الجمهورية الجزائرية الديمقراطية الشعبية
People's Democratic Republic of Algeria
وزارة التعليم العالي والبحث العلمي
Ministry of Higher Education and Scientific Research

Yahia Fares University of Medea

Faculty of Technology

Tribological study of thin films coatings on parts subjected to friction and wear

Doctoral thesis

Presented by:

Khaled Chemaa

In order to get LMD Doctoral

Speciality: Mechanical Engineering: Digital Mechanics and Materials

Defended on July the 7th 2022 before the jury:

Mr. Mourad BACHENE	MCA	Medea University	President
Mr. Mohamed KEZRANE	Professor	Medea University	Supervisor
Mr. Salim HASSANI	Research Director	CDTA	Co-Supervisor
Mr. Mohamed OUCHABANE	Research Director	CDTA	Examiner
Mr. Mohamed BENTCHIKOU	Professor	Medea University	Examiner

Yahia Fares University of Medea 2022

الجمهورية الجزائرية الديمقراطية الشعبية
République Algérienne Démocratique et Populaire
وزارة التعليم العالي والبحث العلمي
Ministère de l'Enseignement Supérieur
et de la Recherche Scientifique

Université Yahia Fares de Médéa

Faculté des technologies

Etude tribologique des revêtements en couches minces sur les pièces soumises aux frottements et à l'usure

Thèse de Doctorat

Présentée par:

Khaled Chemaa

En vue de l'obtention du diplôme de doctorat LMD

Spécialité: Génie mécanique: Mécanique numérique et matériaux

Soutenue le 07 juillet 2022 devant le jury:

Mr. Mourad BACHENE	MCA	Université de Médéa	Président
Mr. Mohamed KEZRANE	Professeur	Université de Médéa	Directeur de thèse
Mr. Salim HASSANI	Directeur de recherche	CDTA	Co-directeur de thèse
Mr. Mohamed OUCHABANE	Directeur de recherche	CDTA	Examinateur
Mr. Mohamed BENTCHIKOU	Professeur	Université de Médéa	Examinateur

Yahia Fares University of Medea 2022

“Allah will raise up to ranks, those of you who believe and who have been granted Knowledge”

The Holy Quran [58:11]

Acknowledgements

First of all, I thank Almighty God for giving me the courage and strength to do this work.

I want to thank my family, my father, my mother and all my sisters and my brothers.

I want to thank my thesis supervisor: **Pr. Kezrane Mohamed** for his advices and support during my thesis duration in Yahia Fares University of Medea since 2017. I want to thank my thesis co-supervisor **Pr. Hassani Salim** who was keen to follow my development in the field of research since my master degree period.

I want to thank the professors and researchers of: Yahia Fares University of Medea, Center of development of advanced technologies, Houarie Boumedien University of Science and Technology and Algérie métallisation Company; who assist me to achieve my coatings and characterizations: **Mr. Younes Salah**, **Pr. Haireche Sofiane**, **Pr. Abdi Said**, **Dr. Khereddine Abd-El-Yazid** and **Mr. Rabhi Said.**

Many thanks to **Pr. Gaceb Mohamed** from M'hamed Bougara University of Boumerdes who assist me by his advices.

Finally, I would like to tribute to all those who, more or less recently, directly or indirectly, in their own way have helped me to complete this thesis.

Khaled Chemaa

Algiers, January 2022

Abstract

This work is a tribological study that tend to give technical solution of the oil and gas valves that suffer from surface failures; through coatings and thin films using different processes: thermal spraying, Plasma Immersion Ion Implantation (PIII) nitriding and Physical Vapour Deposition (PVD). Thermal spraying and post spray vacuum annealing give massive coatings with high hardness (13.9 GPa) and corrosion resistance (0.069 mpy). PIII nitriding increase the hardness of the coating surface (16.4 GPa) and the W-Ti-N thin film deposited by PVD improve the tribological behaviour of the obtained multilayer system (hardness of 22.3 GPa, friction coefficient of 0.14 and a wear rate of $7.55 \cdot 10^{-8}$ $mm^3/N \cdot m$).

Keywords: Coatings, Thin films, Stainless Steel, Triblogy, Nitriding, Thermal Spraying, PIII, PVD.

Résumé

Ce travail est une étude tribologique qui tend à donner une solution technique aux vannes des industries pétrolières et gazières qui souffrent des problèmes de surface ; à travers des revêtements et des couches minces utilisant différents procédés : la projection thermique, la nitruration par implantation d'ions par immersion plasma (PIII) et le dépôt physique en phase vapeur (PVD). La projection thermique et le recuit sous vide après projection donnent des revêtements massifs avec une bonne dureté (13.9 GPa) et une résistance à la corrosion élevée (0.069 mpy). La nitruration par PIII augmente la dureté de la surface du revêtement (16.4 GPa) et la couche mince W-Ti-N déposé par PVD améliore le comportement tribologique du système multicouche obtenu (dureté de 22.3 GPa, coefficient de frottement de 0.14 et un taux d'usure de $7.55 \cdot 10^{-8}$ $mm^3/N \cdot m$).

Mots clés : Revêtements, Couches minces, Acier inoxydable, Tribologie, Nitruration, Projection thermique, PIII, PVD

ملخص

هذا العمل عبارة عن دراسة ترايبولوجية تميل إلى تقديم حل تقني لصمامات النفط والغاز التي تعاني من مشاكل في أسطحها ؛ من خلال الطلاءات والأغشية الرقيقة باستخدام وسائل مختلفة: الرش الحراري، النيترة من خلال زرع أيونات الغمر بالبلازما (PIII) والترسيب الفيزيائي للبخار (PVD). يعطي الرش الحراري والتلدين بالفراغ بعد الرش طلاءات كثيفة ذات صلابة جيدة (13.9 GPa) ومقاومة عالية للتآكل (0.069 mpy). تعمل النيترة بواسطة طريقة PIII على زيادة صلابة سطح الطلاء (16.4 GPa) بينما يعمل غشاء W-Ti-N الرقيق المودع بواسطة تقنية PVD على تحسين الخصائص الترايبولوجية للنظام متعدد الطبقات المتحصل عليه (صلادة 22.3 GPa، معامل احتكاك 0.14 ومعدل اهتراء $(7.55 \cdot 10^{-8}\ mm^3/N \cdot m$.

كلمات مفتاحية: الطلاءات، الأغشية الرقيقة، الفولاذ المقاوم للصدأ، الترايبولوجي، النتردة، الرش الحراري، زرع أيونات الغمر بالبلازما، الترسيب الفيزيائي للبخار.

Contents

Acknowledgement……...……...V

Abstract……...…...……...VII

Contents……...……IX

List of figures……..……XIV

List of tables……..XXI

List of symbols…… XXIII

List of abbreviations…….……XXV

Introduction……...……. XXVIII

Chapter 1: Literature review.....1

1.1. Thermal sprayed Stainless Steel Coatings (SSCs)…….....1

1.2. Enhancing the SSCs surface properties using multilayers.....9

1.3. Enhancing the SSCs by the post-spray annealing.....13

1.4. Plasma Immersion Ion Implantation (PIII) Nitriding.....16

1.5. W-Ti-N thin films.....20

References.....24

Chapter 2: Thermal spray and PVD technologies.....31

2.1. Thermal spray.....31

2.1.1. Introduction.....31
2.1.2. Thermal spray processes.....33
2.1.3. Substrate preparation.....36
2.1.4. Post-spray Heat treatment.....38
2.1.5. Thermal sprayed coatings formation.....38
2.2. Basics of vacuum and plasma.....44
2.2.1. Vacuum and gas state of materials.....44
2.2.2. Motion and velocity of gas molecules.....46
2.2.3. Basics of vacuum technology.....49
2.2.4. Pumping duration.....50
2.2.5. Theory of plasma.....51
2.3. PVD.....52
2.3.1. Vacuum evaporation.....53
2.3.2. Sputtering.....54
2.3.3. Thin films formation.....56
2.3.4. Thin films morphology.....57
References.....59
Chapter 3: Experimental material and methods.....63
3.1. The substrate.....63
3.2. Grit blasting conditions.....64
3.3. Twine-Wire-Arc-Spray (TWAS) deposition parameters.....65
3.4. Optimization of the annealing temperature to enhance the multilayers SSC.....67

3.5 PIII surface treatment.....68

3.6. PVD thin film deposition parameters.....70

3.7. Morphological and structural characterization.....73

3.8. Mechanical Characterization.....74

3.9. Tribological characterization.....76

3.10. Electrochemical characterization.....79

3.11. Performance factor Kp.....80

References.....80

Chapter 4: Surface behaviour optimization of austenite SSCs……..…....….83

4.1. Comparative investigation of 304L and 317L SSCs behaviours……..…..….83

4.1.1. Introduction to the first optimization……...……...…...……83

4.1.2. Microstructural results of the first optimization……..……...……...83

4.1.3. Mechanical results of the first optimization……..…..…..……87

4.1.4. Tribological results of the first optimization……...89

4.1.5. Electrochemical results of the first optimization……..……..93

4.1.6. The performance factors: $Kp_{1(304L\text{-}SSC)}$, $Kp_{1(304L\text{-}SSC)}$ and $Kp_{1(304\text{-}SSB)}$…….……...95

4.2. Study of the surface behaviours of 304L-SSC multilayer……..……..…….97

4.2.1. Introduction of the second optimization……...……..97

4.2.2. Microstructural results of the second optimization…….98

4.2.3. Mechanical results for the second optimization……103

4.2.4. Tribological results for the second optimization……...106

4.2.5. Electrochemical results for the second optimization……..…….....110

4.2.6. The performance factors $K_{P2(SS\text{-}1L)}$, $K_{P2(SS\text{-}2L)}$, $K_{P2(SS\text{-}3L)}$, $K_{P2(SS\text{-}4L)}$……..……...111

4.3. Effect of annealing temperature on the surface behaviour of four layered SSC…....114

4.3.1. Introduction to the third optimization……..…….114

4.3.2. Microstructural results for the third optimization…….115

4.3.3. Mechanical results of the third optimization……..……..…..……121

4.3.4. Tribological results for the third optimization…….……124

4.3.5. Electrochemical results for the third optimization……...……128

4.3.6. The performance factors $K_{P3(SS-800)}$, $K_{P3(SS-1000)}$ and $K_{P3(SS-1100)}$……..……...130

4.4. Conclusions…….……132

References……..……..……..……134

Chapter 5: Improvement the tribological behaviour of the stainless steel coating nitrided by PIII……...……..…….....….141

5.1. Introduction……...……..141

5.2. Microstructural characterization……..142

5.3. Mechanical characterization……....147

5.4. Tribological characterization……...……148

5.5. Conclusions…….152

References…….…153

Chapter 6: Improving the tribological behaviour by W-Ti-N duplex treatment……...……...……...157

6.1. Introduction…….....157

6.2. Microstructural characterization……..157

6.3. Mechanical characterization……..…..161

6.4. Tribological characterization……163

6.5. Conclusions……...……..168

References……..168

General conclusions……..…..171

List of figures

Figure 1 Ball with adhesive wear tracks……...…… XXIX

Figure 2 Wedge gate with adhesive and abrasive wear tracks……..……. XXIX

Figure 3 Parallel gate with pitting corrosion and adhesive wear tracks…….. XXX

Figure 1.1 Cross-section for the 316L SSC deposited by: (a) APS, (b) SPS, (c) HVOF [1.2].....1

Figure 1.2 Cross-section of 316L SSC: (a) before and (b) after electrochemical tests [1.3].....3

Figure 1.3 Cross-section of 321 SSC [1.8].....4

Figure 1.4 Surface image of 321 SSC wear tracks morphology: (a) under dry condition, (b) under lubricated condition [1.8].....5

Figure 1.5 Morphology images of the worn 420 SSC surfaces deposited by (a) EEDS, (b) HVAS [1.9].....6

Figure 1.6 Wear tracks observations on 431 SSC by (a) OM, (b) SEM [1.10].....7

Figure 1.7 Wear tracks images of amorphous SSC under: (a) F=10 N, (b) F=40 N [1.12].....8

Figure 1.8 SEM images of 304L SSC: (a) top surface, (b) cross-section [1.14].....8

Figure 1.9 Cross-section for 316L SSC with: (a) 2 layers, (b) 3 layers, (c) 4 layers [1.5]…..10

Figure 1.10 Pathway to the crack propagation in the multilayers coatings [1.17]…….10

Figure 1.11 Cross-section images of the corroded SSC with: (a) 1 layer, (b) 2 layers, (c) 3

layers [1.5]……..…….12

Figure 1.12 Surface images of the as-sprayed Fe-316L SSC and the annealed one at 1100°C [1.21]……..…...13

Figure 1.13 Cross-section of the annealed 304L SSC at 600 °C, 800 °C and 950 °C [1.20]...14

Figure 1.14 Cross-section images of the as-sprayed and the annealed 316L SSC at 1000 °C with air annealing, vacuum annealing and HIP [1.22]……..……...15

Figure 1.15 Wear mechanisms for the PIII nitrided supermartensitic stainless steel at different temperatures [1.28]……...…….19

Figure 1.16 Wear track profiles and micrographs in the disk and crater in the ball for W-Ti-N films deposited with N_2/Ar ratios of: (a) 1/ 3, (b) 1/5 and (c) 0 [1.44]……22

Figure 1.17 friction curves of: (a) W-Ti-N thin film on two different substrates, (b) W-Ti-N/Al-Si multilayer and the Al-Si thin film [1.41]……...23

Figure 1.18 (a) Micrograph of W-Ti-N film on nitrided substrate without white layer, (b) Micrograph of W-Ti-N on nitrided substrate with white layer [1.45].....24

Figure 2.1 Splats deposited by CGDS [2.4].....32

Figure 2.2 Lamellae structures deposited by SPS [2.6].....33

Figure 2.3 General thermal spraying processes.....33

Figure 2.4 TWAS process principle [2.3].....35

Figure 2.5 Subcritical flow regime in the impact of a liquid particle [2.1].....39

Figure 2.6 Lamella and principal morphologies [2.1].....40

Figure 2.7 (a) planar, (b) cellular, (c) dendritic solidification front morphologies [2.9].....42

Figure 2.8 General defects obtained on the thermal sprayed coatings [2.1].....44

Figure 2.9 Gas velocities distributions at two different temperatures [2.11].....47

Figure 2.10 Free mean path of gas molecules as a function of the pressure [2.11].....48

Figure 2.11 Principle of a vacuum setup.....49

Figure 2.12 Nomogram for calculating the pumping time [2.11].....50

Figure 2.13 PVD vacuum evaporation system [2.8].....53

Figure 2.14 PVD sputtering system [2.8].....54

Figure 2.15 Principle of the magnetron work in PVD sputter process [2.14].....55

Figure 2.16 The three modes of thin films formation [2.15].....57

Figure 2.17 Movchan and Demchishin model [2.17].....58

Figure 2.18 Thornton model [2.19].....58

Figure 2.19 Messier model [2.20].....59

Figure 3.1 Substrates size.....63

Figure 3.2 XRD patterns for EN 10025-2 Structural Steel.....64

Figure 3.3 Metallisation Ltd TWAS system of Algérie Métallisation Company.....66

Figure 3.4 Metallisation Ltd TWAS system spraying gun.....66

Figure 3.5 OTF-1200X-II-UL vacuum split tube furnace of CDTA.....68

Figure 3.6 PIII treatment system of the CDTA.....69

Figure 3.7 (a) CDTA PIII system setup [3.6], (b) a sample in the sample holder during the treatment inside the plasma atmosphere.....69

Figure 3.8 PVD magnetron sputtering installation of the CDTA…….....…...71

Figure 3.9 (a) The samples during the deposition of the W-Ti-N thin film inside the deposition reactor in the plasma atmosphere, (b) The samples after the deposition of the film.....72

Figure 3.10 X-Ray Diffraction (XRD) setup of CDTA.....73

Figure 3.11 Scanning Electron Microscopy (SEM) coupled with Energy-dispersive X-ray spectroscopy (EDS) of USDB.....74

Figure 3.12 CSM Nano-indentation tester of CDTA.....75

Figure 3.13 Nemesis 9000 Vickers hardness tester of CRTI.....76

Figure 3.14 CSM tribometer of USTHB.....77

Figure 3.15 A100 AFM of UYFM.....78

Figure 3.16 Optika B-383 MET OM of UYFM.....79

Figure 3.17 (a) Electrochemical test Cell, (b) Electrochemical test Assembly of CDTA.....80

Figure 4.1 SEM micrographs of: (a) 304L-SSC and (b) 317L-SSC…….……..84

Figure 4.2 EDS spectra of: (a) 304L-SSC and (b) 317L-SSC……..……...85

Figure 4.3 Roughness analysis results for 304L-SSC and 317L-SSC……..……..85

Figure 4.4 SEM cross-section of: (a) 304L-SSC and (b) 317L-SSC……..86

Figure 4.5 XRD diffraction patterns of: 304-SSB, 317L-SSC and 304L-SSC……..87

Figure 4.6 Hardness measurement results for: 317L-SSC, 304L-SSC and 304-SSB……...88

Figure 4.7 Typical nanoindentation curves for: 304L-SSC, 317L-SSC and 304-SSB……...89

Figure 4.8 COF variations as function of the sliding distance for: 317L-SSC, 304L-SSC and 304-SSB……...…….90

Figure 4.9 AFM 3D wear tracks profiles for: (a) 317L-SSC, (b) 304L-SSC and (c) 304-SSB……....92

Figure 4.10 OM wear tracks observations for: (a) 317L-SSC, (b) 304L-SSC and (c) 304-SSB……....92

Figure 4.11 Polarization curves of: 317L-SSC, 304L-SSC and 304-SSB.....94

Figure 4.12 Polar diagrams providing a qualitative comparison of the samples: 317L-SSC, 304L SSC and 304-SSB……..…….….95

Figure 4.13 XRD diffraction patterns for SS-1L, SS-2L, SS-3L and SS-4L……..98

Figure 4.14 SEM top view images with magnifications for: (a) SS-1L, (b) SS-2L, (c) SS-3L and (d) SS-4L……..……100

Figure 4.15 SEM cross-section images with the EDS analysis for: (a) SS-1L, (b) SS-2L, (c) SS-3L, (d) SS-4L…….……102

Figure 4.16 Roughness analysis results for: SS-1L, SS-2L, SS-3L and SS-4L……103

Figure 4.17 Hardness measurement results for: SS-1L, SS-2L, SS-3L and SS-4L……..104

Figure 4.18 Typical nanoindentation curves for: SS-1L, SS-2L, SS-3L and SS-4L……...106

Figure 4.19 COF variations as function of the sliding distance for: SS-1L, SS-2L, SS-3L and SS-4L……...……...107

Figure 4.20 AFM 3D images of wear tracks profiles for: (a) SS-1L, (b) SS-2L, (c) SS-3L and (d) SS-4L……...……..108

Figure 4.21 Wear tracks observations for: (a) SS-1L, (b) SS-2L, (c) SS-3L and (d) SS-4L……109

Figure 4.22 Polarization curves of: SS-1L, SS-2L, SS-3L and SS-4L……...110

Figure 4.23 Polar diagrams providing a qualitative comparison of the coatings: SS-1L, SS-2L, SS-3L and SS-4L……...…….……112

Figure 4.24 SEM cross-section images for: (a) SS-0, (b) SS-800, (c) SS-1000, (d) SS-1100…….116

Figure 4.25 EDS analysis results for: (1) SS-0, (2,3) SS-800, (4,5) SS-1000 and (6,7,8) SS-1100…….117

Figure 4.26 XRD diffraction patterns for: SS-0, SS-800, SS-1000 and SS-1100……..…….118

Figure 4.27 SEM top view images for: (a) SS-0, (b) SS-800, (c) SS-1000 and (d) SS-1100.……119

Figure 4.28 Roughness analysis results for: SS-0, SS-800, SS-1000 and SS-1100…….....120

Figure 4.29 Hardness measurement results for: SS-0, SS-800, SS-1000 and SS-1100……..121

Figure 4.30 Typical nanoindentation curves for: SS-0, SS-800, SS-1000 and SS-1100.....124

Figure 4.31 COF variations as function of the sliding distance for: SS-0, SS-800, SS-1000 and SS-1100……...……125

Figure 4.32 Wear tracks observations for: (a) SS-0, (b) SS-800, (c) SS-1000 and (d) SS-1100…….126

Figure 4.33 AFM 3D images of wear tracks profiles for: (a) SS-0, (b) SS-800, (c) SS-1000 and (d) SS-1100……..127

Figure 4.34 Polarization curves for: SS-0, SS-800, SS-1000 and SS-1100…….…...128

Figure 4.35 Polar diagrams providing a qualitative comparison of the coatings: SS-0, SS-800, SS-1000 and SS-1100……...……..130

Figure 5.1 XRD diffraction patterns of: (a) SSC, (b) PIII-200, (c) PIII-300…….…….143

Figure 5.2 SEM top surface for: (a) SSC, (b) PIII-200, (c) PIII-300……..144

Figure 5.3 Cross-section images of: (a) SSC, (b) PIII-200 and (c) PIII-300…….….145

Figure 5.4 EDS analysis results at the different zones……146

Figure 5.5 Three-dimensional surface topography of: (a) SSC, (b) PIII-200 and (c) PIII-300…..……...……..146

Figure 5.6 Typical nanoindentation curves for: (a) PIII-200, (b) PIII-300 and (c) SSC…....147

Figure 5.7 COF variations as function of the sliding distance for: (a) SSC, (b) PIII-200, (c) PIII-300…….……..……149

Figure 5.8 AFM 3D images of wear tracks profiles for: (a) SSC, (b) PIII-200 and (c) PIII-300.....150

Figure 5.9 SEM wear tracks and EDS punctual analysis of the worn surfaces of: (a) SSC, (b) PIII-200 and (c) PIII-300……...…….……151

Figure 6.1 XRD diffraction patterns of: (a) SSC, (b) PIII/SSC and (c) W-Ti-N/PIII/SSC....158

Figure 6.2 Cross-section images of: (a) SSC, (b) PIII/SSC and (c) W-Ti-N/PIII/SSC multilayer coatings……..…….159

Figure 6.3 EDS analysis results at the different zones……..……..160

Figure 6.4 SEM top view images for: (a) SSC, (b) PIII/SSC and (c) W-Ti-N/PIII/SSC.……...……..160

Figure 6.5 Typical nanoindentation curves for: (a) W-Ti-N/PIII/SSC, (b) PIII/SSC and (c) SSC multilayer coatings…….……161

Figure 6.6 COF variations as function of the sliding distance for: (a) SSC, (b) PIII/SSC, (c) W-Ti-N/PIII/SSC……...…….……164

Figure 6.7 AFM 3D images of wear tracks profiles for: (a) SSC, (b) PIII/SSC and (c) W-Ti-N/PIII/SSC……..……...…….165

Figure 6.8 SEM wear tracks and EDS punctual analysis of the worn surfaces of: (a) SSC, (b) PIII/SSC and (c) W-Ti-N/PIII/SSC multilayer coatings……....……166

Figure 6.9 Rabinowicz Compatibility table [6.12]……...……..…167

List of tables

Table 2.1 Grit blasting principal parameters [2.1]…….……...38

Table 2.2 Thermal flux types for different spraying processes [2.7]……41

Table 2.3 General characteristics of vacuum types [2.10]…….…...44

Table 3.1 EN 10025-2 carbon steel chemical composition [3.1]…….……64

Table 3.2 Grit blasting parameters……...…….65

Table 3.3 Wire Flame spraying deposition parameters……...……..65

Table 3.4 304L wire chemical composition……..67

Table 3.5 317L wire chemical composition……..67

Table 3.6 Annealing parameters……...67

Table 3.7 PIII treatment parameters……..70

Table 3.8 W-Ti-N thin film deposition parameters……...……72

Table 3.9 Nano-indentation test parameters……..……..…75

Table 3.10 Tribological tests parameters……..……77

Table 4.1 Nanoindentation test results of: 317L-SSC, 304L-SSC and 304-SSB…….88

Table 4.2 Tribological test results of: 317L-SSC, 304L-SSC and 304-SSB…….....91

Table 4.3 Corrosion results extracted from the corrosion polarization curves……93

Table 4.4 Factors values of: 304L-SSC, 317L-SSC and 304-SSB……...…96

Table 4.5 Spray parameters of the second optimization……..……...97

Table 4.6 Nanoindentation test results for: SS-1L, SS-2L, SS-3L and SS-4L…….…….105

Table 4.7 Tribological test results for: SS-1L, SS-2L, SS-3L and SS-4L……..……...…107

Table 4.8 Electrochemical test results for: SS-1L, SS-2L, SS-3L and SS-4L……111

Table 4.9 Factors values of: SS-2L, SS-3L and SS-4L……..…..……113

Table 4.10 Annealing parameters for the different coatings……..……..115

Table 4.11 Nanoindentation test results for: SS-0, SS-800, SS-1000 and SS-1100……..…123

Table 4.12 Tribological test results for: SS-0, SS-800, SS-1000 and SS-1100……..126

Table 4.13 Electrochemical test results for: SS-0, SS-800, SS-1000 and SS-1100……129

Table 4.14 Factors values of: SS-800, SS-1000 and SS-1100……...…...131

Table 5.1 Nanoindentation test results for: SSC, PIII-200 and PIII-300……...…...148

Table 5.2 Tribological results after PIII nitriding……..…...150

Table 6.1 Nanoindentation test results for: SSC, PIII/SSC and W-Ti-N/PIII/SSC…….162

Table 6.2 Tribological results after W-Ti-N deposition……...……...165

List of symbols

a: Molecule diameter (mm);

B: Number of the intermolecular impacts;

C_R: Corrosion rate (mpy);

D: Sliding distance (m);

d: Distance (m);

D_P: Wear track depth (m);

E: Elastic modulus (GPa);

E_{OC}: Open circuit potential (V);

F: Normal load (N);

H: Hardness (HV_{10});

H_N: Nanohardness (GPa);

i_{corr}: Corrosion potential ($\mu A/cm^2$);

k: Wear rate ($mm^3/N \cdot m$);

k': Boltzmann constant ($1.38 \cdot 10^{-6}$ $N \cdot m/K$);

Kn: Knusden number;

K_P: Performance factor ($N^2 \cdot year/mm^5$);

m: molecule mass (kg);

n: Density of the molecules (m^{-3});

P: Pressure (Pa);

Q: Mass flow rate (kg/s);

R_p: Potential resistance ($\Omega \cdot m^2$);

T: Temperature (K);

v: Gas velocity (m/s);

V_k: Wear volume (m^3);

v_p: The most probable velocity of a molecule (m/s);

$\bar{v}$: Arithmetic mean velocity (m/s);

$\sqrt{\bar{v}^2}$: Root mean square velocity of molecules (m/s);

w: Wear track width (m);

α': Degree of the gas ionization;

α-Fe: Ferrite/Martensite phase;

γ-Fe: Austenite phase;

λ: Mean free path of the gas molecule (m);

μ: Coefficient of friction;

ρ: Density of the gas (kg/cm^3).

List of abbreviations

304-SSB: 304 Stainless Steel Bulk;

304L-SSC: 304L Stainless steel coating;

317L-SSC: 317L Stainless steel coating;

AFM: Atomic Force Microscope;

APS: Atmospheric Plasma Spray;

CAPS: Controlled Atmosphere Plasma Spray;

CDTA: Center for Development of Advanced Technologies;

CGDS: Cold Gas Dynamic Spray;

CGS: Cold Gas Spray;

COF: Coefficient of friction;

CRTI: Research Center for Industrial Technologies;

D-gun: Detonation Gun Spray;

EDS: Energy-Dispersive Spectroscopy;

EEDS: Electro-thermal Explosion Directional Spray;

FS: Flame Spray;

FS-Powder: Powder Flame Spray;

FS-Wire: Wire Flame Spray;

HIP: Hot Isostatic Pressing;

HVAS: High Velocity Arc Spray;

HVOF: High Velocity Oxy Fuel;

IPS: Inert-Gas Plasma Spray;

LEI: Low-Energy Ion Implantation;

OM: Optical Microscope;

PIII: Plasma Immersion Ion Implantation;

PVD: Physical vapor deposition;

RF: Radio Frequency;

SSC: Stainless Steel Coating;

SEM: Scanning Electron Microscope;

SPS: Shrouded plasma spray;

SS-0: Stainless Steel Coating without annealing;

SS-800: Stainless Steel Coating annealed at 800°C;

SS-1000: Stainless Steel Coating annealed at 1000°C;

SS-1100: Stainless Steel Coating annealed at 1100°C;

SS-1L: Stainless Steel Coating with single-layer;

SS-2L: Stainless Steel Coating with two layers;

SS-3L: Stainless Steel Coating with three layers;

SS-4L: Stainless Steel Coating with four layers;

TEC: Thermal Expansion Coefficient;

TWAS: Twin-Wire Arc Spray;

USDB: Saad Dahlab University of Blida;

USTHB: Houarie Boumedien University of Science and Technology;

UYFM: Yahia Fares University of Medea;

VPS: Vacuum Plasma Spray;

XRD: X-Ray Diffraction.

Introduction

In oil and gas industries, valves are the components in fluid flow systems that have three main functions: stopping and starting flow, controlling flowrate and diverting flow [1]. Those functions are performed by adjusting the position of the valve closure member.

The choice of the valve base material is based on the requirements of temperature, corrosion resistance, abrasive wear resistance and manufacturing process [2]. Some fluids require the use of special expensive materials or materials with complex manufacturing processes in order to prevent any failure.

The most common materials for valves are the AISI 300 stainless steel series. AISI 302 can be considered as the lowest tolerated grade. AISI 304 is the most popular stainless steel grade especially for cryogenic applications since it has good behaviors at temperatures down to -196°C to -250°C. Another popular grade is AISI 316, although it is not preferred for low temperatures applications due to its minimum standardised temperature of -60°C. If welding is required and post weld heat treatment is difficult or expensive, the low carbon grades 304L and 316L are applicable [2].

Some reported researches [1] shows that stainless steel valves are susceptible to severe adhesive wear known also by galling. Cavitation can occur also in liquid flow systems if there is changes of phases either from liquid to vapour in the valves inlet or from vapour back to

liquid in the outlet [2]. Erosion is another problem when the flowing fluid contains solids that can destroy the valves characteristics [2].

In an expertise visit to POVAL, which is an Algerian company that manufactures and repairs oil and gas valves, it was found that the most common surface defects on their valves are adhesive wear or galling such as the ball valve closure member given in **Figure 1**, or abrasive wear like the gate of the wedge gate valve given in **Figure 2** or pitting corrosion like gate of the parallel gate valve given in **Figure 3**.



Figure 1 Ball with adhesive wear tracks



Figure 2 Wedge gate with adhesive and abrasive wear tracks



Figure 3 Parallel gate with pitting corrosion and adhesive wear tracks

In order to reduce the valves surfaces defects, coatings and thin films can give interesting solutions in tribological point of view. In addition to their economic impact. Metallic alloys coatings such as stellite (6, 12 and SF6), colmonoy 6 and tungsten carbide LW-5 deposited by various processes and especially the thermal spray and the laser beam [2]. Hard chromium HC and nanostructured cobalt-phosphor NCP [3] are also reported as good candidates to coat the valves. It is good to notice that when depositing metallic coatings to stainless steel valves, it is better to use the low carbon grades in order to avoid the cabrides precipitations within the substrate [2]. Cladded SSCs on valves made by carbon steels are used to reduce the manufacturing costs by stainless steels, the coatings thicknesses are desirable to be at least of 1 mm, but the poor surface properties of those coatings limit their use [4]. Surface treatments of the valves using nitriding and siliconizing [5] used also to increase their hardness and corrosion resistance.

The aim of the present thesis is to study a new system of coatings/thin films and their behavior for future application on valves surfaces made by carbon steel alloy instead of stainless steel, combining their technical effects with economic impacts. This study can be divided in two parts. The first part consists of introducing a thermal sprayed SSC on carbon steel substrate, testing and optimizing their surface properties through different methods in order to get the SSC with better surface behavior than the massive stainless steel. The second

part consists of introducing a duplex thin film on the previous coating by nitriding first the optimized SSC using PIII process then depositing the famous lubricate ternary thin film W-Ti-N by PVD process. This second part has as objective to enhance more the tribological properties of the SSC, since the most important valves defects are adhesive wears (galling) and abrasive wears.

Introducing a system made by thermal sprayed SSC, nitrided layers and W-Ti-N thin film is an original work in tribology domain. This system can have simultaneously the corrosion resistance of the sprayed SSC, the hardness of the nitrided layers and the excellent tribological properties of the W-Ti-N thin film.

The thesis is composed of 6 chapters:

The chapter 1 is a literature review chapter, where the previous studies on SSCs were reviewed, also the main methods to optimize the SSCs which are the number of the coating layers increasing and the post spraying heat treatment were reviewed also. At the end, the previous works dealing with nitriding the massive steels and stainless steels by PIII were reviewed (since nitriding SSCs by PIII is original). The previous studies on the effect of W-Ti-N thin film on enhancing the tribological properties of steels were reported also.

The chapter 2 is a theoretical overview on the thermal spraying technology and methods, the sprayed coatings morphology and formation, vacuum and plasma theory, PVD technology and the thin films morphology and formation.

Chapter 3 is a description of the procedures used in our study and of the equipment and the materials of the SSC and the thin film depositions, PIII nitriding and the surface characterizations.

Chapter 4 studied the SSCs deposited by TWAS process and their microstructural, mechanical, tribological, and electrochemical properties through 3 different optimizations

steps. The first optimization is to choose the best SSC grade between 304L and 317L. The second optimization is to vary the number of the coating layers from 1 to 4. The third optimization consist of applying a post spraying vacuum annealing with 3 different temperatures: 800°C, 1000°C and 1100°C.

In chapter 5, the optimized SSC was nitrided by PIII process with different injected powers: 200 W and 300 W in order to choose the optimal power that can enhance the coating microstructure, mechanical and tribological properties.

In chapter 6, W-Ti-N thin film was deposited on the nitrided SSC to form a lubricated duplex film in order to enhance more the tribological properties of the optimal nitrided SSC.

Our research study has resulted numerous scientific works as follows:

1) Peer-reviewed papers

1- Investigation of the effect of vacuum annealing on the tribological properties of the austenite stainless steel multilayer coatings. Applied Physics A (IF: 2.584) 128(2):1-13, (2022), DOI: 10.1007/s00339-022-05272-y

2- Tribological and corrosion behaviours of 304L and 317L stainless steel coatings for mechanical parts subjected to friction and wear. Journal of Materials Engineering and Performance (IF: 1.819), (2021), DOI: 10.1007/s11665-022-06830-4

3- Austenite stainless steel multilayers coatings on ball valves for tribological and corrosion behaviour improvement. Applied Physics A (IF: 2.584) 128(7):1-10, (2022), DOI: 10.1007/s00339-022-05770-z

2) Under reviewed papers

1- Tribological characterization of austenitic stainless steel multilayer coatings nitrided by plasma immersion ion implantation.

2- Tribological investigation of duplex treatment: W-Ti-N thin film on nitrided stainless steel multilayer coating by plasma immersion ion implantation.

3) Conferences

1- Tribological study of Al-Si and Ti-W-N multilayer thin films deposited on stainless steel, The 4th International Conference on Fracture Mechanics, 26-29 November 2018, Chlef University, Algeria.

2- Structural, mechanical and tribological characterization of Al-Si thin film, The 8th Chemistry days, 26-27 March 2019, Polytechnic Military School Algiers, Algeria.

3- Tribological behaviors of Ti-W-N thin film for diesel engines applications, 8th International Symposium on Hydrocarbons and Chemistry, 08-10 April 2019, Boumrdes University, Algeria.

4- Tribological study of the stainless steel coating multilayer for ball valves application, 1st National Conference on Applied Science and Advanced Materials, 20-22 December 2021, ENSET-Skikda, Algeria.

References

[1] R.W. Zappe, *Valve selection handbook*, Gulf Professional Publishing, Houston, 1999.

[2] B. Nesbitt, *Handbook of Valves and Actuators: Valves Manual International*, Butterworth-Heinemann, Oxford, 2007.

[3] L. Vernhes, M. Azzi, and J.E. Klemberg-Sapieha, Alternatives for hard chromium plating: Nanostructured coatings for severe-service valves, *Mater. Chem. Phys.*, 2013, **140(2-3)**, p 522-528.

[4] J. Lewin, *Hydraulic gates and valves In Free Surface Flow and Submerged Outlets*, Thomas Telford Publishing, London, 1995.

[5] A. Bahadori, *Oil and gas pipelines and piping systems*, Gulf Professional Publishing, Oxford, 2017.

Chapter 1: Literature review

1.1. Thermal sprayed SSCs

Cross-section images for 316L SSCs deposited by APS and SPS processes are given in **Figure 1.1 (a)** and **(b)** and they present the typical thermal sprayed coatings lamellae structures. Those structures indicate that the sprayed particles are well melted. The dark regions represent the oxides that can be formed during spraying. HVOF process (**Figure 1.1 (c)**) coating doesn't reveal the lamellae structure but a lot of the unmelted particles [1.1]. SSCs surfaces are composed generally of fine splats that are adhered to each other with some unmelted particle [1.2].

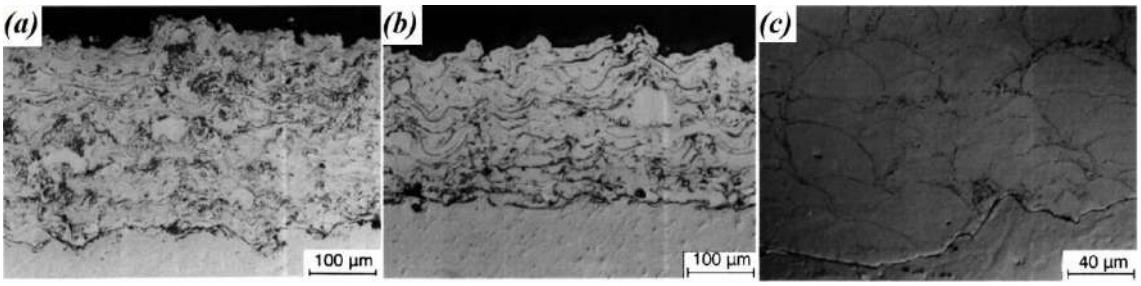


Figure 1.1 Cross-section images for 316L SSC deposited by: (a) APS, (b) SPS, (c) HVOF [1.2]

The thermal sprayed coatings are built up from individual particles that impact the substrate as fully melted, semi-melted or unmelted. The unmelted ones are weakly bonded to the rest of the coating, reducing as consequence the coating toughness. For that reason, a carful optimization of the spray parameters is a necessity to avoid or minimize the unmelted particles formation [1.3].

Increasing the deposition temperature reduces the formation of the unmelted particles, leading to higher adhesion strength between the coating splats in one side and between the coating and the substrate in the other side [1.3]. In addition, the plasticity of the coating will be enhanced [1.4]. On the contrary, increasing the deposition temperature increases oxides, cracks and residual stresses amount in the coating [1.3]. At low deposition temperatures, particles do not deform plastically and they erode the substrate and as a consequence, low coating thickness will be obtained. The obtained coating will be characterized also by higher porosity amount and lower adhesion strength between the coatings splats and between the coating and the substrate [1.4]. Low deposition temperatures reduce the oxides amount within the coating [1.2].

Spray distance between the spray gun and the substrate can be considered also as a very important parameter. Short distances do not permit the particles to be sufficiently heated and accelerated to the substrate, resulting in a high amount of the unmelted particles. Higher distances can increase the kinetic energy of the sprayed particles [1.3]. The deposition efficiency can be increased also by increasing the spray distance and that is related to the decreasing in the number of the unmelted particles [1.5]. As a numeric example, for 316L SSC deposited by HVOF, at spraying distances between d=50 mm and d=175 mm, the coating exhibits a dense microstructure, while at d=300 mm, pores begin to appear in the coating. Oxides inclusions can be observed at a distance of d=50 mm, while between d=175 mm to d=300 mm no apparent oxides inclusions can be observed [1.2].

Thermal spray velocity is another factor. Higher velocities enhance the coatings adhesion and decrease their porosity [1.2].

316L SSCs contain generally variety of iron oxides such as: FeO, Fe_2O_3 and Fe_3O_4 [1.6]. The coatings phases are also of different types and they are mainly: martensite, ferrite and

austenite. The existence of the metastable austenite is because of Ni that can be considered as an austenite stabilizer. Ferrite and martensite can exist during the rapid solidification of the coating in the areas with less Ni content [1.6]. Due to the difference in the TECs of the different phases existing in the coatings, their chemical uniformity will be disrupted [1.7].

316L SSC deposited by CGS exhibits hardness between H=314 HV_N and H=358 HV_N [1.4] and from H=293 $HV_{0.3}$ to H=312 $HV_{0.3}$ for the same coating deposited by HVOF, between H=244 $HV_{0.3}$ to H=257 $HV_{0.3}$ for the one obtained by SPS, and H=241 $HV_{0.3}$ to H=262 $HV_{0.3}$ [1.1] for the coating obtained by APS. With increasing the oxides amount within the coating, the coating hardness increases [1.2].

The reported wear rates of 316 SSCs are in the order of $k=9\cdot10^{-3}$ $mm^3/N\cdot m$ for the coating deposited by CGS, $k=1.32\cdot10^{-4}$ $mm^3/N\cdot m$ for the one deposited by HVOF with hydrogen gas and $k=1.60\cdot10^{-4}$ $mm^3/N\cdot m$ by HVOF with propylene gas [1.4]. Iron oxides enhance the wear resistance of the coating by showing self lubricating performance and reduce the sliding wear and the COF [1.6], while, porosity has an inverse effect [1.4].

Corrosion resistance of 316L SSCs depends on the spraying parameters and especially the spraying distance between the spray gun and the substrate in the case of HVOF. Higher spraying distance (d=310 mm) shows higher E_{OC} (between -0.334 V to -0.360 V) than the shorter ones (d=260 mm between -0.379 V to -0.412 V) [1.7].

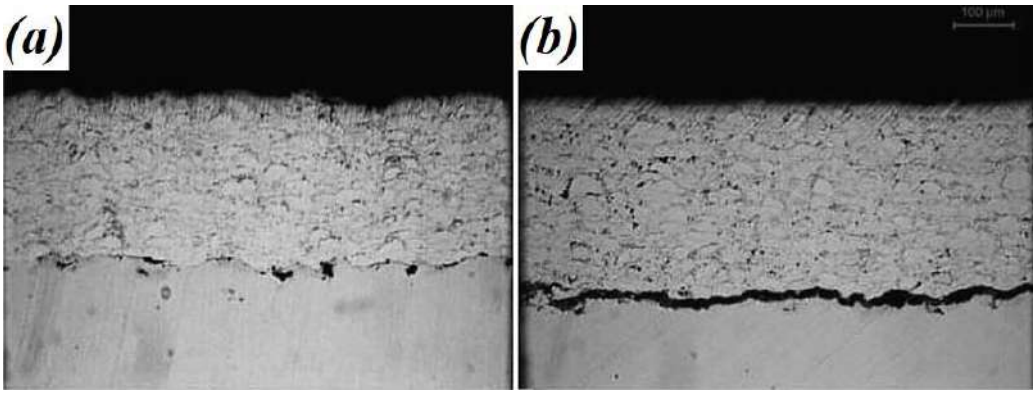


Figure 1.2 Cross-section of 316L SSC: (a) before and (b) after electrochemical tests [1.3]

Because of the SSC defects such as oxides and pores, the electrolyte penetrates through them to reach and corrode the substrate. Leading to the destruction of the bounding between the coating and the substrate [1.1]. Once the electrolyte reaches the substrate, a galvanic pair will be formed in the interface due to the noble nature of SSC, causing an accelerated corrosion process and a complete oxidation of the interface and at the end, the coating detachment (**Figure 1.2**) [1.3]. Coating oxides such as iron oxides [1.7] and chromium oxides [1.1] impairs the corrosion resistance of SSCs by changing their electrochemical potential after the dissolution of the oxides in the electrolyte.

321 SSC deposited by HVAS [1.8] reveals also the typical lamellar structure with splats (a), oxides (b), micro-cracks (c) and pores (d) (**Figure 1.3**). Another remark for 321 SSC is its aptitude to form cracks. The existence of the cracks suggests that the sprayed particles have encountered metamorphosis and distortions during their deposition, leading to the generation of residual stresses and other defects. Cracks often initiate from the oxide layers with the action of the residual stresses. The mean hardness value of the coating is H=459.5 $HV_{0.1}$ with a porosity of 3%. The wear volume is in the order of V_k=201.5 mm^3 and that at lubricated conditions is V_k=218.1 mm^3.

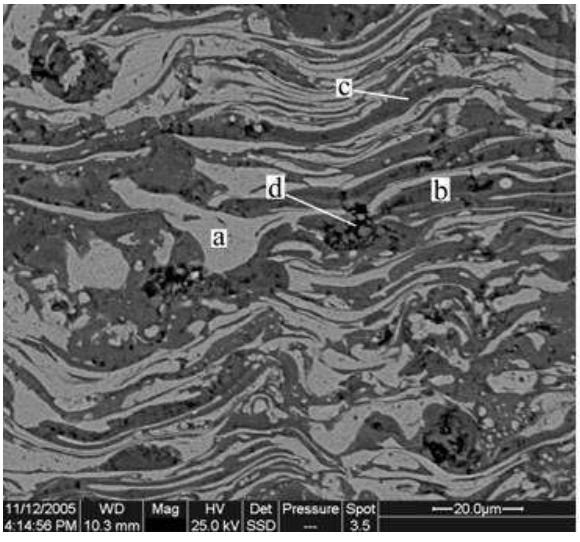


Figure 1.3 Cross-section of 321 SSC [1.8]

The wear tracks analysis using SEM under dry sliding conditions shows the distribution of some cracks around the scaling pits in addition to few slight plows (**Figure 1.4 (a)**). Under dry conditions, the shear contact stresses on the sliding surface of the coating are as high as the cohesive strength of the inter-splats, these strong shear stresses lead to the generation of micro-cracks in the oxides zones or in the pores. With the increase in the sliding distance, the initiated micro-cracks grow up and extend through the inter-particles boundaries. When the stress intensity factor of the micro-cracks is close to the fracture toughness of the coating, the whole splats break off from the coating, giving the scaling pits. With the processing of sliding, the splats scaled from the coating keep increasing. In addition, the scaling pits rough the surface of coating leading to the initiation of local asperities that accelerate the wear rate [1.8].

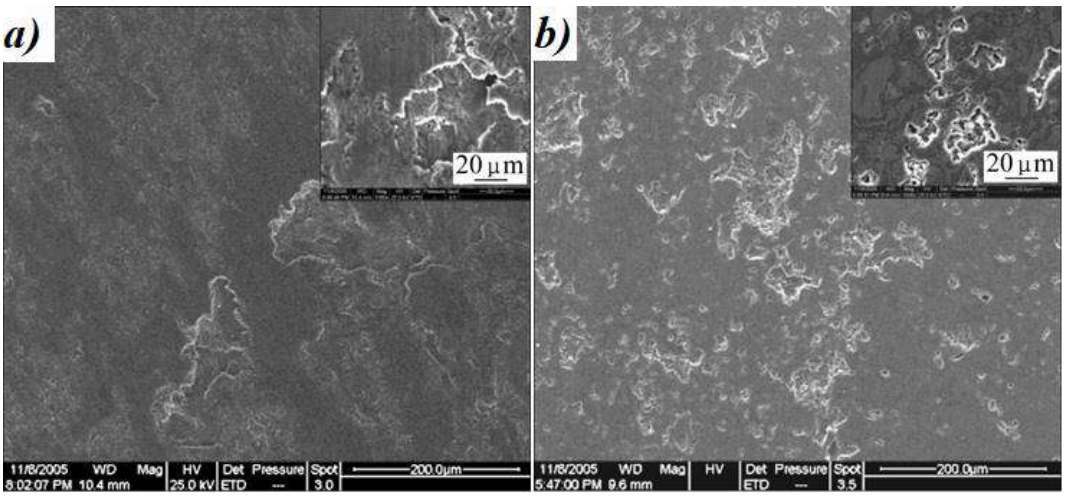


Figure 1.4 Surface image of 321 SSC wear tracks morphology: (a) under dry condition, (b) under lubricated condition [1.8]

The COF of the coating is increased from µ= 0.58 to 1.2 at the beginning of the test, then it is varied relatively in a small range between µ=1.25 to 1.1, later on it become stable at a value of µ=1.15.

420 SSC was deposited by two processes: EEDS and HVAS [1.9]. The results showed that with EEDS, more compact microstructure was obtained with no lamellar structures and with higher hardness (H=10.3 GPa for EEDS and H=7.6 GPa for HVAS) and elastic modulus (E=237.8 GPa for EEDS and E=183.3 GPa for HVAS), and better wear resistance. HVAS coating wear tracks revealed microploughing furrows caused by the counterbody. Also, delamination could be observed (**Figure 1.5**). When the counterbody slides against the coating surface, the surface and the subsurface of the coating are subjected to alternate tensile and compression stresses and thereby the plastic distortion occurs. Along with the plastic distortion, dislocations and cracks initiate and propagate at a shallower position beneath the worn surface. Cracks are easily generated also on the boundaries between the lamellar structures due to their weak bonds. With the propagation of the cracks, delamination happens. Wear debris act as abrasive third bodies that accelerate the wear process, and so the abrasive wear can be observed too.

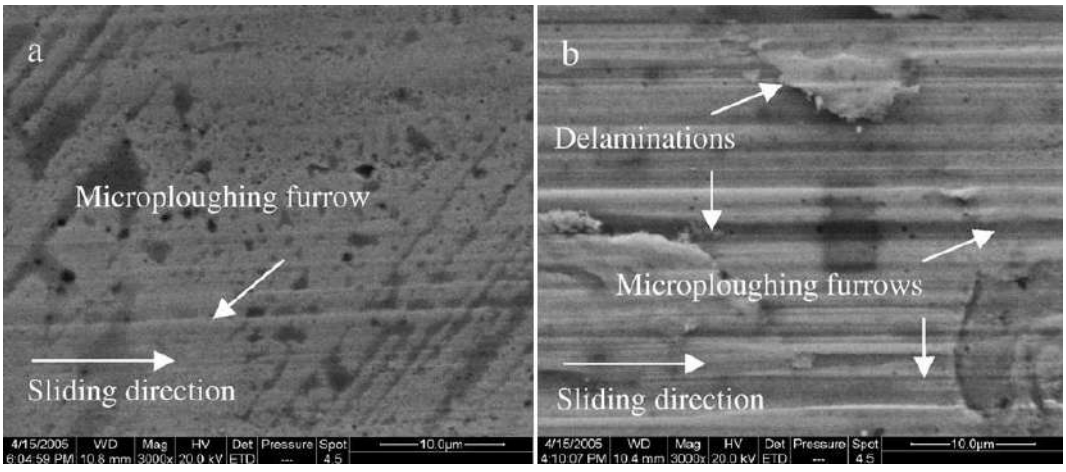


Figure 1.5 Morphology images of the worn 420 SSC surfaces deposited by (a) EEDS, (b) HVAS [1.9]

431 SSC deposited by FS process [1.10] gave the following results: a thickness of 414 μm, a porosity of 2.2%, oxides amount of 21%, a hardness of H=303 $HV_{0.3}$, a COF of μ=0.65 and a

wear rate of $k=4.4\cdot10^{-4}$ $mm^3/N\cdot m$. An observation on the wear tracks showed in **Figure 1.6** suggests that the oxidation wear is the main wear mechanism.

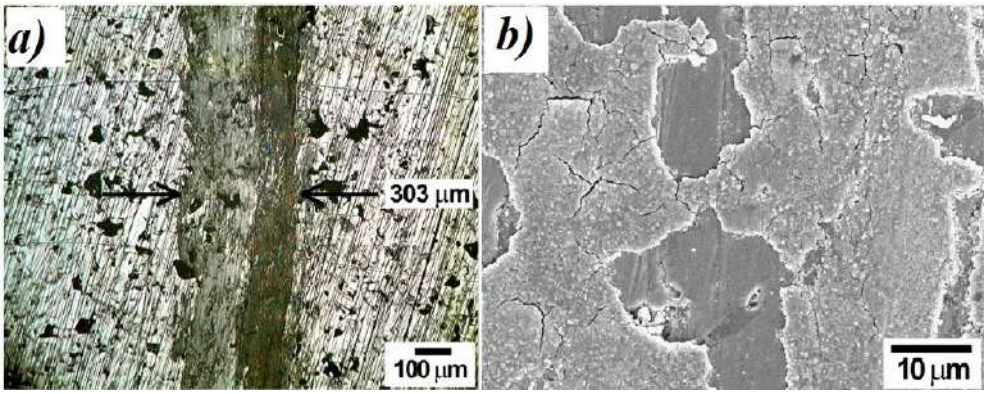


Figure 1.6 Wear tracks observations on 431 SSC by (a) OM, (b) SEM [1.10]

The amorphous SSC ($Fe_{44.6}Cr_{28}Mn_{0.8}Mo_{2.5}C_{7.6}Si_{2.4}Ni_{14.1}$ (at.%)) [1.12] deposited by HVAF with 500 µm of thickness exhibited two types of wear mechanisms: delamination and oxidation (**Figure 1.7**). The obtained coating displayed a dense microstructure with high hardness (between H=8.5 GPa to H=8.9 GPa) and low porosity (around 1%). The COF had large fluctuation between µ=0.8 and µ=0.9. Another interesting point from the obtained coating was the slight decrease in the COFs range of values when increasing the normal load (for the normal loads of F=10 N, F=20 N, F=30 N and F=40 N the COFs are ranged respectively between µ=0.51 to µ=0.81, µ=0.51 to µ=0.81, µ=0.51 to µ=0.75 and µ=0.51 to µ=0.74) and that is related to the flash temperature increasing which can be generated during the sliding process, causing more oxide debris and leading to a larger area of oxide layers that can be considered as a self-lubricating oxide layer.

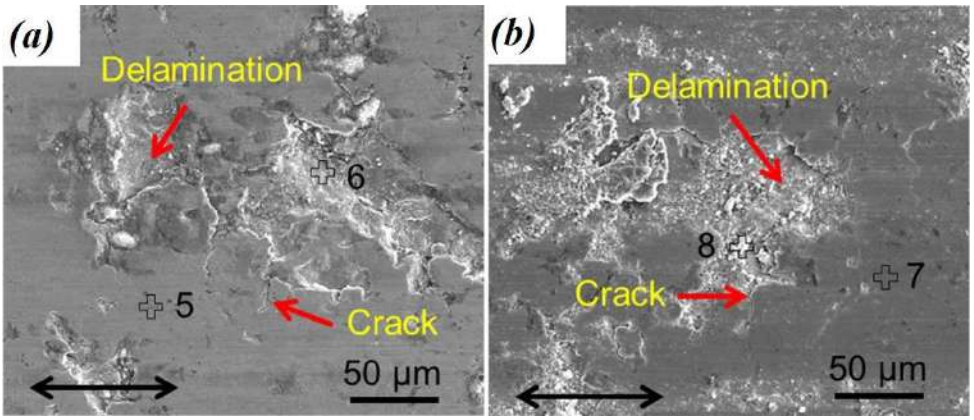


Figure 1.7 Wear tracks images of amorphous SSC under: (a) F=10 N, (b) F=40 N [1.12]

304L SSC deposited by CGDS was reported by [1.13, 1.14]. SEM images of the coating surface highlighted cellular-like morphologies (**Figure 1.8 (a)**). Such morphologies gave the coating surface a rough aspect. The Cross-section images (**Figure 1.8 (b)**) presented a dense morphology with lamella structures, some pores and interlamellar cracks. The interlamellar cracks are obtained owing to the lack of the bonding between the adjacent deposited layers.

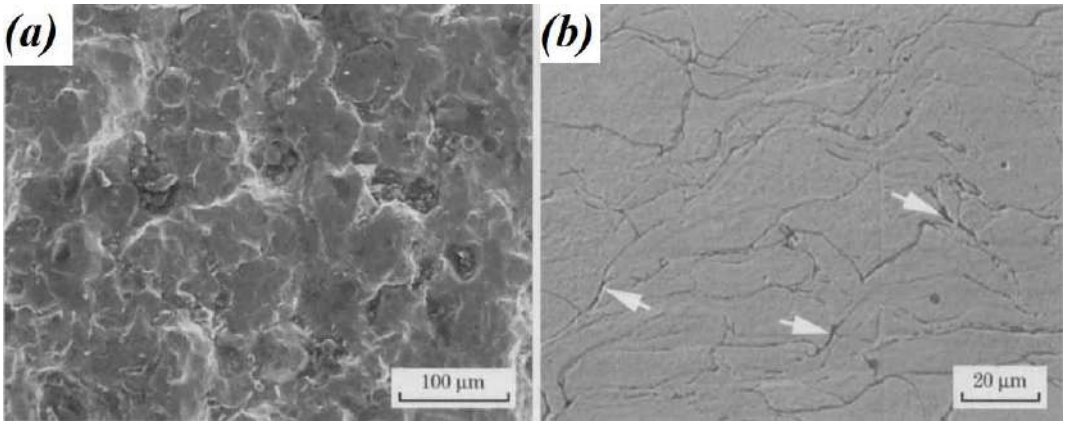


Figure 1.8 SEM images of 304L SSC: (a) top surface, (b) cross-section [1.14]

The obtained elastic modulus of the coating is about E=117.9 GPa [1.13] which was slightly lower than that of the bulk 304L stainless steel (about E=200 GPa). The main reason for such reduction is the existence of pores and defects in the coating. The low corrosion resistance of the coating in comparison with the bulk material can be attributed to the oxidation of some

alloyed elements especially chromium leading to the formation of chromium depleted areas that impairs the corrosion resistance [1.14].

1.2. Enhancing the SSCs using multilayers

In order to get better thermal sprayed SSCs, two characteristics must be optimised: the coating density that can be enhanced through the post-spray heat treatment and the coating thickness [1.5]. According to what was reported before about the optimization of the SSC thicknesses, two methods were used:

1. Variation in the deposition velocity at a constant period [1.15, 1.16]: with increased velocity, the final thickness decrease. The coating properties when using this method were not extensively studied, only the coating porosity and the corrosion resistance were reported, with no porosity variation (about 4%) and with a corrosion resistance similar to that of the stainless steel bulk material when a coating with a higher thickness was deposited (305 µm that corresponded to the deposition velocity of 50 mm/s) [1.15].

2. Variation in the coating number of layers at constant deposition parameters [1.5, 1.17-1.19]: where the number of layers were varied from 2 layers to 4 layers. The coating thickness increased with the number of layers.

By increasing the number of layers, the density of the coating is improved due to the accumulative deformation after the impact of the deposited particles on the surface of the previous layers, resulting in the coatings mass gain increase, and the reduction in porosity and defects due to the compacting effect of the layers that deposited on the top of the others as presented in **Figure 1.9** [1.17]. It is good to notice that the cavities between layers' boundaries as presented in **Figure 1.9** are not coating porosities but the external roughness of the previous layers [1.5].

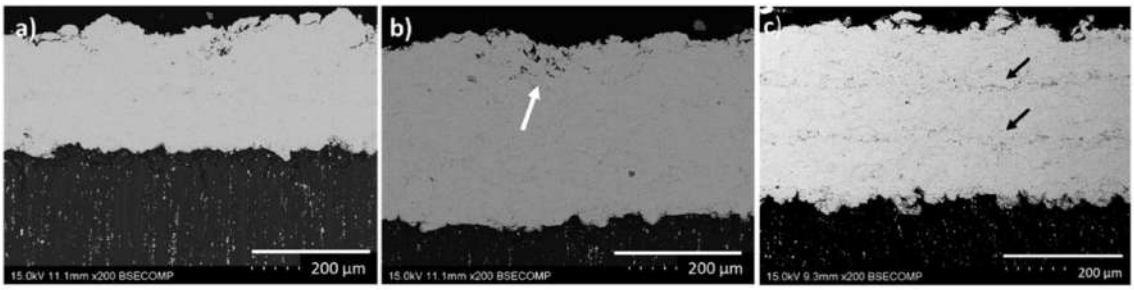


Figure 1.9 Cross-section images for 316L SSC with: (a) 2 layers, (b) 3 layers, (c) 4 layers [1.5]

In the SSCs multilayers, oxides can be existed in two different forms: those between the different sprayed layers and those surrounding the semi-melted particles. The first form is deposited due to the exposure of each layer to the oxidizing effect of the spraying flame after their deposition [1.17]. Oxides are the preferred locations for the cracks generation and propagation, but that is not true in the case of the first form of oxides because the cracks propagation has the same preferred direction with that of the applied force, and the oxides between layers forms a continuous line in the perpendicular direction [1.17]. This suggestion is illustrated in **Figure 1.10**. In the contrary, the inter-particles boundaries oxides are the most susceptible locations for the cracks propagation [1.19].

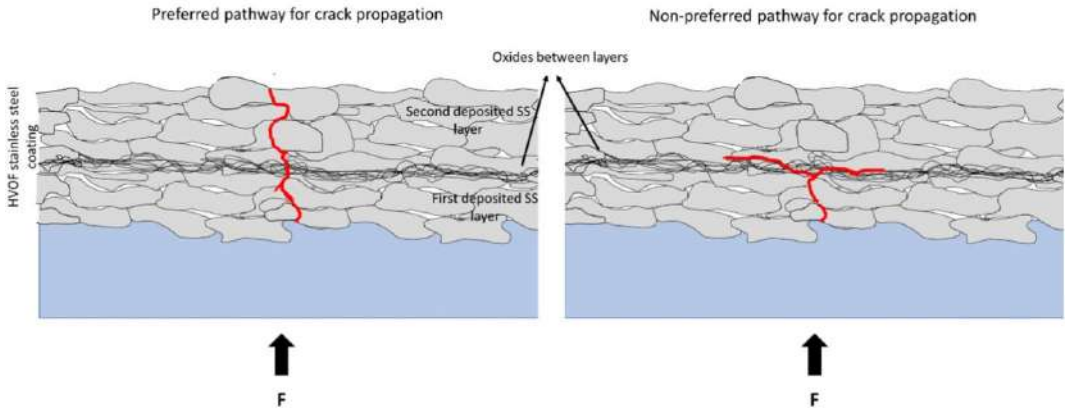


Figure 1.10 Pathway to the crack propagation in the multilayers coatings [1.17]

It is remarkable that the ferrite phase increased with the number of layers and that can be attributed to the increasing in the heat exposure during the deposition of each layer, so a heat treatment will be produced each time and the transformation rate of austenite into ferrite

increases [1.17, 1.19]. Another explanation [1.19] suggests that the local changes in the chemical composition of the coating due to the oxidation of the alloying elements such as chromium and nickel can reduce the stability of the austenite phase and induces their transformation into ferrite phase.

It was observed that the hardness also increased with the number of layers from H=349 $HV_{0.1}$ for the 2 layers coating to H=392 $HV_{0.1}$ for the 3 layers coating and H=433 $HV_{0.1}$ for the 4 layers one [1.17]. The increase in the hardness of the different coatings can be related to the increase in the coating compactness with each layer addition [1.5] due to the effect of depositing each layer above the other, leading to their deformation and the reduction in their porosity and the increase in their density [1.17]. Another interesting result is that the hardness of the multilayer coating was higher than that of the bulk material and that is due to the generation of the quenching stresses after the rapid cooling and solidification of the molten particles, the generation of the thermal stresses after the cooling of the system coating/substrate is due to the difference in TECs between the substrate and the coating. Finally, the hardness is increased due to the generation of compression stresses after the plastic deformation of the substrate and/or the previous layers' surface due to the high velocity impact of the sprayed particles [1.17].

The electrochemical test results indicate that R_p of the mono layer coating was even lower than that of the substrate (45.6 Ω/cm^2 after 168h) but after increasing the number of layers, potential resistance was too high, either for the 2 layers coating (1271 Ω/cm^2 after 168h) or the 3 layers one (7515 Ω/cm^2 after 168h) [1.5]. Observations on the corroded coating cross-sections after 168h of the test (**Figure 1.11**) revealed that with 1 layer only, the substrate corrosion products were seen and there were no signs of the SSC corrosion products in the corroded zone. For the 2 layers coating, the coating top surface seemed undamaged with the

stainless steel corrosion products. Cross section images showed the detachment of the coating (dark zone) due to the formation of the substrate corrosion products in the interface. With 3 layers, the coating was still present and perfectly attached to the substrate with the absence of any corrosion products in the interface. The maximum penetration of the electrolyte was about 57 µm which means that there was still about 300 µm of coating to protect the substrate for another 48 days [1.5].

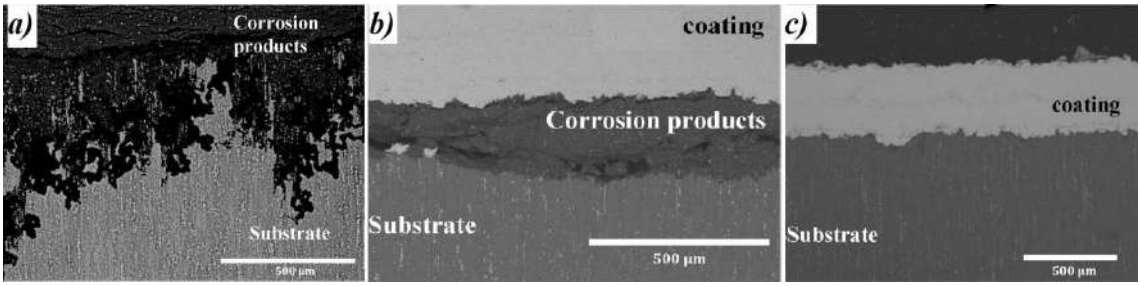


Figure 1.11 Cross-section images of the corroded SSC with: (a) 1 layer, (b) 2 layers, (c) 3 layers [1.5]

The above results suggest that the corrosion is progressed from the substrate after the electrolyte reaches it across the interconnected pores. Also chloride anions have the ability to deform the metallic crystalline structure with lower compactness and to open a path for the electrolyte to reach the substrate. Pitting corrosion on the substrate surface is built up in the first contact with the electrolyte, causing a high i_{corr} after the first hour of the test. The formation of corrosion products inside the coating cracks increase the coating volume causing the spallation of the coating. With the increase in the coating thickness, the formation of the interconnected pores is lowered and the amount of the electrolyte that can reach the substrate will be low and the growth of the corrosion products will be not sufficient to break the coating, the delaying in the entrance of more electrolyte causes a reduction in the corrosion resistance [1.5].

Other electrochemical results showed that the 4 layers coating gave the best corrosion results such as E_{OC} (-1.01 V for the 1 layer, -0.96 V for the 2 layers, -0.89 V for the 3 layers and -

0.19 V for the 4 layers) and i_{corr} (93 µA/cm^2 for the 1 layer, 9.5 µA/cm^2 for the 2 layers, 7.7 µA/cm^2 for the 3 layers and 4.6 µA/cm^2 for the 4 layers) [1.18].

1.3. Enhancing the SSCs by the post-spray annealing

According to what was reported before, it can be concluded that the annealing treatment has two major effects on the SSCs microstructures [1.20]:

(i) Eliminating the microstructure anisotropy through the phases transformation;

(ii) Enhancing the inter-particles bounding.

Using the OM (**Figure 1.12**), the transformation of austenite into ferrite was remarkable in the Fe-316L SSC deposited by CGDS process [1.21] through the absence of lighter phases. XRD analysis confirmed the transformation of austenite.

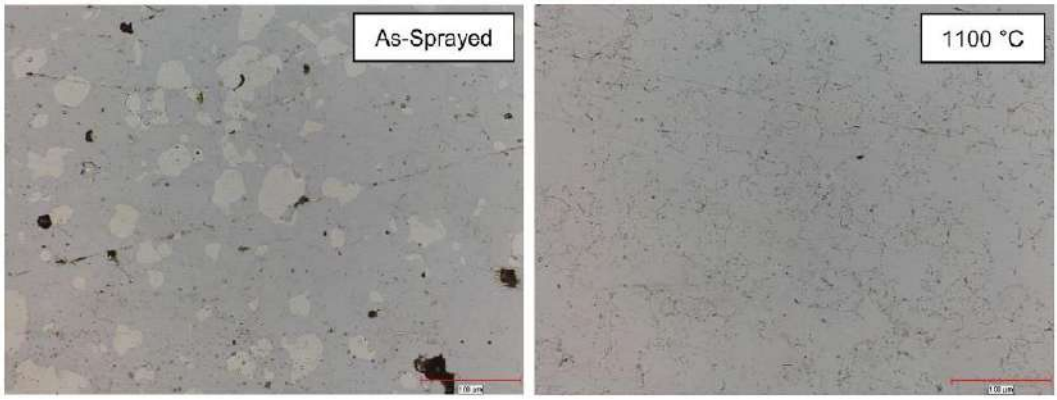


Figure 1.12 Surface images of the as-sprayed Fe-316L SSC and the annealed one at 1100°C [1.21]

The transformation of austenite into ferrite can be explained in this case by the nickel diffusion from the 316L stainless steel regions into the iron regions during annealing. Any remained austenite after annealing can be revealed to the incomplete nickel diffusion [1.21]. The above observations and explanations can be generalized for any SSC on an ordinary steel or iron substrate.

When air annealing method was used [1.22], high amount of oxides can be expected on the SSCs such as: Mn_2CrO_4, Cr_2O_3 and SiO_2 and that is related to oxygen penetration inside the inter-particle boundaries during the air annealing. Those oxides play a barrier role to the formation of the inter-splats bounding, causing weak particles cohesion and low coating properties.

The improvement in the inter-particles bounding as a result of other annealing methods is owing to the grains recrystallization which induce atoms diffusion into the inter-splats [1.21], and as a result, the dislocations exist within the crystalline structure will be removed, and the SSC become soft with high ductility and good tensile strength, and so many properties will be enhanced like the electrical conductivity and the corrosion resistance [1.22].

Annealing 304L SSC deposited by CGDS process at 600°C [1.20] changeed its surface microstructure from the one with high deformed particles into a dense microstructure. At 800°C some particles interfaces were still observed and at 950°C, grain sizes became larger and the inter-splats boundaries were no longer observed (**Figure 1.13**).

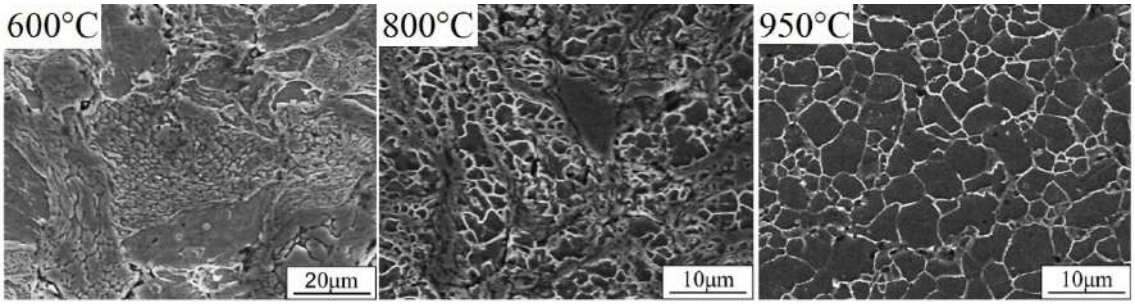


Figure 1.13 Cross-section images of the annealed 304L SSC at 600 °C, 800 °C and 950 °C [1.20]

A comparison between the different annealing methods at 1000°C [1.22] revealed that HIP method gave the densest coating with no visible pores and inter-particles boundaries, while air annealing showed a microstructure similar to that of the as-sprayed coating. By vacuum annealing method, only a slight reduction in porosity was observed. Such observations can be attributed to the diffusion of the material into the open pores which leads to their closing and

so the obtaining of small amount of pores. Pore sizes were differentiated from 70 µm with air annealing to 35 µm with vacuum annealing and 15 µm with HIP. While, further work [1.23] reported that pores were formed after air annealing and not before. These pores were reorganized and localized at the inter-splats boundaries leading to the impairment of the coating properties. As a conclusion, vacuum and HIP annealing methods gives the best microstructural aspect of the coating because of the absence of oxides inclusions [1.22], and so, high mechanical properties will be expected through those two methods (**Figure 1.14**).

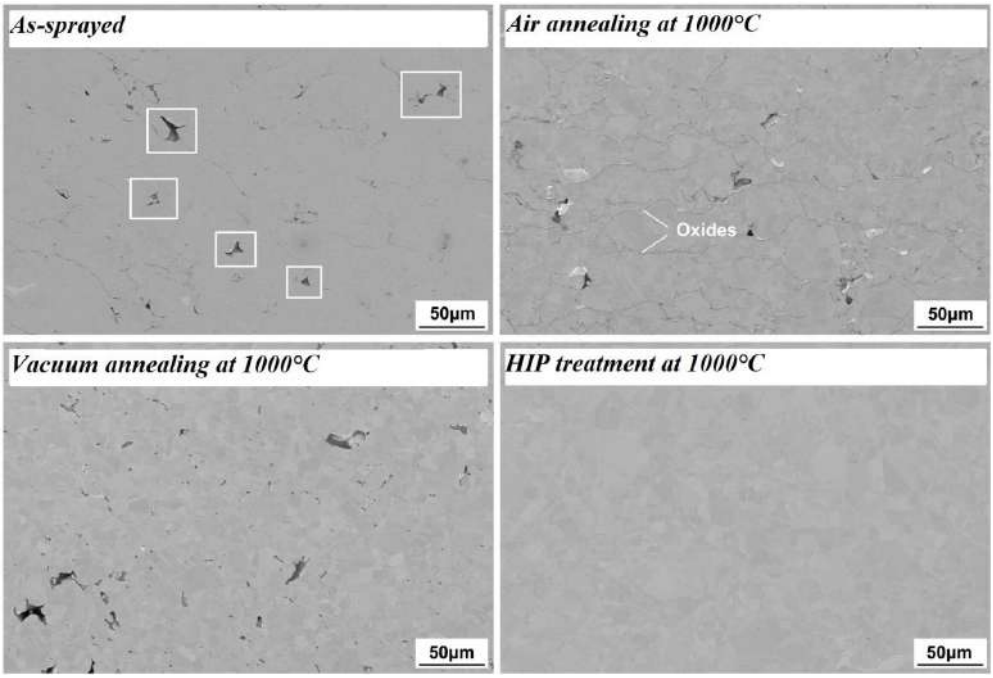


Figure 1.14 Cross-section images of the as-sprayed and the annealed 316L SSC at 1000 °C with air annealing, vacuum annealing and HIP [1.22]

Annealing at low temperatures such as 300°C [1.20] and 400°C [1.23] had no effect on the SSCs properties. In general, for 304L SSC, the recommended annealing temperatures are in the range of 1010 °C and 1120°C [1.24], and below 500°C, the SSCs properties are similar to the as-sprayed one [1.23].

After annealing 304L SSC at 1050°C with air annealing method, the hardness was reduced from H=450-459 $HV_{0.2}$ into H=144-161 $HV_{0.2}$ which was close to the typical hardness of the

annealed 304L bulk material [1.23]. The same reduction in the hardness was obtained for the same coating annealed at 950°C, from H=345 $HV_{0.2}$ for the as-prayed coating to H=201 $HV_{0.2}$ for the annealed one [1.20]. The high hardness of the as-sprayed coating is related to the generation of the dislocations density increments that occurs on the SSCs during their deposition. The recrystallization of the coating leads to the elimination of dislocations and the growth of the grains and so the reduction of the hardness [1.22].

Comparing the hardness results of 316L SSCs using three different annealing methods at 1000°C showed that the hardness of the as-sprayed coating was about H=255 $HV_{0.5}$ and then it reduced into H=170 $HV_{0.5}$ with air annealing method and H=150 $HV_{0.5}$ with vacuum annealing method and H=180 $HV_{0.5}$ with HIP method [1.22].

Cracks in SSCs initiate generally in the inter-splats boundaries, then they propagate along the interface vertically [1.20]. After annealing, and because of the atoms diffusion through these boundaries, cracks nucleation sites will be reduced.

Electrochemical test results revealed low corrosion rates for the annealed SSCs at vacuum conditions with temperatures of 1200°C and 1300°C and they were in the order of 0.1 mpy which represented a reduction of approximately 43% in comparison with the as-sprayed coating [1.21]. Such reduction in corrosion rate can be attributed to the decreased porosity and the strengthening of the inter-splats boundaries, and that can be related to the fact that the corrosion starts first around them [1.21].

1.4. PIII Nitriding

When nitriding stainless steels at a low range of temperatures between 350-400°C [1.25] or between 300-380°C [1.26], hard and wear resistant solid solutions of high nitrogen contents up to 30 at.% were formed, this phase is called the S-phase, the m-phase or the expanded

austenite, designed to by γ_N. The obtained S-phase is responsible for the hardness increasing [1.25] (between 10-15 GPa according to [1.26] and up to 17 GPa as reported by [1.27]), and the enhancement of the tribological properties (wear rate reduced from 2 [1.28] up to 3 orders of magnitude [1.26] and the COF is 60% lower than the untreated stainless steel surfaces [1.28]) and the corrosion behaviour [1.29], those obtained results are related to the remaining free nitrogen atoms in the solid solution without forming any nitride [1.30]. The heavy lattice distortion caused by the diffusion of nitrogen atoms is another explanation for the increased hardness [1.31].

Nitriding at a low range of temperatures can be obtained through different plasma nitriding processes such as: LEI, PIII or the conventional ion implantation [1.27]. PIII has many other denominations like: PBII and PIII&D [1.32].

PIII process consist of immersing the target (sample to be treated) inside a plasma atmosphere, then a high negative voltage pulses between 10 to 50 kV are applied repetitively on them. The plasma ions are accelerated into the target and then they will be implanted on it. Afterward, the ions are diffused inside the target and finally they form nitrides and change the target surface morphology [1.31]. The desired treatment temperature is achieved by adjusting the repetition frequency and the time duration of the high voltage pulses [1.33].

Plasma nitriding at high temperatures are not suitable for nitriding stainless steels, and low treatments below 400°C are necessary to prevent the formation of the chromium nitride CrN precipitates that removes chromium from the stainless steel solid solutions [1.32] that compromises the corrosion resistance [1.27]. Mandle et al. reported that even at 380°C, degraded corrosion resistance could be obtained [1.34]. Despite the corrosion resistance deterioration when nitriding at high temperatures, thicker nitride layers with higher wear resistance, hardness and elastic recovery can be obtained [1.28, 1.35].

With PIII process, the thickness of the nitrided layer grew as the implantation temperature increased starting from 300°C to 400°C [1.28]. An S-phase of tens of micrometers in thicknesses could be obtained at the implantation temperature of 400°C as reported by [1.30]. By applying PIII on the coatings, more stable coating properties could be obtained [1.36]. Lin et al. [1.30] have studied the effect of implantation temperature on the obtained surface hardness. They found that with increasing the implantation temperature, the surface hardness increased from H=8 GPa with 300°C, 15.5 GPa with H=400°C and H=17.5 GPa with 500°C. Farazmand et al. [1.31] have found also that with increasing the implantation temperature from 470°C to 570°C, the hardness was increased with about 21.5%. Their explanation for such increasing is that with raising the nitriding temperature, the nitrogen diffusion and the amount of the S-phase formation will be increased, especially above 540°C. Fu et al. In the contrary [1.36], reported a reduction in the hardness with temperatures between 300°C and 400°C. Lin et al. [1.30] have studied also the effect of the implantation duration on the obtained hardness and they have found that the hardness increased just slightly at 400°C from H=13 GPa in a duration of 1 hour, H=15.5 GPa in 2 hours duration and H=16 GPa in 3 hours duration. Farazmand et al. [1.31] have found that after rising the time to 3 hours the hardness increases by 14% [1.31]. As a conclusion, they arrive to the fact that the increase in the temperature is more effective than the increase in the implantation duration. On the contrary, the elastic modulus is remaining constant at different implantation temperatures and durations [1.30].

The COF values were decreased as the implantation temperature increased up to μ=0.22 at 400°C [1.28], such a reduction can be attributed to the surface hardening and the increase in the nitrided layer thickness with the temperature. The increase in nitrides amount reduces the adhesion and the plastic deformation between the antagonist surfaces, resulting in lower COFs

[1.28]. The wear rate was also reduced with the increased implantation temperature and duration [1.31]. As the temperature increased from 300°C to 400°C, the wear mechanism transition was observable from adhesive wear to abrasive wear [1.28] (**Figure 1.15**).

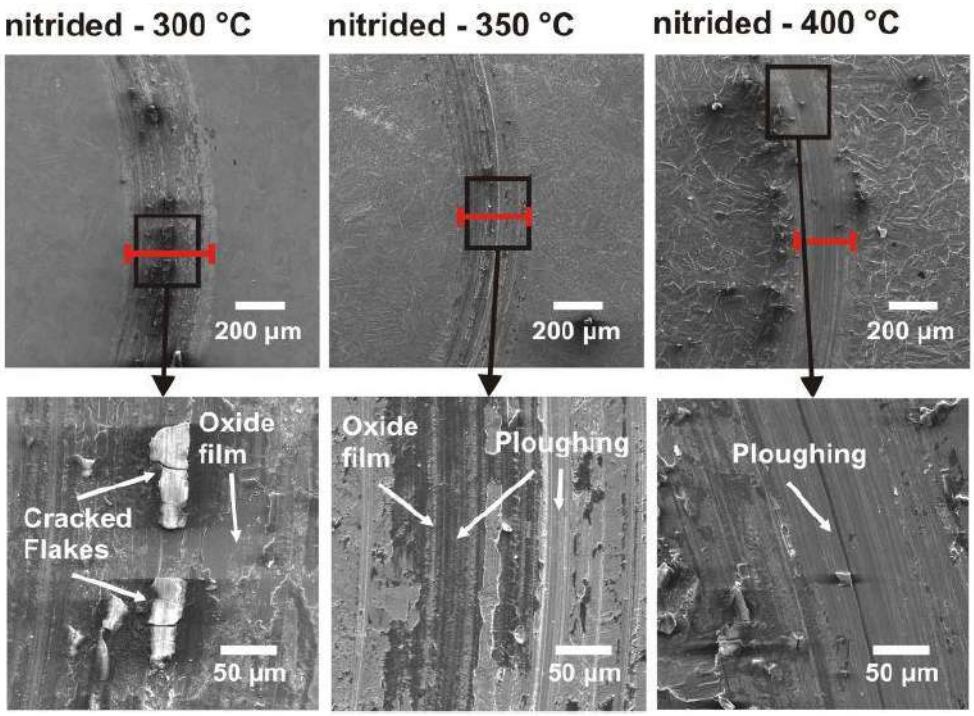


Figure 1.15 Wear mechanisms for the PIII nitrided supermartensitic stainless steel at different temperatures [1.28]

Fu et al. [1.36] have studied the effect of the implantation temperature on the corrosion behaviour of the 420 stainless steels. All the treated samples showed higher corrosion resistance than the untreated one. The i_{corr} results were $6.11 \cdot 10^{-4}$ A, $4.10 \cdot 10^{-4}$ A, $8.25 \cdot 10^{-4}$ A, $1.11 \cdot 10^{-3}$ A and $2.03 \cdot 10^{-3}$ for respectively room temperature, 300°C, 400°C, 500°C and the untreated material. As a conclusion, higher implantation temperatures give lower corrosion resistances. Longer nitriding durations as reported by Mandle et al. [1.34], gives better corrosion resistance while there is no correlation between the nitrided layer thickness with the corrosion resistance.

1.5. W-Ti-N thin films

W-Ti-N thin film is one of the most interesting thin films that is generally studied for diffusion barriers applications in the integrated circuits [1.37-1.39] and in mechanical applications for high speed cutting tools [1.40] and in tribology for the internal combustion engines pistons [1.41].

Sharginyan et al. [1.42] have studied the W-Ti-N thin film as a function of the Ar/N_2 partial pressures at a total pressure of 0.5 Pa. The thin film composition analysis revealed that there were three ranges of the films according to their nitrogen concentrations:

- At very low nitrogen concentrations varied between 0 to 3 at.%, the film was consisted of inhomogeneous microstructure. For the part adjacent to the substrate, it was consisted of small crystallites, while the upper part had larger ones.

- At nitrogen concentrations in the range of 12-28 at.%, the grains sizes decreased. The reason behind such microstructure transformation is the presence of the chemically active nitrogen that is concentrated in the boundaries between the W grains and the structure defects inside the grains, thereby, in those areas, where the nitride phases can be formed. With such nitrogen concentration, the volume of nitride phase is small and a destruction of the continuous and the dense surface along with the W grains boundaries and inside their defects are observed. The higher the nitrogen concentrations are, the higher nitrides filled up the W grains, and accordingly the size of the W grains would decrease. Finally, when the nitrogen atoms concentration on the grown surface is equal or above the concentration of the W atoms, only the nitride nuclei arise on the surface and only the nitride film will grow.

- At higher nitrogen concentrations $[N_2]>36$ at.%, the thin film grain sizes were increased again.

It was found also elsewhere [1.39] that the oxygen content within the W-Ti-N thin film decreased with increasing the nitrogen concentration and that is related to the increase in the thin film density.

The hardness measurements at different N_2/Ar partial pressures showed that a hardness of H=49 GPa was obtained at N_2/Ar=1/5 and of H=40.3 GPa at N_2/Ar=1/3 [1.43]. The same authors found a hardness maximum value of 45 GPa at nitrogen content up to 35 at.% and that it was decreased thereafter [1.44]. The distortion of the b.c.c. α-(W, Ti) lattice by nitrogen incorporation in the interstitial position is the reason why the hardness increases with increasing the nitrogen content [1.44]. The same hardness trend was reported by Sharginyan et al. [1.42] with decreased hardness values at higher nitrogen content than 30 at.%. The decreasing in the hardness from a certain point can be related to the electronically induced lattice softening as a result of the anti-bonding states generation [1.42].

The tribological results showed high COFs of μ=0.78 and μ=1.0 with N_2/Ar=1/5 and N_2/Ar=1/2 respectively [1.43], while at N_2/Ar=1/20 and N_2/Ar=1/3, the best COFs were obtained with μ=0.57 and μ=0.68 respectively [1.44].

Figure 1.16 presents the wear track profiles for W-Ti-N films at different N_2/Ar partial pressures ratios. Some positive parts can be seen in the wear tracks, indicating the adhesive wear. The grooves are indications of the abrasive wear. For the film at N_2/Ar=1/5, the wear tracks showed the typical abrasive aspect and the film at N_2/Ar=1/3 and N_2/Ar=0 (W-Ti film) showed very smooth surfaces [1.44].

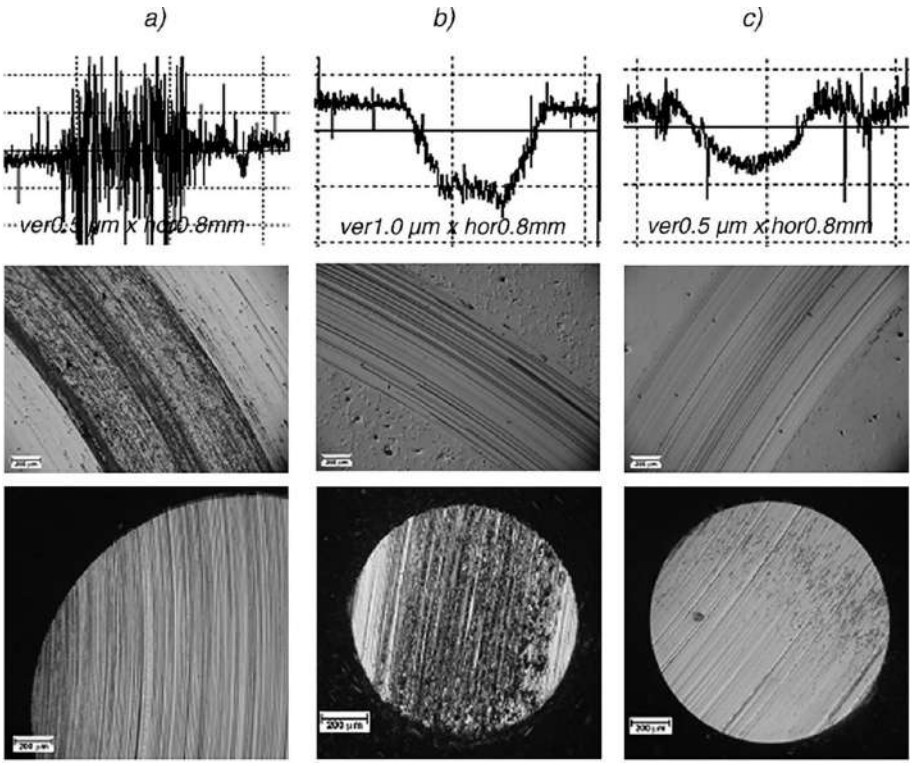


Figure 1.16 Wear track profiles and micrographs in the disk and crater in the ball for W-Ti-N films deposited with N_2/Ar ratios of: (a) 1/ 3, (b) 1/5 and (c) 0 [1.44]

The most interesting results in tribology point of view are those reported by Chemaa et al. [1.41]. The authors have studied the mechanical and the tribological properties of W-Ti-N thin film and of W-Ti-N/Al-Si multilayer at N_2/Ar=1/20 and they found in both studies COFs of μ=0.08 which represent one of the lowest reported COFs for the hard thin films (**Figure 1.17**).

Despite the interesting COF, the hardness of the first thin film was very low (H=7.1 GPa) and higher for the W-Ti-N/Al-Si multilayer (H=17.2 GPa) due to the high mismatch of the TECs between the W-Ti-N thin film (W-based film TEC is in the range of $4\text{-}9\cdot10^{-6}$ K^{-1}) and the Al-Si thin film (Al thin film TEC is $23.1\cdot10^{-6}$ K^{-1}) in comparison with that between the W-Ti-N thin film and the stainless steel substrate (stainless steel TEC is $18\cdot10^{-6}$ K^{-1}).

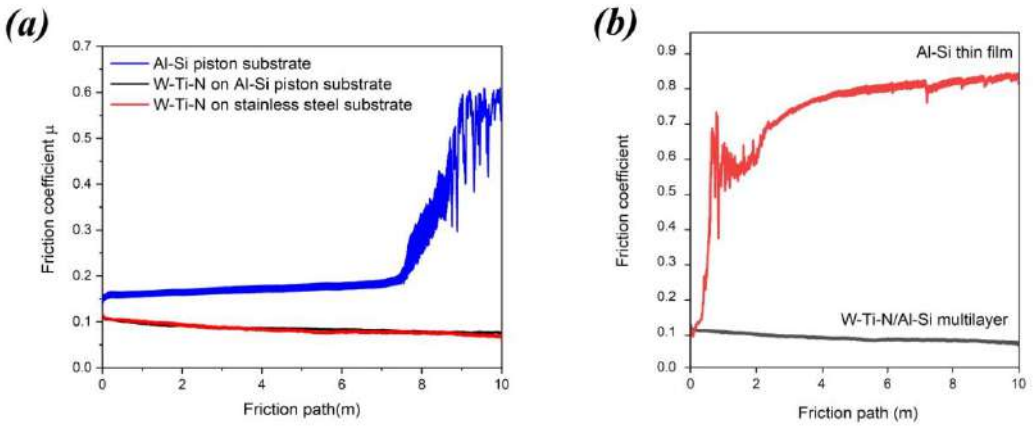


Figure 1.17 friction curves of: (a) W-Ti-N thin film on two different substrates, (b) W-Ti-N/Al-Si multilayer and the Al-Si thin film [1.41]

Braga et al. [1.45] have studied the behaviour of the duplex treatment: plasma nitriding + W-Ti-N thin film with and without the white layer formation. Duplex treatments are used generally to combine the excellent properties of nitriding with the high hardness of the hard films such as W-Ti-N thin film. The microstructural characterization showed that the main difference between the W-Ti-N thin film that was deposited on the nitrided and on the non nitrided substrates was the loss of the (200) preferential orientation in the favour of the (111) orientation. The comparison between the films micrographs with and without the formation of the white layer (**Figure 1.18**) showed that in the first case, a very nice continuity was found between the film and the nitrided layer, while in the second case, dark, thin and irregular interlayer could be seen underneath the film. In reality, the white layer can be considered as the main problem for the duplex treatments because during the film deposition, it can be transformed into ferrite that can alter the adhesion of the film.

The hardness measurements revealed that the hardness of the duplex treatment was lower than that of the simple W-Ti-N thin film. Such result can be related to two reasons:

- The decrease in the (200) preferential orientation in the favour of the (111);

- The low compressive stresses level due to the low difference in the TECs between the nitrided steels and the W-based films in comparison to the non nitrided steels.

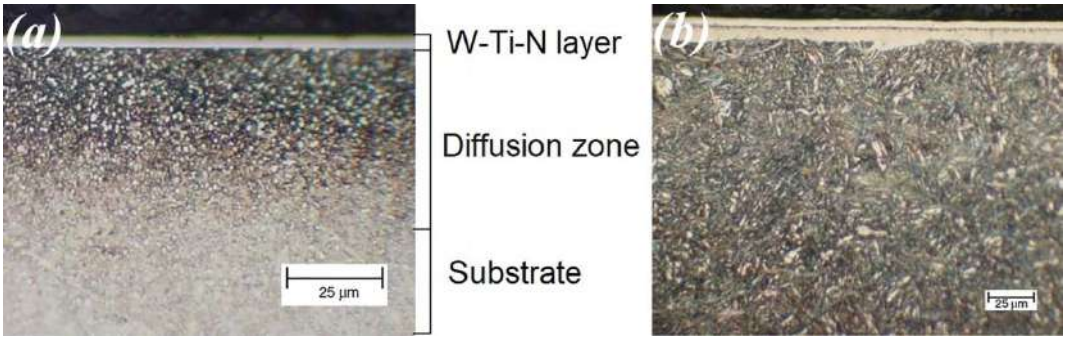


Figure 1.18 (a) Micrograph of W-Ti-N film on nitrided substrate without white layer, (b) Micrograph of W-Ti-N on nitrided substrate with white layer [1.45]

References

[1.1] L. Zhao and E. Lugscheider, Influence of the spraying processes on the properties of 316L stainless steel coatings, *Surf. Coat. Technol.*, 2002, **162**, p 6-10.

[1.2] B. Sun, H. Fukanuma and N. Ohno, Study on stainless steel 316L coatings sprayed by a novel high pressure HVOF, *Surf. Coat. Technol.*, 2014, **239**, p 58-64.

[1.3] P.H. Suegama, C.S. Fugivara, A.V. Benedetti, J. Fernández, J. Delgado and J.M. Guilemany, Electrochemical behavior of thermally sprayed stainless steel coatings in 3.4% NaCl solution, *Corrosion Sci.*, 2005, **47**, p 605-620.

[1.4] M. Villa, S. Dosta and J.M. Guilemany, Optimization of 316L stainless steel coatings on light alloys using cold gas spray, *Surf. Coat. Technol.*, 2013, **235**, p 220-225.

[1.5] S. García-Rodríguez, A.J. López, B. Torres and J. Rams, 316L stainless steel coatings on ZE41 magnesium alloy using HVOF thermal spray for corrosion protection, *Surf. Coat. Technol.*, 2016, **287**, p 9-19.

[1.6] E.P. Song, B. Hwang, S. Lee, N.J. Kim and J. Ahn, Correlation of microstructure with hardness and wear resistance of stainless steel blend coatings fabricated by atmospheric plasma spraying, *Mater. Sci. Eng. A*, 2006, **429**, p 189-195.

[1.7] J.M. Guilemany, J. Fernández, N. Espallargas, P.H. Suegama and A.V. Benedetti, Influence of spraying parameters on the electrochemical behaviour of HVOF thermally sprayed stainless steel coatings in 3.4% NaCl, *Surf. Coat. Technol.*, 2006, **200**, p 3064-3072.

[1.8] Y. Chen, B. Xu, Y. Liu, X. Liang and Y. Xu, Structure and sliding wear behavior of 321 stainless steel/Al composite coating deposited by high velocity arc spraying technique, *Transactions Nonferrous Metals Soc. China*, 2008, **18**, p 603-609.

[1.9] G. Jin, B. Xu, H. Wang, Q. Li and S. Wei, Microstructure and tribological properties of stainless steel coatings sprayed by two methods based on spraying, *Surf. Coat. Technol.*, 2007, **201**, p 5261-5263.

[1.10] D. Kaewsai, A. Watcharapasorn, P. Singjai, S. Wirojanupatump, P. Niranatlumpong and S. Jiansirisomboon, Thermal sprayed stainless steel/carbon nanotube composite coatings, *Surf. Coat. Technol.*, 2010, **205**, p 2104-2112.

[1.11] P.H. Gao, S.T. Cao, J.P. Li, Z. Yang, Y.C. Guo and Y.R. Wang, High temperature oxidation resistance of M42C stainless steel coatings deposited on the surface of cast iron through atmospheric plasma spraying, *J. Alloys Compounds*, 2016, **684**, p 188-194.

[1.12] H. Guo, S. Zhang, W. Sun and J. Wang, Differences in dry sliding wear behavior between HVAF-sprayed amorphous steel and crystalline stainless steel coatings, *J. Mater. Sci. Technol.*, 2019, **35**, p 865-874.

[1.13] W. Han, X. Meng, J. Zhang and J. Zhao, Elastic modulus of 304 stainless steel coating by cold gas dynamic spraying, *J. Iron Steel Res. International*, 2012, **19**, p 73-78.

[1.14] X. Meng, J. Zhang, W. Han and J. Zhao, Fracture behavior of cold sprayed 304 stainless steel coating during cold rolling, *J. Iron Steel Res. International*, 2012, **19**, p 57-63.

[1.15] K. Spencer and M. Zhang, Optimisation of stainless steel cold spray coatings using mixed particle size distributions, *Surf. Coat. Technol.*, 2011, **205**, p 5135-5140.

[1.16] D. Kotoban, S. Grigoriev, A. Okunkova and A. Sova, Influence of a shape of single track on deposition efficiency of 316L stainless steel powder in cold spray, *Surf. Coat. Technol.*, 2017, **309**, p 951-958.

[1.17] S. García-Rodríguez, B. Torres, A.J. López, E. Otero and J. Rams, Characterization and mechanical properties of stainless steel coatings deposited by HVOF on ZE41 magnesium alloy, *Surf. Coat. Technol.*, 2019, **359**, p 73-84.

[1.18] S. García-Rodríguez, B. Torres, N. Pulido-González, E. Otero and J. Rams, Corrosion behavior of 316L stainless steel coatings on ZE41 magnesium alloy in chloride environments, *Surf. Coat. Technol.*, 2019, **378**, 124994.

[1.19] M. Moshref-Javadi, H. Edris, A. Shafyei, H. Salimi-Jazi and E. Abdolvand, Evaluation of hydrogen permeation through standalone thermally sprayed coatings of AISI 316L stainless steel, *International J. Hydrogen Energy*, 2018, **43**, p 4657-4670.

[1.20] X.M. Meng, J.B. Zhang, W. Han, J. Zhao and Y.L. Liang, Influence of annealing treatment on the microstructure and mechanical performance of cold sprayed 304 stainless steel coating, *Appl. Surf. Sci.*, 2011, **258**, p 700-704.

[1.21] J. Frattolin, R. Roy, S. Rajagopalan, M. Walsh, S. Yue, O.F. Bertrand and R. Mongrain, A manufacturing and annealing protocol to develop a cold-sprayed Fe-316L stainless steel biodegradable stenting material, *Acta Biomaterialia*, 2019, **99**, p 479-494.

[1.22] S. Yin, J. Cizek, X. Yan and R. Lupoi, Annealing strategies for enhancing mechanical properties of additively manufactured 316L stainless steel deposited by cold spray, *Surf. Coat. Technol.*, 2019, **370**, p 353-361.

[1.23] P. Coddet, C. Verdy, C. Coddet, F. Debray and F. Lecouturier, Mechanical properties of thick 304L stainless steel deposits processed by He cold spray, *Surf. Coat. Technol.*, 2015, **277**, p 74-80.

[1.24] J. Douthett, Heat treating of stainless steels, *ASM metals handbook volume 1 heat treating*, ASM international, NY, 1991.

[1.25] Y. Jirásková, S. Havlíček, O. Schneeweiss, V. Peřina and C. Blawert, Characterization of iron nitrides prepared by spark erosion plasma nitriding and plasma immersion ion implantation, *J. Magnetism Magnetic Mater.*, 2001, **234**, p 477-488.

[1.26] J. Lutz, J.W. Gerlach and S. Mändl, PIII nitriding of fcc-alloys containing Ni and Cr, *physica status solidi*, 2008, **205**, p 980-984.

[1.27] S. Mändl, Nitriding of Stainless Steel: PIII or Low Energy Nitriding?, *Plasma Processes Polymers*, 2007, **4**, p 239-245.

[1.28] B.C.E.S. Kurelo, W.R. DeOliveira, F.C. Serbena and G.B. DeSouza, Surface mechanics and wear resistance of supermartensitic stainless steel nitrided by plasma immersion ion implantation, *Surf. Coat. Technol.*, 2018, **353**, p 199-209.

[1.29] W.R. DeOliveira, B.C.E.S. Kurelo, D.G. Ditzel, F.C. Serbena, C.E. Foerster and G.B. DeSouza, On the S-phase formation and the balanced plasma nitriding of austenitic-ferritic super duplex stainless steel, *Appl. Surf. Sci.*, 2018, **434**, p 1161-1174.

[1.30] J.F. Lin, K.W. Chen, C.C. Wei and C.F. Ai, The effects of differing nitrogen implantation conditions on penetration depth, mechanical properties and tribological behavior of plasma-nitrided AISI 304 stainless steel, *Surf. Coat. Technol.*, 2005, **197**, p 28-38.

[1.31] M.H. Farazmand, H. Khorsand and H. Ebrahimnezhad-Khaljiri, The Effect of the Plasma-Nitriding Process on the Structure and Wear Properties of the Sintered Low Alloy Steel, *Metallography Microstructure Anal.*, 2018, **7**, p 711-723.

[1.32] J.A. García and R.J. Rodríguez, Ion implantation techniques for non-electronic applications, *Vac.*, 2011, **85**, p 1125-1129.

[1.33] K. Kostov, M. Ueda, M. Lepiensky, P. Soares, G. Gomes, M. Silva and H. Reuther, Surface modification of metal alloys by plasma immersion ion implantation and subsequent plasma nitriding, *Surf. Coat. Technol.*, 2004, **186**, p 204-208.

[1.34] S. Mändl, D. Manova, H. Neumann, M.T. Pham, E. Richter and B. Rauschenbach, Correlation between PIII nitriding parameters and corrosion behaviour of austenitic stainless steels, *Surf. Coat. Technol.*, 2005, **200**, p 104-108.

[1.35] R. Valencia, R. López-Callejas, A. Muñoz-Castro, S.R. Barocio, A.E. Chávez and O. Godoy-Cabrera, Nitriding of AISI 304 stainless steel by PIII in DC and RF toroidal discharges, *Brazilian J. Phys.*, 2004, **34**, p 1594-1597.

[1.36] R.K.Y. Fu, D.L. Tang, G.J. Wan and P.K. Chu, Enhancement of corrosion resistance of AISI 420 stainless steels by nitrogen and silicon plasma immersion ion implantation, *Surf. Coat. Technol.*, 2007, **201**, p 4879-4883.

[1.37] J.M. Oparowski, R.D. Sisson and R.R. Biederman, The effects of processing parameters on the microstructure and properties of sputter-deposited TiW thin film diffusion barriers, *Thin Solid Films*, 1987, **153**, p 313-328.

[1.38] H. Ramarotafika and G. Lemperiere, Influence of a D.C. substrate bias on the resistivity, composition, crystallite size and microstrain of WTi and WTi-N films, *Thin Solid Films*, 1995, **266**, p 267-273.

[1.39] R. S. Nowicki, J. M. Harris, M.A. Nicolet and I.V. Mitchell, Studies of the Ti-W/Au metallization on aluminum, *Thin Solid Films*, 1978, **53**, p 195-205.

[1.40] T. Hurkmans, T. Trinh, D.B. Lewis, J.S. Brooks and W.D. Münz, Multilayered titanium tungsten nitride coatings with a superlattice structure grown by unbalanced magnetron sputtering, *Surf. Coat. Technol.*, 1995, **76-77**, p 159-166.

[1.41] K. Chemaa, Y. Chabani, M. Gaceb and S. Hassani, "Study of tribological properties of titanium-based thin films applied to the rubbing parts of internal combustion engines piston", Master degree Thesis, M'hamed Bougara University Boumerdes, 2017.

[1.42] L. Shaginyan, M. Mišina, J. Zemek, J. Musil, F. Regent and V. Britun, Composition, structure, microhardness and residual stress of W-Ti-N films deposited by reactive magnetron sputtering, *Thin Solid Films*, 2002, **408**, p 136-147.

[1.43] P.N. Silva, J.P. Dias and A. Cavaleiro, Performance of W-Ti-(N) coated pins in lubricated pin-on-disk tests, *Surf. Coat. Technol.*, 2008, **202**, p 2338-2343.

[1.44] P.N. Silva, J.P. Dias and A. Cavaleiro, Tribological behaviour of W-Ti-N sputtered thin films, *Surf. Coat. Technol.*, 2005, **200**, p 186-191.

[1.45] D. Braga, J.P. Dias and A. Cavaleiro, Duplex treatment: W-Ti-N sputtered coatings on pre-nitrided low and high alloy steels, *Surf. Coat. Technol.*, 2006, **200**, p 4861-4869.

Chapter 2

Thermal spray and PVD technologies

2.1. Thermal spray

2.1.1. Introduction

Thermal spray is a deposition technique where molten, semi-molten or solid particles are deposited on the substrate surface. The spray process is the way to generate the stream of these particles. Thermal spray coatings are generated when these particles are plastically deformed when impacting the substrate [2.1].

The main advantage of the thermal spray is that the deposited particles are sprayed without melting the substrate. The substrate temperature during the spray rarely exceed 150°C even if the temperatures of the sprayed particles are higher than the solidus of the substrate material, because the solidification rate of the sprayed coatings is very high, and it is generally between 10^{-8} and 10^{-6} seconds [2.2].

The principle of the thermal spray is simply: a heat source (which can be a combustion flame, an electric arc, a plasma or an inert gas flow jets in the case CGS process) used to melt the

feedstock materials (powders or wires) and to accelerate the particles toward the surface of the substrate [2.3].

Heating and accelerating the sprayed particles are practical only if they occur in a stream of gas. The classification of the spray processes is based on the way to generate such stream or heat source. Spray processes can be classified also according to:

- Kinetic energy (velocity) of the sprayed particles and so according to their temperature and flight time.

- Atmosphere surrounding the gas stream (plasma or air). That atmosphere modifies the chemical composition of the gas stream and so the obtained properties of the coating.

- Production rate (high or low) and it is related to the volume of the sprayed material [2.1].

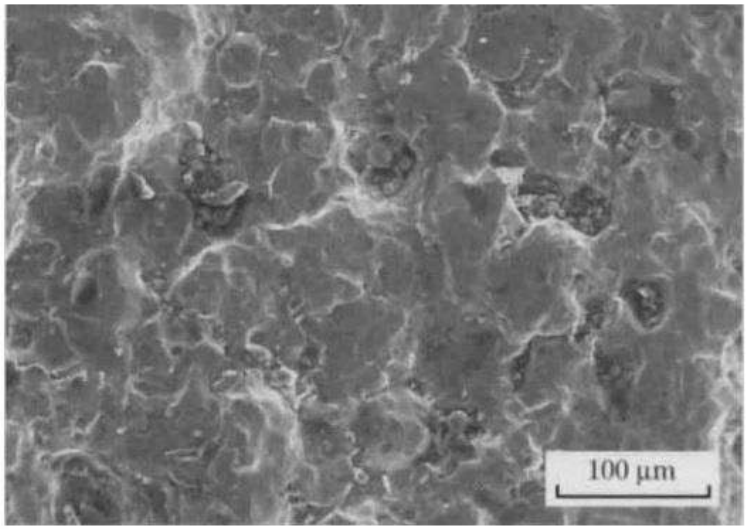


Figure 2.1 Splats deposited by CGDS [2.4]

During the particles flight time in the gas stream, they may interact with the surrounding medium and the oxidation may occur due to the high temperature of their active surface. When impacting the substrate surface, the sprayed particles form splats with forms that depend on their temperature and kinetic energy (**Figure 2.1**). Oxide layers around the molten particles will be dispersed and entrapped in fragments upon the impact which can be seen in

the metallurgical cross-sections as oxide inclusions between the lamellae structures formed by the various splats. The particles flight time is about 10^{-2} seconds which is much higher than the time necessary for solidification [2.2].

The mechanism of the bounding between the coating and the substrate is generally mechanical and as a result, each layer bounds with the previous one, forming the lamellae structure [2.5] (**Figure 2.2**).

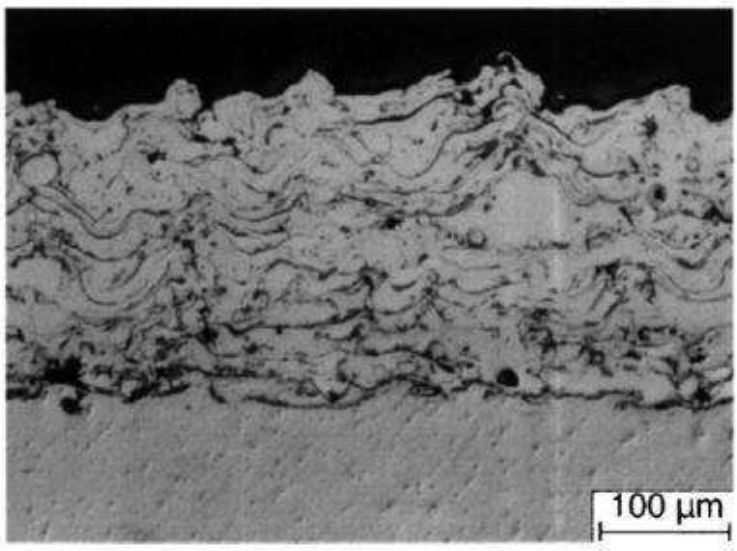


Figure 2.2 Lamellae structures deposited by SPS [2.6]

2.1.2. Thermal spray processes

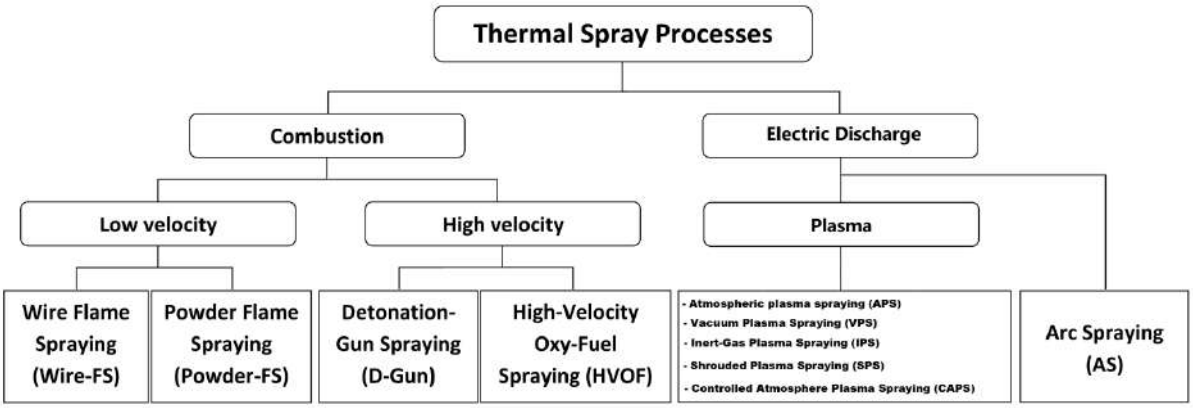


Figure 2.3 General thermal spraying processes

In general, thermal spray processes can be divided in two basic types: combustion (flame) spray processes and electric discharge spray processes [2.2] (**Figure 2.3**).

2.1.2.1. Low velocity combustion spray:

A heat of oxygen-fuel flame (oxy-acetylene, oxy-hydrogen or oxy-propane) is used [2.5] to melt the feedstock powder or wire. The acceleration of the particles in the direction of the substrate is obtained by the combustion gases or the dispersing gases such as the compressed air [2.2]. These spraying processes have relatively the lowest cost and they are used mainly for wear protection in various industries [2.2].

The principle of FS-Powder process is a gas and powders that are introduced into the torch. The particles become molten in the flame and are accelerated in the direction of the substrate [2.1]. The principle of FS-Wire process is a flame that melts the end of a wire which becomes atomized by a compressed air to form droplets that propelled towards the substrate [2.1].

2.1.2.2. High velocity combustion spray:

D-gun process gives a very dense coating with a high bound strength due to the high velocity of the particles upon impact, which results in a very good contact between the sprayed particles and a partial fusing of those particles and the substrate [2.2]. There are generally 1-15 detonations per second [2.1].

The major differences between HVOF process and the low velocity combustion spray processes is the confined combustion process under a higher pressure in the combustion chamber within the spray torch, and so the flame temperature and the combustion energy of the fuel gases are not as high as that of the low velocity processes. Compared with the D-gun, HVOF spray is a continuous process [2.2].

2.1.2.3. TWAS:

The principle of this process is two conductive wires that brought in contact with each other, then, a high voltage is applied on them to create an electric arc between the two wires. The temperature of the arc is up to 4000°C that melts the tips of the two wires and the molten particles are atomized and propelled to the substrate by a continuous flow of a compressed air or non oxidizing gas such as nitrogen. The wires are continuously fed the gun at uniform speed to balance the loss. TWAS process is easy to use and to maintain [2.5] (**Figure 2.4**). Generally, it can be considered as the most economical thermal spray process to be applied for corrosion resistant metal coatings [2.3]. In addition, it gives higher deposition rates and thereby thicker coatings [2.5].

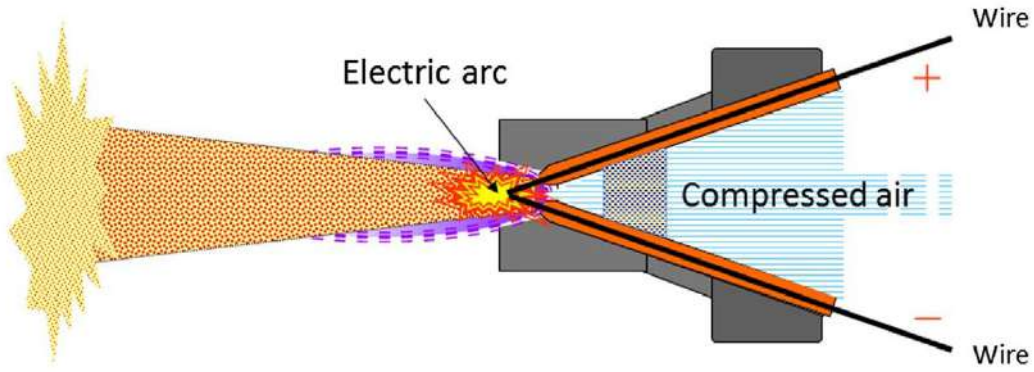


Figure 2.4 TWAS process principle [2.3]

2.1.2.4. Plasma spray:

The electric arc is the energy source for the plasma spray process. The gases are heated as they pass over and through the arc; they are expanded radially and axially, and accelerate through the nozzle exit. Then the exothermic recombination of atoms and molecules of the plasma gases follows. The feedstock material (mainly powder) is melted with a carrier gas and injected into the high energy plasma jet [2.2].

In APS process, powder particles interaction with the air atmosphere can cause a significant amount of oxides in the coating with a porosity range between 1-7% or more [2.1].

VPS process uses vacuumed chamber and the deposition process takes place after an evacuation up to $<10^{-1}$ mbar, then, the chamber is refilled with an inert gas atmosphere at pressure between 50-400 mbar [2.2]. The porosity of the coating is usually lower than 1-2% [2.1].

When the inert gas atmosphere pressure is higher (about 1 bar) the process is called IPS. Oxidation reactions of both substrate and coating materials are then suppressed [2.2].

SPS process has been developed to reduce the effort from the vacuum chamber and the pumping system for less expensive applications. An envelope of an inert gas, which is not ionized, protects the plasma jet from the surrounding oxygen containing atmosphere and also improves substrate cooling [2.2].

CAPS process combines VPS and IPS processes in one system. For a pressure range from 50 to 400 mbar VPS coatings are produced, and at pressures around 1 bar IPS coatings are obtained, and with pressures up to 4 bar high pressure, APS coatings are deposited [2.2].

2.1.3. Substrate preparation

Before coating the substrate, an important operation must be done, that is the surface preparation. Substrate surface preparation has generally three main steps [2.1]: surface cleaning, substrate shaping and surface activation.

2.1.3.1. Surface cleaning:

To clean the surface from grease or any undesirable contaminations such as oxides and corrosion products, dust particles and physical adsorption of atmosphere; organic solvents (methyl alcohol and acetone), hot water under high pressure or water vapor are generally used [2.1].

2.1.3.2. Substrate shaping:

Substrate shaping is used to obtain the desired form of the samples and to avoid any dimension that can reduce the coating properties like sharp ends or sharp angles where the coating adherence will be too poor due to the high concentration of the thermal stresses and so it will be difficult to be coated [2.1].

2.1.3.3. Surface activation:

Activation is a temporary increase of the chemical reactivity of the surface. The activated surface should be used within a specified time after the activation [2.7]. The surface activation phase is important to enhance the coatings adherence. According to the physicochemical phenomena, there are two types of the coatings adherence [2.8]:

- Intrinsic adherence: it appears during the coating formation and it depends on the surface roughness, crystallographic structure similitude between the coating and the substrate material and the difference in TECs between the substrate and the coating.

- Service adherence: it appears during the coating service and it depends on the thermal and the mechanical solicitations and also on the difference between the mechanical properties between the substrate and the coating.

Grit blasting is the method that is largely used to activate the surfaces. The principle of the grit blasting is to send hard grits with a high velocity into the substrate surface by compressed air to get a rough surface. **Table 2.1** shows the grit blasting main parameters.

In spite of being largely used because of its simplicity, grit blasting has an important disadvantage and that is the contamination of the activated surface by grits. These embedded grits will cause “pinhole flaking” in the deposited coating [2.7]. In order to avoid such drawback, substrate surfaces can be activated by water jet, laser ablation or by chemical attack.

Process element	Parameter
Grit	Material/ Grit size/ Elastic modulus/ Hardness
Blasted surface	Elastic modulus/ Hardness/ Thickness
Grit-feed principle	Suction/ Gravitational effect
Blasting atmosphere	Cabinet blasting/ Open air blasting
Blasting technique	Duration/ Compressed air pressure/ Angle of grit impact/ Distance between nozzle and substrate

Table 2.1 Grit blasting principal parameters [2.1]

2.1.4. Post-spray Heat treatment

Post-spray heat treatment can be considered as a key step to enhance the quality of the coating [2.1]. In industrial point of view, furnace and flame heat treatments are the most economical processes.

In furnace treatment, the heat treatment is realized at different gas atmospheres. The main inconvenient for that process is the creation of the thermal stresses during the heating cycle if the substrate and the coating have different TECs. If such stresses are higher than the fracture and/or the ultimate stress of the coating, a permanent deformation will occurs i.e. the coating damages. Consequently, the maximum temperatures for furnace treatments are limited [2.1].

2.1.5. Thermal sprayed coatings formation

Thermal sprayed coatings are the result of the accumulation of the injected particles that strike the substrate. These particles can be fully melted or partially melted. Partially melted particles result in a heterogenic coating. The heterogeneity of the coating occurs also because of the

different sizes of the sprayed particles. Variation in the particles velocity and temperature has also an effect on the heterogeneity of the obtained coating. Unmelted particles are weakly connected to the rest of the coating and thereby reduce its behaviour.

At the moment of the impact on the substrate or the previously deposited coating, molten particles are transformed into lamellas. Such transformation is associated with the processes of deformation and solidification. Coating microstructure and characteristics depend on the deformation of the particles, that deformation is independent from the spray process but it depends on the particles velocity at the impact and their phase content.

Temperature of the interface between particles/substrate at the impact is called the contact temperature and it influences the adherence of the coating.

The impact of the particles can happen during two stages [2.1]:

- Subcritical flow regime stage: started by the contact with the substrate and finished by the formation of a truncated sphere with a compressed liquid near the contact circle (**Figure 2.5**).

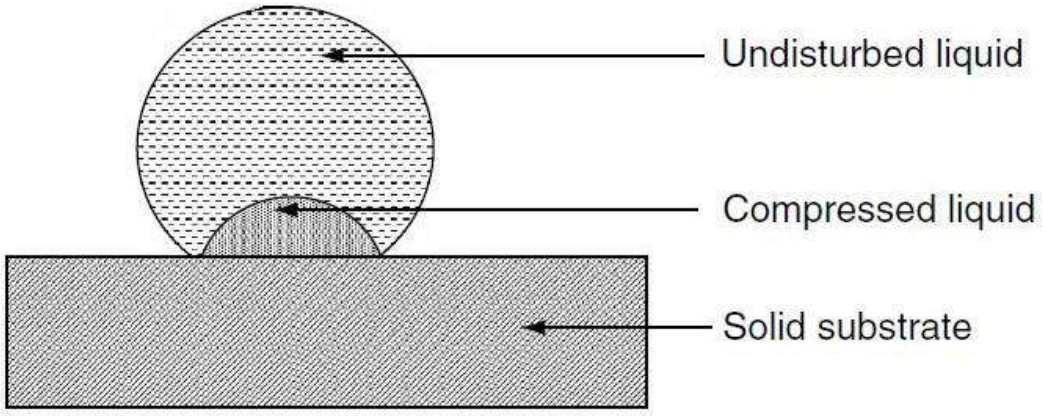


Figure 2.5 Subcritical flow regime in the impact of a liquid particle [2.1]

- Postcritical flow regime stage: the liquid starts to expand radialy to reach its final shape (splat) and simultaneously the solidification occurs. The liquid expansion size is limited by the substrate roughness. This effect can be explained by the action of the friction force between the liquid and the substrate roughness which restrain the movement of the liquid.

Lamellas and splats can have two principal morphologies: the pancake and the flower morphologies [2.1] (**Figure 2.6**).

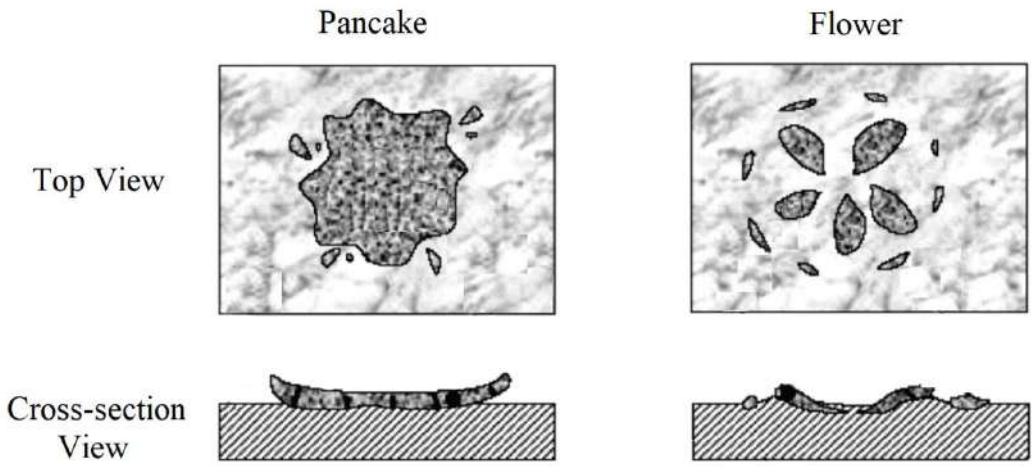


Figure 2.6 Lamella and principal morphologies [2.1]

Generally, pancake morphology which is formed without the particle splashing, is obtained during the impact of fine particles or particles with low thermal and/or kinetic energies or with substrate at high temperature. Inversely, flower lamella which is associated with splashing is formed with high energy impact or with the substrate at low temperature. For each coating/substrate pair, there is a substrate temperature bellow it flower splat is formed and above it pancake splat is formed.

Solidification starts after the contact of the liquid particles with the substrate or the previous deposited layers and finishes either after the splat deformation or sometimes faster, or in very particular cases, the deformation and the solidification happens simultaneously.

During thermal spray, substrate is heated by the thermal flux of the torch and of the sprayed particles. Thermal flux types are depending on the spray process (**Table 2.2**).

Thermal flux	Flux description	Spraying process
Radiative	Radiation of plasma jets in all directions	Plasma processes (APS, VPS, IPS, SPS, CAPS)
Convective	Convective flux coming from the jets and flames, directed towards the substrate	Plasma processes (APS, VPS, IPS, SPS, CAPS), Combustion processes (Wire-FS, Powder-FS, D-Gun, HVOF).
Splats solidification	Liberated latent heat of fusion, directed towards the cooler zones of the coating and/or substrate	All spraying processes
Lamellae cooling	Flux resulting from the lamellae cooling down to the temperature of equilibrium, directed towards the cooler zones of the coatings and/or substrates	All spraying processes

Table 2.2 Thermal flux types for different spraying processes [2.7]

Heat is released through the substrate in the direction of the bottom part of the lamella, but the thermal contact resistance between the bottom part and the substrate can restrain the heat evacuation and slowing down the solidification of the lamella.

The solidification front morphology can be planar, cellular or dendritic depending on the cooling rate (**Figure 2.7**).

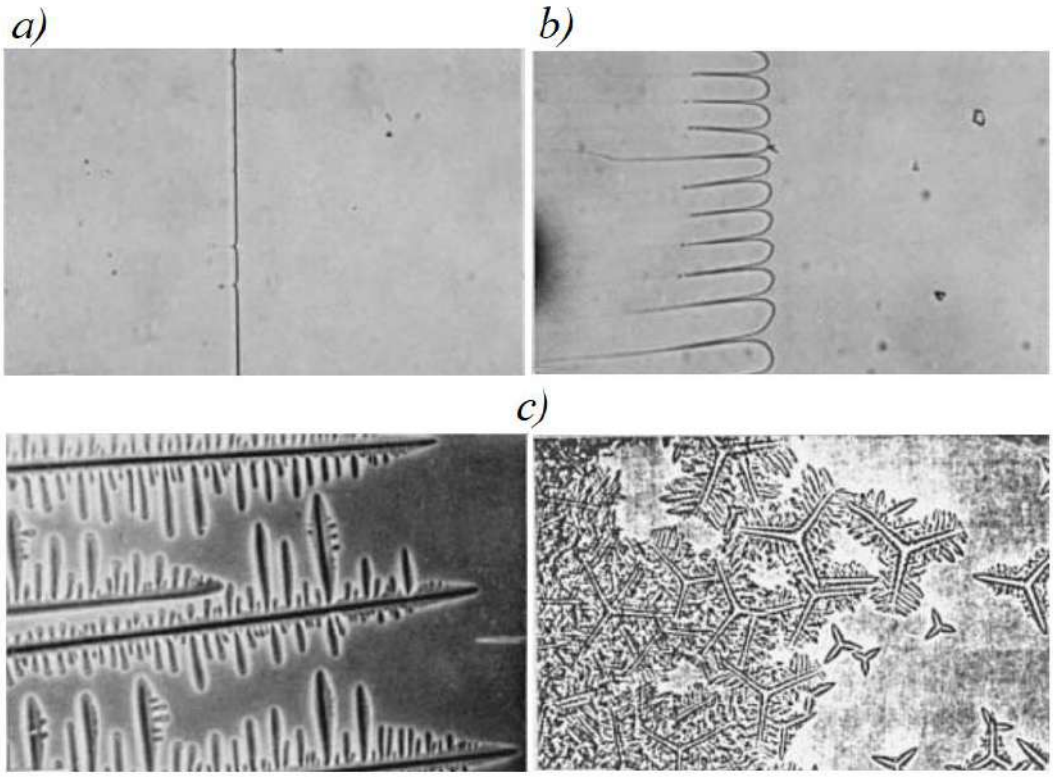


Figure 2.7 (a) planar, (b) cellular, (c) dendritic solidification front morphologies [2.9]

At a very high cooling rate, no nuclei can be formed but only amorphous grain microstructure. At a very high cooling rate also, some crystals grow in their preferential direction and as a result a texture microstructure can be formed. A good substrate roughness can reduce such formation.

Generally, the adhesion mechanism of the sprayed coating is a mechanical anchorage. During the solidification, splats are not in a whole contact with the substrate area, only some contact zones are obtained called active zones. With increasing the active zones, coating adherence increased. However, oxides contamination and porosity reduce those active zones. The adhesion mechanisms of the active zones can be one of the following:

- Physical interaction: between the atoms of the lamella and of the substrate as results of Van Der Waals forces and it can occurs only if the contact lamella/substrate is close i.e. in the field of attraction of atoms (less than 1 nm).

- Metallurgical interaction: which can be diffused due to the rapid solidified lamellas and/or the high contact temperature, or it can be chemical reaction between the lamella and the substrate materials resulting in the formation of intermetallic phases and a strong metallurgical bonding.

Residual stresses are composed of mechanical stresses that are introduced during the grit-blasting of the substrate (compressive stresses) and the stresses that are introduced during the deposition which can be one of the following four types:

- Quenching stresses: generated when the sprayed particles solidify rapidly. At a low deposition temperature, such stresses are predominant.

- Stresses generated in one pass of the torch, if the deposited layer is thick enough. In this case the temperature gradient between the surface and the interface of the layer becomes large, generating those stresses.

- Cooling stresses: generated during the cooling down, when the thermal expansion coefficients of the coating and the substrate are different. At high deposition temperatures those stresses are predominant. In order to reduce the possibility of getting such stresses, intermediate coatings and/or post-spray treatment are applied.

- Phase transformation stresses: generated when the temperature during post-spray heat treatment is bigger than the phase transformation one.

At the end of the spray process, too many defects can be obtained on the coating due to badly optimized processing parameters. Some of them are presented in **Figure 2.8**.

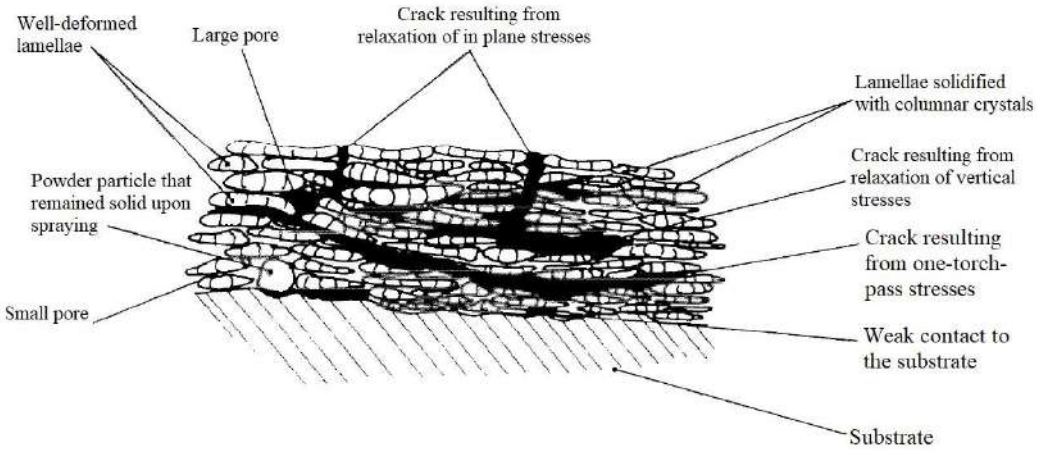


Figure 2.8 General defects obtained on the thermal sprayed coatings [2.1]

2.2. Basics of vacuum and plasma

2.2.1. Vacuum and gas state of materials

Characteristics	Vacuum			
	Low vacuum	**Medium vacuum**	**High vacuum**	**Ultrahigh vacuum**
Pressure (bar)	$1 - 10^{-3}$	$10^{-3} - 5 \cdot 10^{-5}$	$5 \cdot 10^{-5} - 10^{-12}$	$< 10^{-12}$
Number of molecules in 1 cm^3	$10^{19} - 10^{16}$	$10^{16} - 10^{13}$	$10^{13} - 10^{10}$	10^{10}
Mean free path λ	$\lambda \ll l$	$\lambda < l$	$\lambda > l$	$\lambda \gg l$
Flow regimes	Viscous flow	Intermediate flow	Molecular Flow	Molecular Flow

Table 2.3 General characteristics of vacuum types [2.10]

Materials in gas state are characterized by the great mobility of their molecules. Because of that, they always occupy the volume of the container in which they are enclosed. In physics

and technology, we call vacuum, the state in which the gas pressure is below the atmospheric pressure. In general, vacuum can be divided in four types: low vacuum, fine or medium vacuum, high vacuum and ultrahigh vacuum. **Table 2.3** gives the general characteristics of these types:

According to the kinetic theory, the gas molecules move in a continuous and chaotic manner. They collide with each others, and during their impacts their motion is straight. The distance between two successive impacts is called the mean free path of the gas molecule λ. After each impact, the velocities magnitude and direction of the molecules change.

When the gas occupies a limited volume, there will be molecular impacts on the walls of the container, and the gas pressure is the result of the statistical average of these impacts.

A general criterion characterizing the vacuum in a system is the ratio between λ of the molecule with a characteristic dimension *l* of the vacuum chamber, that is to say:

$$Kn = \frac{\lambda}{l} \quad (2.1)$$

The Kn ratio is known as Knusden number, when Kn >> 1 i.e. λ >> *l*, the flow regime of the gas is the molecular flow. When Kn << 1 i.e. λ << *l*, the flow regime is the viscous flow.

The limit temperature above which, the gas cannot be condensed, whatever the pressure is, called the critical temperature. This is a fundamental criterion for distinguishing gases from vapors. Materials are in a gas state when their temperature is above their critical temperature. If the temperature is below their critical temperature, they are in a vapor state.

The pressure can be written in the form of the following equations:

$$P = n \cdot k' \cdot T \quad (2.2)$$

n : The density of the molecules (m^{-3});

k' : The Boltzmann constant ($1.38 \cdot 10^{-6}$ N·m/K);

T : The gas temperature.

$$P = \frac{1}{3}\rho\bar{v}^2 \quad (2.3)$$

ρ : The density of the gas (Kg·cm^{-3});

$\sqrt{\bar{v}^2}$: The root mean square velocity of molecules.

When the system is a mixture of different gases, each gas exerts its own pressure P_i independently from the others. The total pressure P_Σ is the sum of the partial pressures (Dalton's law):

$$P_\Sigma = \sum_{i=1}^{i=n} P_i \quad (2.4)$$

According to the kinetic theory, the mean kinetic energy of the molecules motion is proportional to the temperature of the gas:

$$\frac{m \cdot \bar{v}^2}{2} = \frac{3}{2} \cdot k \cdot T \quad (2.5)$$

m: molecule mass *(kg)*.

2.2.2. Motion and velocity of gas molecules

The gas molecules have different velocities. During their thermal motions, they collide with each others. As a result, the magnitude and the direction of their velocities change. The distribution of molecules according to their velocity is described by a statistical law. It is generally assumed that this distribution follows the Maxwell's law.

According to Maxwell, molecules have absolute velocities between *v* and *v* + *dv* for any direction of motion. The distribution of their velocities is given by the equation:

$$\mathrm{f(v) \cdot dv} = 4\pi\mathrm{N} \cdot \left(\frac{\mathrm{m}}{2\pi\mathrm{kT}}\right)^{3/2} \mathrm{e}^{-\frac{\mathrm{mv^2}}{2\mathrm{kt}}} \mathrm{v^2 dv} \quad (2.6)$$

This function allows determining the most probable velocity v_p. The most probable velocity v_p corresponds to the maximum of the function *f (v)* that can be determined by the condition:

$$\frac{\mathrm{d}}{\mathrm{dv}}\left(\mathrm{e}^{-\frac{\mathrm{mv}^2}{2\mathrm{kT}}}\mathrm{v}^2\right) = 0 \quad (2.7)$$

Result of (2.7) gives the v_p:

$$v_p = \sqrt{\frac{2kT}{m}} \quad (2.8)$$

In calculations, the arithmetic mean velocity $\bar{v}$ is generally used:

$$\bar{v} = \sqrt{\frac{8kT}{\pi m}} = 1.128\, v_p \quad (2.9)$$

The roots mean squared velocity $\sqrt{\bar{v}^2}$ can be also used:

$$\sqrt{\bar{v}^2} = \sqrt{\frac{3kT}{m}} = 1.223\, v_p = 1.08\, \bar{v} \quad (2.10)$$

Figure 2.9 shows the molecule velocities distribution at two different temperatures.

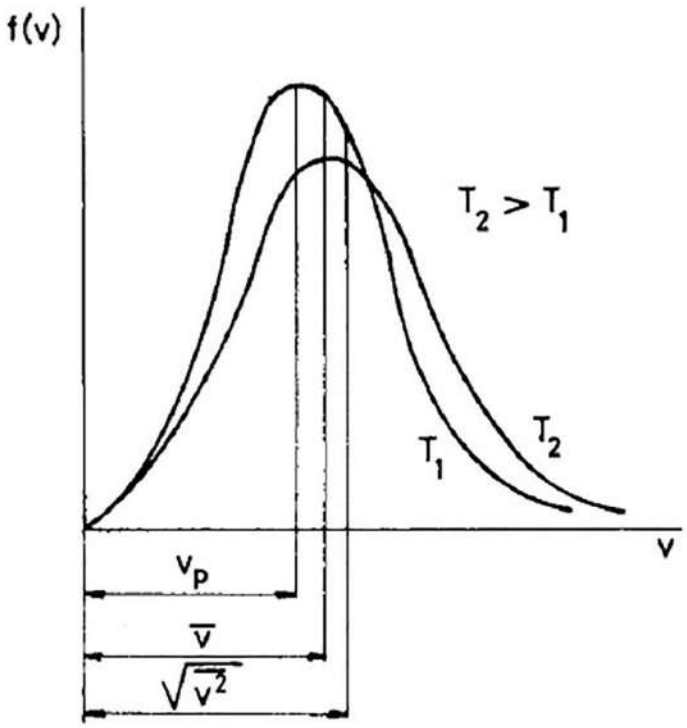


Figure 2.9 Gas velocities distributions at two different temperatures [2.11]

Kinetics theory shows that each constituent of a gas mixture has an independent velocity distribution.

At great distances, molecules attract themselves, while at smaller distances they repel each others. The number of the intermolecular impacts *B* can be calculated by the following formula:

$$B = \sqrt{2} n \pi a^2 \bar{v} = \sqrt{2} P a^2 \sqrt{\frac{8\pi}{mkT}} \quad (2.11)$$

a : Molecule diameter (considering the molecule as a solid sphere).

Finally the mean free path λ is calculated by:

$$\lambda = \frac{1}{\sqrt{2}\pi a^2 n} = \frac{kT}{\sqrt{2} P \pi a^2} \quad (2.12)$$

This gives:

$$\lambda = \frac{\bar{v}}{B} \quad (2.13)$$

The variation of the free mean path of some molecules as a function of the pressure is shown in **Figure 2.10**.

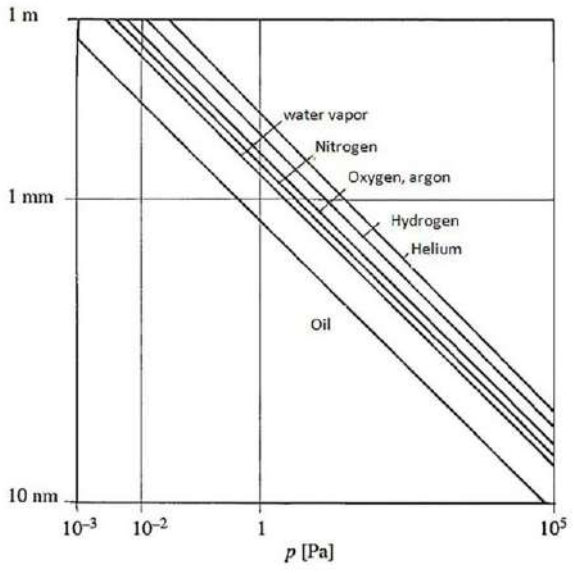


Figure 2.10 Free mean path of gas molecules as a function of the pressure [2.11]

2.2.3. Basics of vacuum technology

Each vacuum setup contains a chamber where the vacuum is obtained and maintained, a vacuum pump that evacuates the chamber and pipes which connect the chamber with the pump. When the pump is switched on, molecules in the chamber are pumped to the outside (**Figure 2.11**).

While pumping, the quantity of gas contained in the vacuum setup decreases, and so its pressure falls because the volume and temperature of the installation remain constants. In fact, the expansion of the gas lowers the temperature, but because of the high thermal inertia of the setup, gas temperature is considered constant.

The variation in mass flow rat Q as a function of the quantity of gas molecules passing through the section per unit time N is given by:

$$Q = k \cdot N \cdot T \quad (2.14)$$

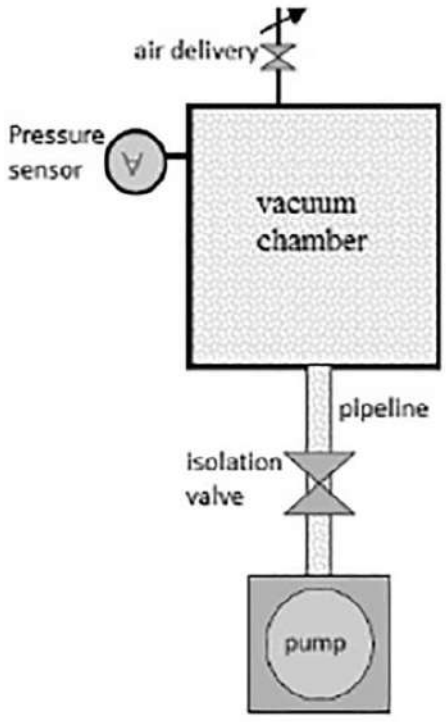


Figure 2.11 Principle of a vacuum setup

2.2.4. Pumping duration

The pumping of a vacuum system is a non-stationary process. During pumping, the pressure and the flow rate of each point of the setup will vary. The pumping duration is the time it takes to obtain a certain pressure in the vacuum setup.

For a piping with high conductance, the pumping time can be obtained by:

$$t = \frac{V}{Q} Ln\left(\frac{P_0}{P}\right) \quad (2.15)$$

V : The chamber volume (m^3);

P_0 : The pressure of the gas in the initial instant (N/m^2);

P : The pressure of the evacuated gas (N/m^2).

In general, the pumping duration can be obtained also using the nomograms shown in **Figure 2.12**. To use them, first calculate V and Q, and then join the corresponding points by straight line. The obtained point on the line V/S is joined to the corresponded point on the line of P which corresponds to the pressure to be obtained. The obtained intersection point on the line of t gives the necessary pumping duration.

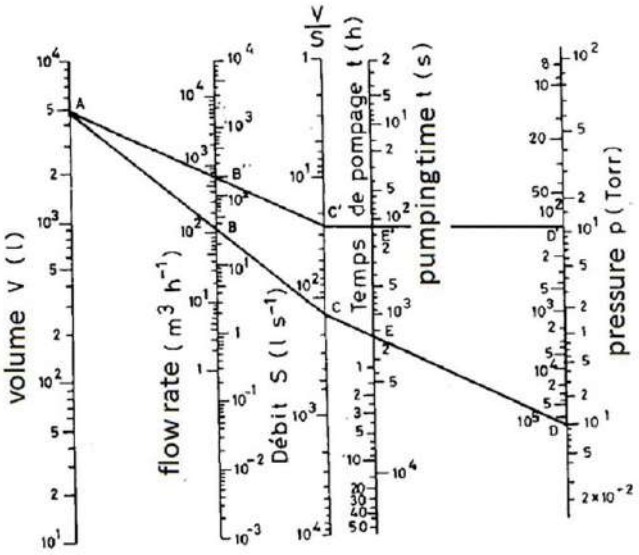


Figure 2.12 Nomogram for calculating the pumping time [2.11]

2.2.5. Theory of plasma

In their normal state, gases are electricity insulators; this is due to the fact that they don't contain free charged particles. However, by charging them with high electric fields, they become conductors. The phenomena that occur called discharging in gases and it is due to the appearance of electrons and free ions. The result from discharging is the formation of ionized gas. The degree of the gas ionization is defined by the ratio α′:

$$\alpha' = \frac{n}{n_0 + n} \quad (2.16)$$

n_0 : The quantity of neutral particles per unit of volume;

n : The quantity of ionized particles per unit of volume.

The degree of ionization value varies from very low values in the order of 10^{-10} to one. A degree of ionization is equal to one means that the gas is totally ionized.

The study of concepts, methods and results of this state of matter constitutes the physics of plasmas. In our environment, the plasma phase is totally absent in its natural state, whereas in the cosmic scale, more than 99.9% of the visible matter is in this phase.

When heating a gas with a sufficient high temperature (the order of 10^4 K), the average energy of its molecules motion can become of the same order as their ionization energy. Under these conditions, if two molecules collide, one of them can be ionized.

The probability of the ionization as a function of the energy is characterized by a threshold which is the ionization energy. The ionization energies for all species can be found in specialized data banks.

Among all the weakly ionized gases we distinguish three families:

- Lowly ionized gases: in which some ions and electrons move in the middle of neutral molecules. Ions and electrons interact only with theses neutral molecules;

- Highly ionized gases without interactions between particles: in this plasma the charged particles move without any collision. Their trajectory is determined by external electromagnetic fields;

- Highly ionized gases with interactions between particles.

There are two main types of plasmas that are: hot plasma and cold plasma. The plasma is called hot when the temperature of the ions and electrons are high (more than 10^7 K). In this case, the medium will be completely ionized. The plasma is called cold when the electrons are hot (in the order of 10^4 K), and the ions are cold (from 300 to 10^4 K). The medium in this case is weakly ionized (ionization rate is close to 10^{-6} and up to 10^{-2} per neutral species).

Coating by plasma involves the modification of the state of the surface by one of the following methods:

- The deposition of a thin film;

- Chemical reaction with the surface itself (oxidation, nitriding) or physicochemical transformation of the surface (modification of adhesion, surface energy);

- Surface erosion either by chemical action (formation of pores between one or more atoms of the surface) or by ion sputtering due to plasma ion bombardment of the surface atoms or chemically-assisted sputtering that combines the ion bombardment and the chemical erosion [2.12, 2.13].

2.3. PVD

PVD processes are atomistic deposition processes in which material is vaporized from a solid or liquid source in the form of atoms or molecules by evaporation, sputtering, laser ablation, etc., transported from the source to the substrate and during the transport, some of the vapor species can be ionized by creating plasma in the space between the source and the substrate.

Then, the vaporized species are condensing on the substrate surface, followed by the formation of the thin film by nucleation and growth processes [2.2, 2.7].

PVD processes are used to deposit thin films. Generally, the term “thin film” is applied to layers which have thicknesses in the order of several microns or less. Thicker layers such as the thermal sprayed ones are often called coatings [2.7].

The main PVD processes are vacuum evaporation and sputtering.

2.3.1. Vacuum evaporation

It is a PVD process in which material from a thermal vaporization source reaches the substrate with little or no collision with gas molecules in the space between the source and substrate. The vacuum environment provides the ability to reduce gaseous contamination in the deposition system to a low level. Evaporation is generally done using thermally heated sources such as tungsten wire coils or by high energy electron beam. Generally, the substrates are mounted at an appreciable distance away from the evaporation source to reduce radiant heating of the substrate by the vaporization source [2.7]. A schematic of an evaporation system is shown in **Fig.2.13**.

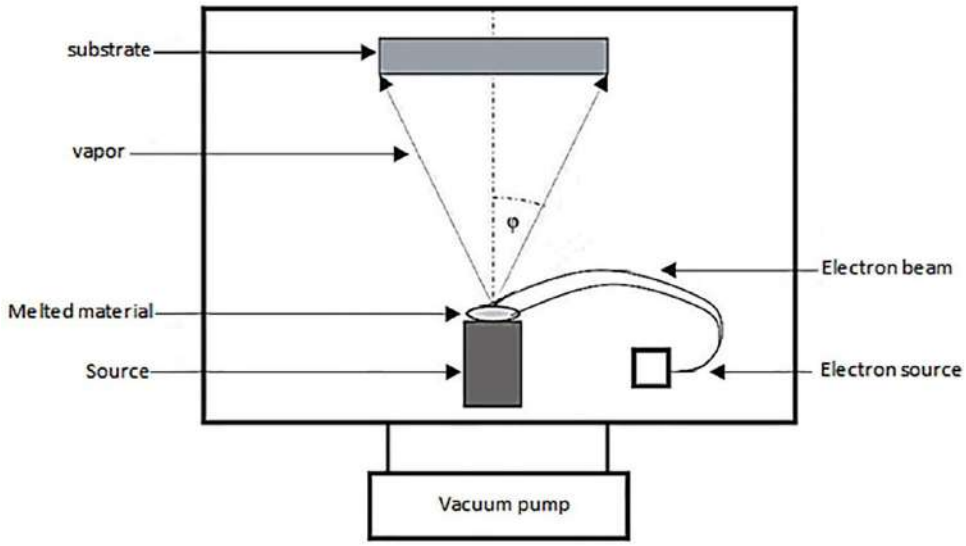


Figure 2.13 PVD vacuum evaporation system [2.8]

The advantages of that process are:

- High deposition rates (more than 200 μm/h);

- Low processing temperature allowing deposits on plastic substrates.

The disadvantage of this process is the weak adherence between the thin film and the substrate, because the film is made in a vapor phase with a low energy. It is often necessary to heat the substrate towards 300 to 400 °C, or to use subsequent heat treatments to improve the adhesion [2.8].

2.3.2. Sputtering

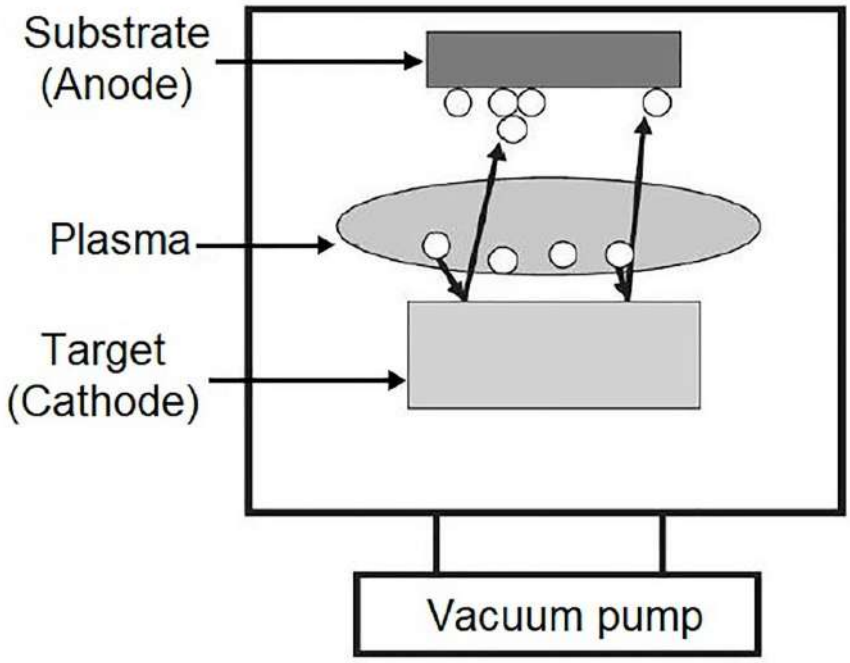


Figure 2.14 PVD sputtering system [2.8]

Sputtering is the phenomena of a momentum transfer from an incident energetic projectile which is usually a gaseous ion that is accelerated from plasma to a solid or a liquid target resulting in the ejection of surface atoms or molecules [2.2]. The sputtering deposition consists of placing the target known as the cathode (a source of coating material) face to face

with the substrate known as the anode in the vacuum chamber (**Figure 2.14**). The target is connected to the negative voltage. A glow discharge is initiated after an inert gas (usually argon) is introduced into the evacuated chamber [2.2]. The sputtering rate increases with the applied voltage due to the increase in the discharge current.

- Magnetron sputter deposition

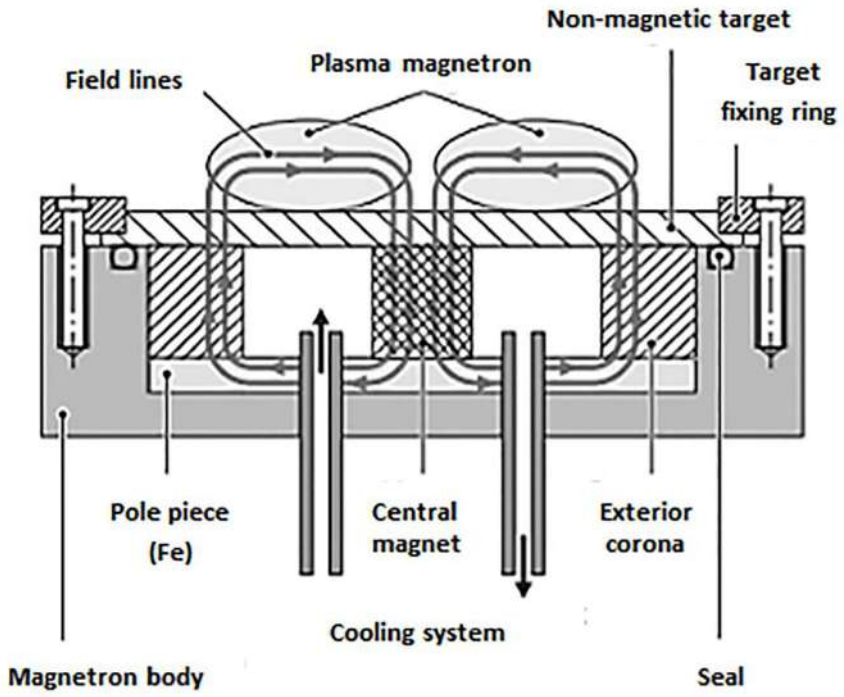


Figure 2.15 Principle of the magnetron work in PVD sputter process [2.14]

In the conventional PVD sputtering process, the primary electrons are generated far from the target and the probability for ions to lose their energy to the chamber walls is high and so, the ionization efficiency is low [2.2] and the deposition speed is low (<0.1 μm/h) [2.14]. However, in magnetron sputtering deposition process, the magnetron field form traps for the primary electrons and control their motions. Dense plasma is then generated (**Figure 2.15**), which leads, despite the heterogeneous erosion of the target, to increase considerably the deposition speed in the order of 10 μm/h [2.14].

The magnetron sputtering PVD process has the advantages of high sputtering rate. The disadvantages from this process are the limitation of choice of the target materials (must be non-magnetic targets) [2.2].

2.3.3. Thin films formation

The formation of the PVD's thin films is resulted from the condensation of the particles ejected from the target onto the substrate, and it is carried out after the combination of the nucleation and their growth.

At the moment of their impact on the substrate, the incident atoms lose their kinetic energy which limits their ability to diffuse through the substrate. However, using some techniques such as the substrate heating or ion bombardment, the ability of atoms diffusion will increase. The incident atoms are known by the adatoms.

During their diffusion, the adatoms interact with each other creating nucleus called the clusters. Those clusters continue to grow, leaving only holes or channels of small dimensions between them. A continuous film can be formed when those holes and channels are totally filled [2.14].

There are three modes of clusters nucleation and growth:

- Volmer-Weber mode (**Figure 2.16(a)):** This mode of growth is usually obtained when the binding energy between adatoms forming the thin film is higher than that between the thin film and the substrate. As the film growth proceeds, these clusters expand, widening their volumes of heights higher than the thickness of a monolayer thin film, and as a consequence, thin films with rough surface will be obtained.

- Frank-Van DerMerwe mode (**Figure 2.16(b)):** This mode of growth is obtained when the binding energy between the adatoms is less than or equal to that between the thin layer and

the substrate. As consequence, a complete monolayer thin film will be formed before another starts to grow.

- Stranski-Krastanov mode (**Figure 2.16(c)):** This mode is a combination of the two preceding modes is taking place: starting by Frank-Van DerMerwe mode. When a critical layer thickness is reached, where its value depends on the specific physical properties of the deposited material, the elastic energy accumulated during the growth relaxes, resulting in the formation of the clusters with the Volmer-Weber mode [2.15].

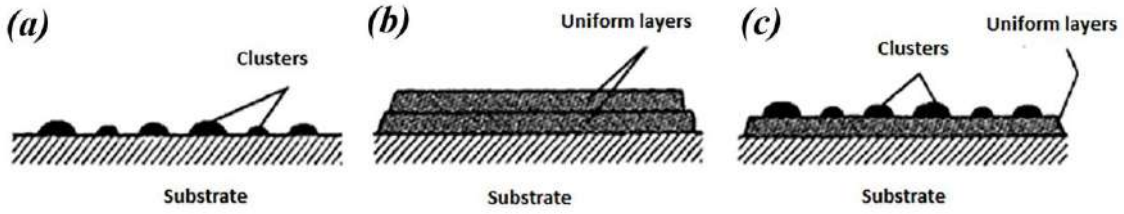


Figure 2.16 The three modes of thin films formation [2.15]

2.3.4. Thin films morphology

The clusters growth mode accompanied with the deposition conditions have an influence on the crystallographic orientations and the topology of the obtained thin film.

There are several models of the thin films growths depending on the deposition conditions:

- Movchan and Demchishin model (1969) [2.16]**:** according to this model, there is three zones of the thin films morphologies (**Figure 2.17**):

First zone: this zone is suitable to obtain lubricating film, but not suitable to improve the corrosion resistance and the mechanical strength.

Second zone: or the transition zone where the microstructure of the film is very fine with good properties in terms of corrosion resistance and adhesion.

Third zone: where the columnar structure of the film is well identified, this zone is preferred for mechanical applications because of the excellent obtained adhesion.

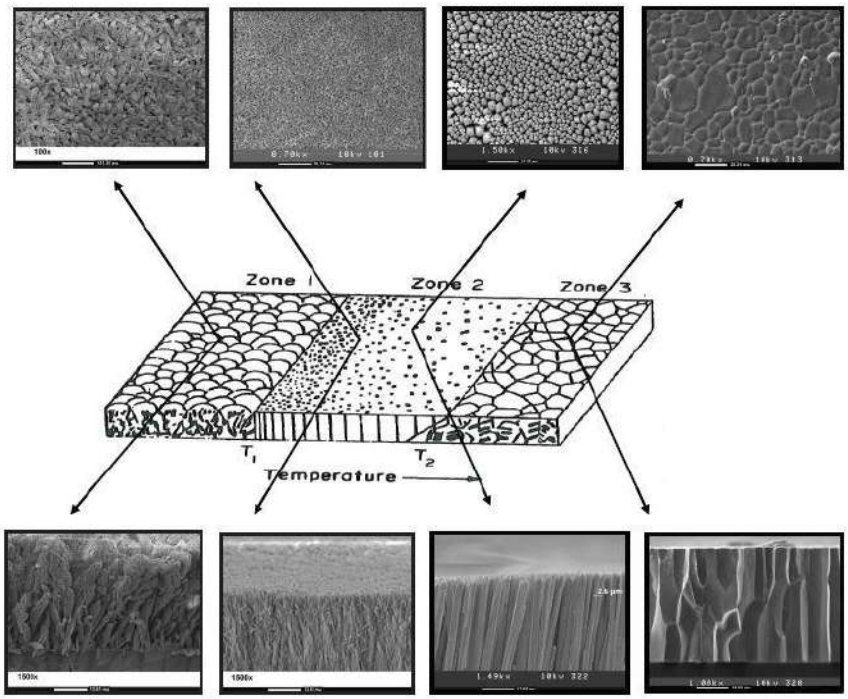


Figure 2.17 Movchan and Demchishin model [2.17]

- **Thornton model (1977)** [2.18]**:** Thornton proposes a model that complements the previous one by considering the argon gas pressure during the sputtering process. The model shows a transition zone, called zone T, between zones 1 and 2 (**Figure 2.18**). In this zone, the grains have a fibrous form without porosities.

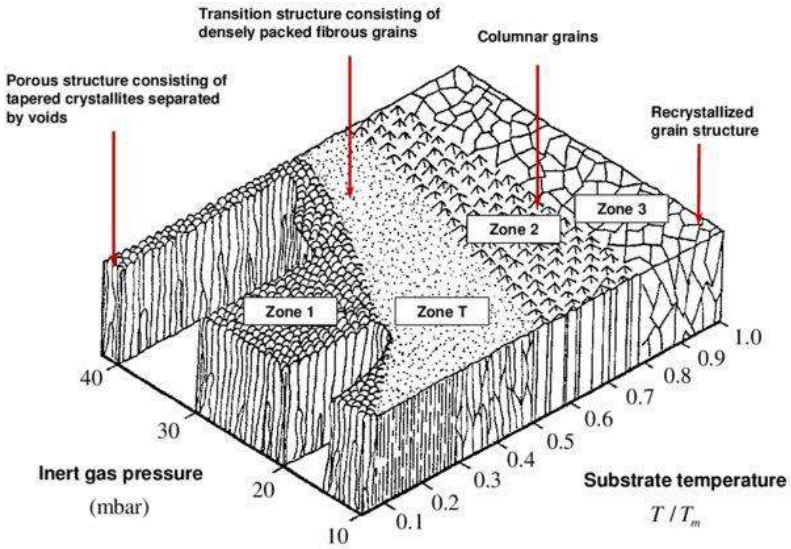


Figure 2.18 Thornton model [2.19]

- Messier et al. model (1984) [2.20]**:** Messier et al. showed that the fundamental process controlling the morphology of the T-zone is not only the argon gas pressure but also ion bombardment energy on the growing films during their deposition. . According to this model, high ion energy has a positive effect on the growth of the preferable transition zone T in low-temperature deposition processes (**Figure 2.19**).

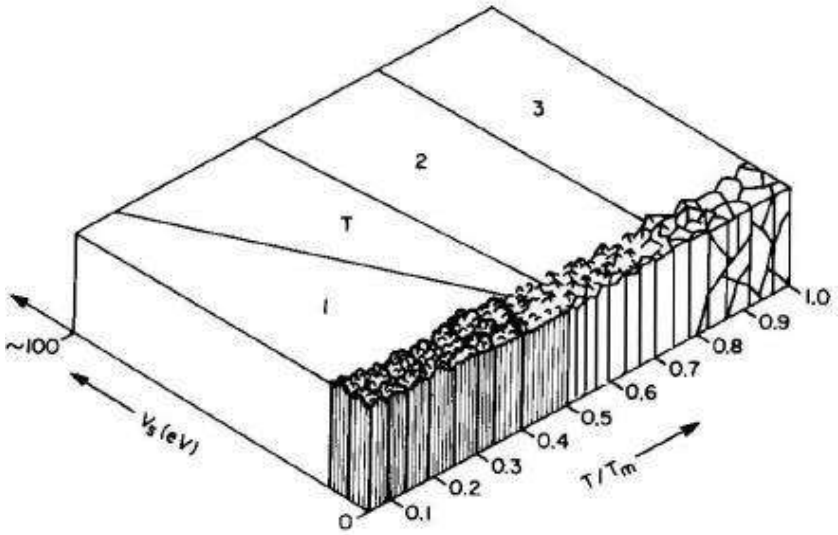


Figure 2.19 Messier model [2.20]

References

[2.1] L. Pawlowsky, *The science and engineering of thermal spray coatings*, John Wiley & Sons, England, 2008.

[2.2] R.F. Bunshah, *Handbook of hard coatings*, Noyes publications Park Ridge, New Jersey, 2001.

[2.3] P. Vuoristo, Thermal spray coating processes, *Compr. Mater. Process.*, 2014, **4**, p 229-276.

[2.4] X. Meng, J. Zhang, W. Han, and J. Zhao, Fracture behavior of cold sprayed 304L stainless steel coating during cold rolling, *J. Iron Steel Res. International*, 2012, **19**, p 57-63.

[2.5] M.R. Dorfman, *Handbook of Environmental Degradation of Materials*, William Andrews Publishing, NY, 2018.

[2.6] L. Zhao, and E. Lugscheider, Influence of the spraying processes on the properties of 316L stainless steel coatings, *Surf. Coat. Technol.*, 2002, **162**, p 6-10.

[2.7] D.M. Mattox, *Handbook of physical vapor deposition (PVD) processing: Film Formation, Adhesion, Surface preparation and Contamination Control*, Noyes publications Westwood, New Jersey, 1998.

[2.8] L. Pawlowski, *Dépôts physiques: techniques, microstructures et propriétés (Physical deposition ; techniques, microstructures and properties)*, Presses polytechniques et universitaires romandes, Switzerland, 2003. (In Franch)

[2.9] A. Chiocca, "*Etude de l'influence des écoulements dans le bain de fusion sur les mécanismes de solidification en cours de soudage sur l'alliage $Cu_{30}Ni$" (Study of the influence of flows in the weld pool on the solidification mechanisms during welding on the $Cu_{30}Ni$ alloy)*, Ph.D Thesis, Montpellier University, 2016. (In Franch)

[2.10] E. Bergmann, H.J. Mathieu, and R. Gras, *Traité des matériaux Tome 4: Analyse des surfaces (Treatise on materials Volume 4: Surface analysis)*, Presses polytechniques et universitaires romandes, Switzerland, 2003. (In Franch)

[2.11] G. Grigorov, *Vide poussé au laboratoire et dans l'industrie (High vacuum in laboratory and in industry)*, Edition Masson et Cie, France, 1970. (in Franch)

[2.12] M. Moisan, and J. Pelletier, P*hysique des plasmas collisionnels (Collisional plasma physics)*, EDP science, France, 2006. (In French)

[2.13] J.L. Delcroix, and A. Bers, *Physique des plasmas tome 1 (Plasma physics volume 1)*, EDP science, France, 1994. (In French)

[2.14] R. Develay, *Traitement de surface des métaux par voix sèche et en milieu fondu (Surface treatment of metals by dry process and in a molten medium)*, Techniques d'ingénieur, Ref: 42360210, 1992. (In French)

[2.15] C.I. Fornari, G. Fornari, P.H.O. Rappl, E. Abramof, and J.D.S. Travelho, Monte Carlo simulation of epitaxial growth, *Epitaxy*, 2018.

[2.16] B.A. Movchan, and A.V. Demchishin, Study of the structure and properties of thick vacuum condensates of nickel, titanium, tungsten, aluminum oxide and zirconium dioxide, *Fiz. Metal. Metallovcd*, 1969, **28**, p 653-660.

[2.17] H. Sabet, H.B. Bhandari, H. Kudrolli, V.V. Nagarkar, Fabrication of X-ray/gamma-ray detector by growth of microcolumnar CsI:Tl onto silicon photomultipliers, *Phys. Procedia*, 2012, **37**, p 1523-1530.

[2.18] J.A. Thornton, High rate thick film growth, *Annual Rev. Mater. Sci.*, 1977, **7**, p 239-260.

[2.19] J.J. Fernandez, *"Tuning the thermal conductivity of polycrystalline films via multiscale structural defects and strain"*, Ph.D Thesis, Central school of Paris, 2015

[2.20] R. Messier, A.P. Giri, and R.A. Roy, Revised structure zone model for thin film physical structure, *J. Vac. Sci. Technol. A*, 1984, **2**, p 500-503.

Chapter 3

Experimental material and methods

3.1. The substrate

The substrates are of EN 10025-2 carbon steel with a diameter of 10 mm and a thickness of 10 mm (**Figure 3.1**).



Figure 3.1 substrates size

The chemical composition of the substrate is given in **Table 3.1** and their XRD patterns are given in **Figure 3.2**.

Fe %	C %	Mn %	P %	S %	N %	Cu %
97.496	0.21	1.60	0.040	0.040	0.014	0.60

Table 3.1 EN 10025-2 carbon steel chemical composition [3.1]

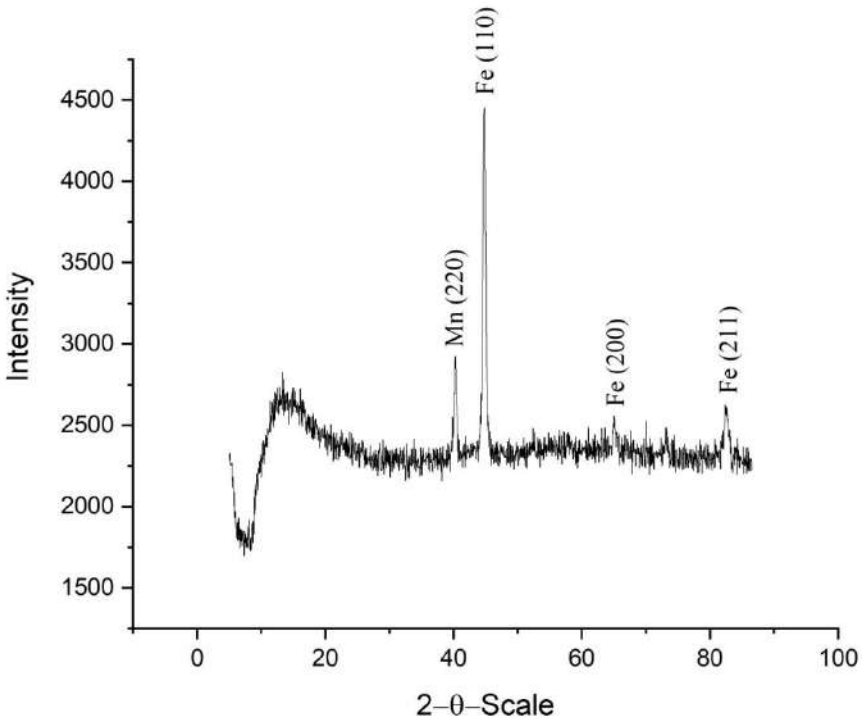


Figure 3.2 XRD patterns for EN 10025-2 Structural Steel

3.2. Grit blasting conditions

The grit blasting of the substrates before the coating deposition was carried out according to further optimizations [3.2, 3.3]. The optimized grit blasting parameters are given in **Table 3.2**. The grit material is grease cast iron.

Grit size #	24
Blasting angle (°)	75

Blasting pressure (MPa)	0.5
Blasting duration (s)	60
Standoff distance (mm)	100

Table 3.2 Grit blasting parameters

3.3. TWAS deposition parameters

All the sprayed coatings were deposited under the conventional conditions are given in **Table 3.3**.

Oxygen gas pressure	0.24 MPa
Spray distance	130 mm
Spraying angle	90°
Wire feed rate	0.06 m/s

Table 3.3 Twin-wire arc spraying deposition parameters

The coatings were deposited using Metallisation Ltd TWAS system of Algérie Métallisation Company (**Figure 3.3** and **Figure 3.4**).



Figure 3.3 Metallisation Ltd TWAS system of Algérie Métallisation Company: (1) Spraying gun (see **Figure 3.4**), (2) Wire control unit, (3) Wire speed panel, (4) Control panel, (5) Air compressor, (6) Gas cylinder

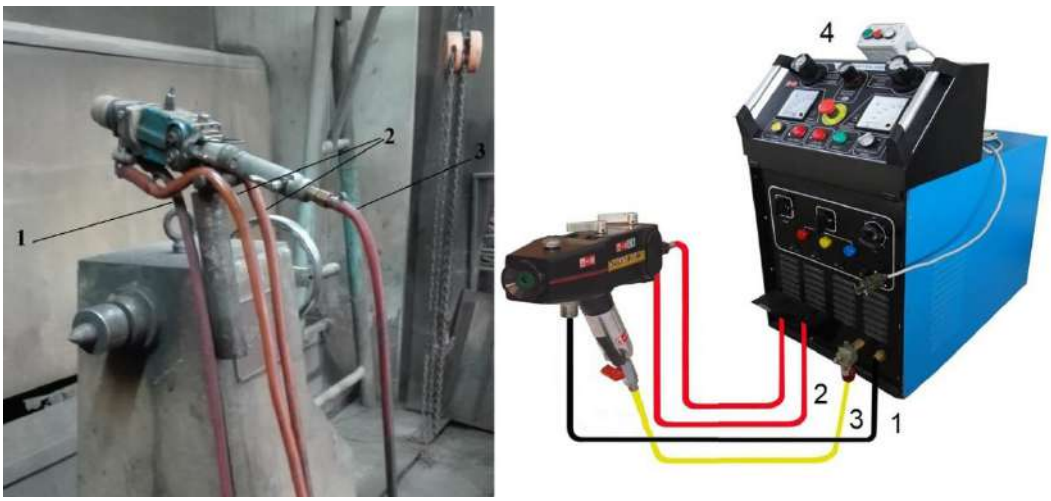


Figure 3.4 Metallisation Ltd TWAS system spraying gun: (1) Compressed air supply, (2) compressed air supply (for air motor), (3) Wire feed control cable, (4) Power source

The feed stocks are wires of 1.6 mm in diameter of commercial 304L and 317L. The chemical compositions of the wires are given in **Table 3.4** and **Table 3.5** respectively [3.4].

C %	Si %	Mn %	Cr %	P %	Ni %	S %
0.08	1.00	2.00	18.00-20.00	0.045	8.00-10.50	0.030

Table 3.4 304L wire chemical composition

C %	Si %	Mn %	Cr %	P %	Ni %	S %	Mo %
0.08	1.00	2.00	16.00-18.00	0.045	10.00-14.00	0.030	2.00-3.00

Table 3.5 317L wire chemical composition

3.4. Optimization of the annealing temperature to enhance the multilayered SSCs

Temperature (°C)	Time (hours)	Heating/cooling rate (°C/min)
800	4	10
1000	4	10
1100	4	10

Table 3.6 Annealing parameters

The annealing temperatures are similar to that reported by [3.5] for 304L SSC. According to what was reported before (see the literature review) annealing at temperatures below 500°C has no effect on the as-deposited stainless SSC, thereby the lowest annealing temperature used in our study will be 800°C. Also it was reported that generally for 304L SSCs it is recommended to use a range of annealing temperatures between 1010°C and 1120°C. So the

temperatures 1000°C and 1100°C will be used also. **Table 3.6** shows the annealing parameters used in our study.

In the literature review, it was found also that vacuum annealing shows the best results. So instead of using air annealing technique that was used by [3.5], vacuum annealing method was chosen.

The coatings vacuum annealing was carried out in a vacuum split tube furnace (OTF-1200X-II-UL, USA) of CDTA shown in **Figure 3.5**, with 10^{-5} MPa of vacuum. All the samples were furnace cooled.



Figure 3.5 OTF-1200X-II-UL vacuum split tube furnace of CDTA

3.5 PIII surface treatment

The optimized stainless steel coating will be treated by the PIII system of CDTA. The samples are treated inside a plasma reactor with an inductive RF source within 1 hour of time. The experimental system used for the PIII treatment is presented in **Figure 3.6** in two sides.



Figure 3.6 PIII treatment system of the CDTA: (1) Bottle of nitrogen gas, (2) PIII treatment chamber, (3) Pallet primary pump, (4) Secondary diffusion pump, (5) Power supply, (6) Throttle valve, (7) Secondary pump cooling water hose, (8) Pressure gauge, (9) Nitrogen passage hose

The system setup is shown with the sample during the treatment inside the plasma atmosphere in **Figure 3.7** (a) and (b) respectively.

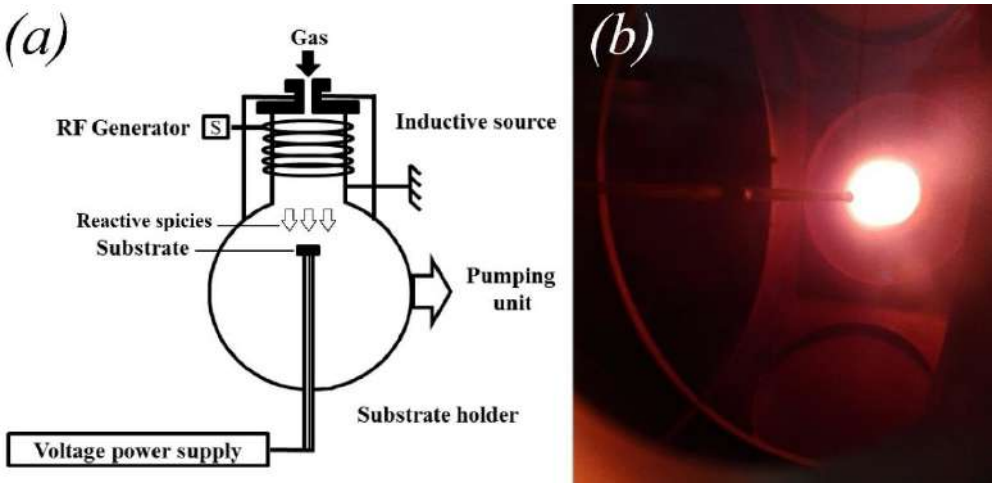


Figure 3.7 (a) CDTA PIII system setup [3.6], (b) a sample in the sample holder during the treatment inside the plasma atmosphere

The system consists of a spherical chamber of 930 mm in diameter which is connected to a primary pump and to a secondary oil diffusion pump for air pumping up to 10^{-2} mbar. The

distance between the plasma source and the sample is set at 100 mm. Before the PIII treatment, the samples were etched by argon ions Ar^+ bombardment for 5 min.

PIII treatment parameters are listed in **Table 3.7** in accordance to the optimizations done by [3.7] on carbon steel samples using the same system.

RF frequency	13.56 MHz	
Negative bias voltage	4.0 KV	
Injected power	200 W	300 W
Discharge gas	N_2 (100%)	
Working pressure	$8 \cdot 10^{-2}$ mbar	

Table 3.7 PIII treatment parameters

Two different injected powers are used which are: 200 W and 300 W in order to choose the optimal one for our coatings. Before nitrogen introduction, the system is evacuated to a pressure of $8 \cdot 10^{-6}$ mbar, and after the nitrogen injection, a working pressure of $8 \cdot 10^{-2}$ mbar is attained. The samples are negatively biased with a voltage of 4.0 KV which is the negative bias that gives the best hardness and corrosion resistance values according to [3.6] for treated carbon steel samples at an injected power of 200 W using the same system.

3.6. PVD thin film deposition parameters

W-Ti-N thin film was deposited using CDTA PVD magnetron sputtering system shown in **Figure 3.8**. The target is made of W-Ti (70 at.% W and 30 at.% Ti) with specific target power density of 10 W/cm^2. High-purity Argon was used as working gas and Nitrogen N_2 as reactive

gas. The N_2/Ar partial pressures ratio was set at 1/20 which is the ratio optimized previously by [3.8] and gives the lowest friction coefficient ever obtained for nitrides films. Prior to the thin film deposition, the samples were etched by argon ions Ar^+ bombardment for 5 min.

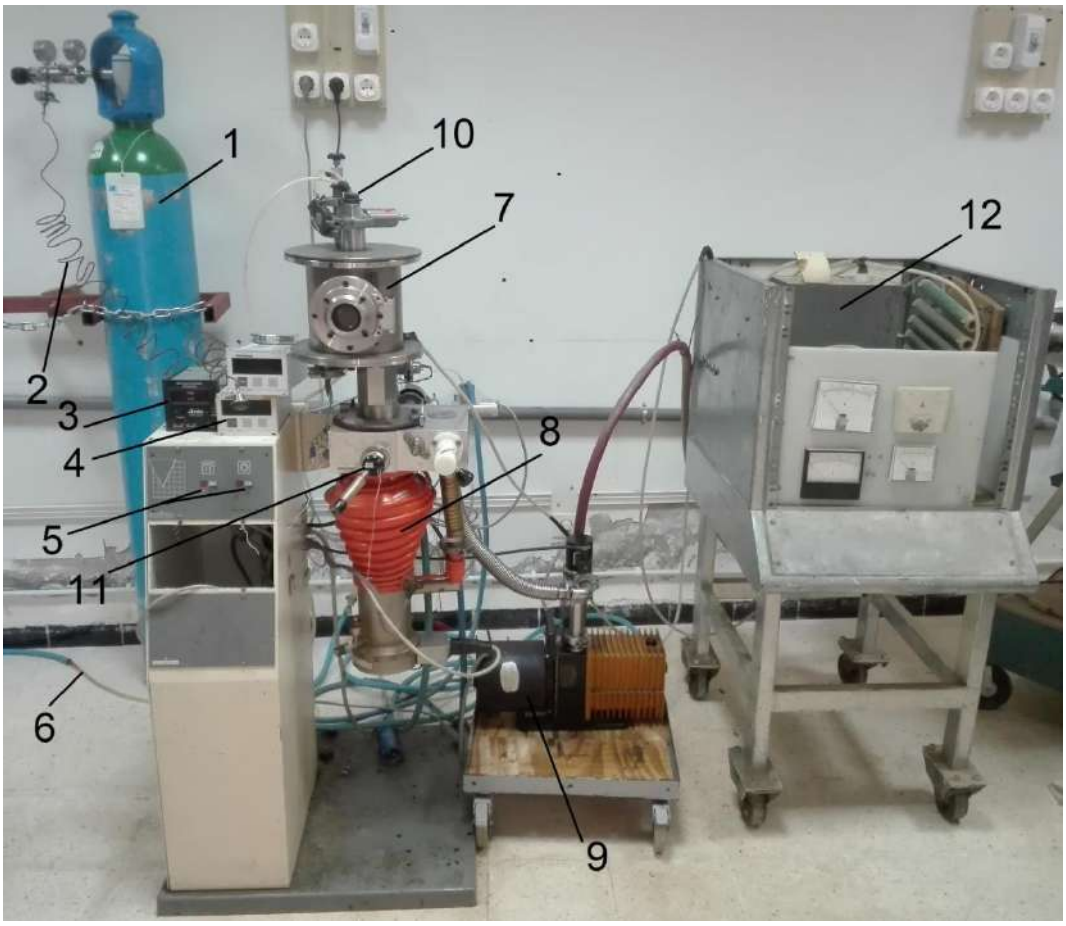


Figure 3.8 PVD magnetron sputtering installation of the CDTA: (1) Bottle of nitrogen gas, (2) Nitrogen passage hose, (3) Primary pressure gauge, (4) Secondary pressure gauge, (5) Primary and secondary pump ignition switches, (6) Secondary pump cooling water hose, (7) Deposition reactor, (8) Secondary diffusion pump, (9) Pallet primary pump, (10) Gas pressure control valve, (11) Throttle valve, (12) Power supply

Figure 3.9 shows the samples during the deposition of the W-Ti-N thin film inside the deposition reactor and the samples after the deposition of the film.

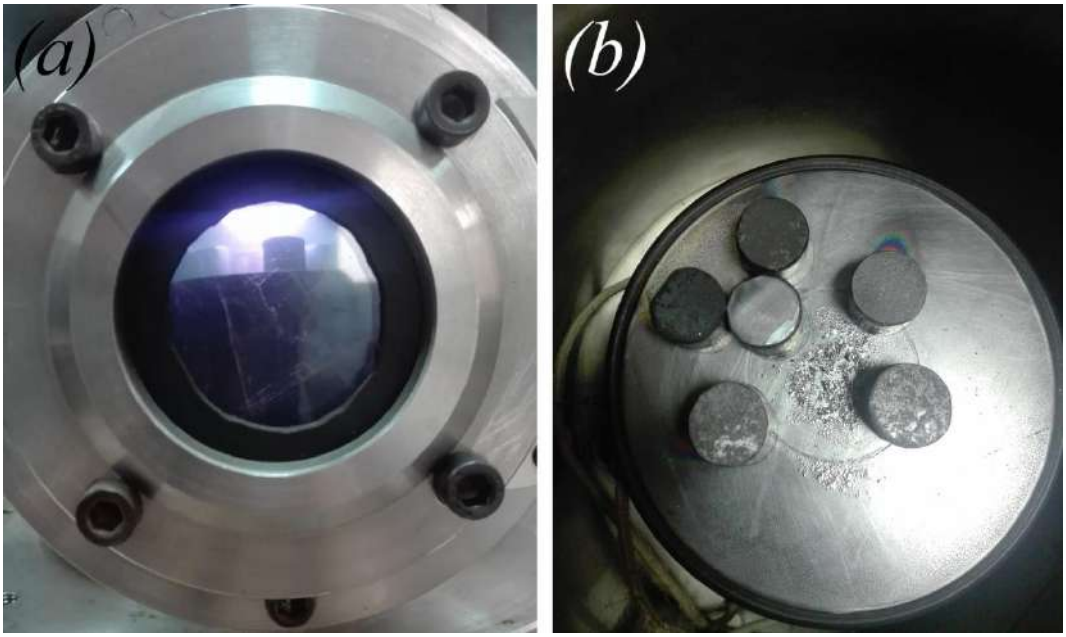


Figure 3.9 (a) The samples during the deposition of the W-Ti-N thin film inside the deposition reactor in the plasma atmosphere, (b) The samples after the deposition of the film

Table 3.8 lists the deposition parameters according to [3.8].

Primary pressure	$3 \cdot 10^{-2}$ mbar
Secondary pressure	$2.8 \cdot 10^{-5}$ mbar
Working pressure	$2 \cdot 10^{-2}$ mbar
Negative bias voltage	350 V
Specific target power density	10 W/cm^2
N_2/Ar	1/20
Deposition duration	10 min

Table 3.8 W-Ti-N thin film deposition parameters

3.7. Morphological and structural characterization

The coating phases analysis were carried out with XRD (Bruker D8 Advance, Germany) of CDTA shown in **Figure 3.10** with a Cu Kα radiation source of 0.15406 nm wavelength in the Bragg-Brentano configuration.

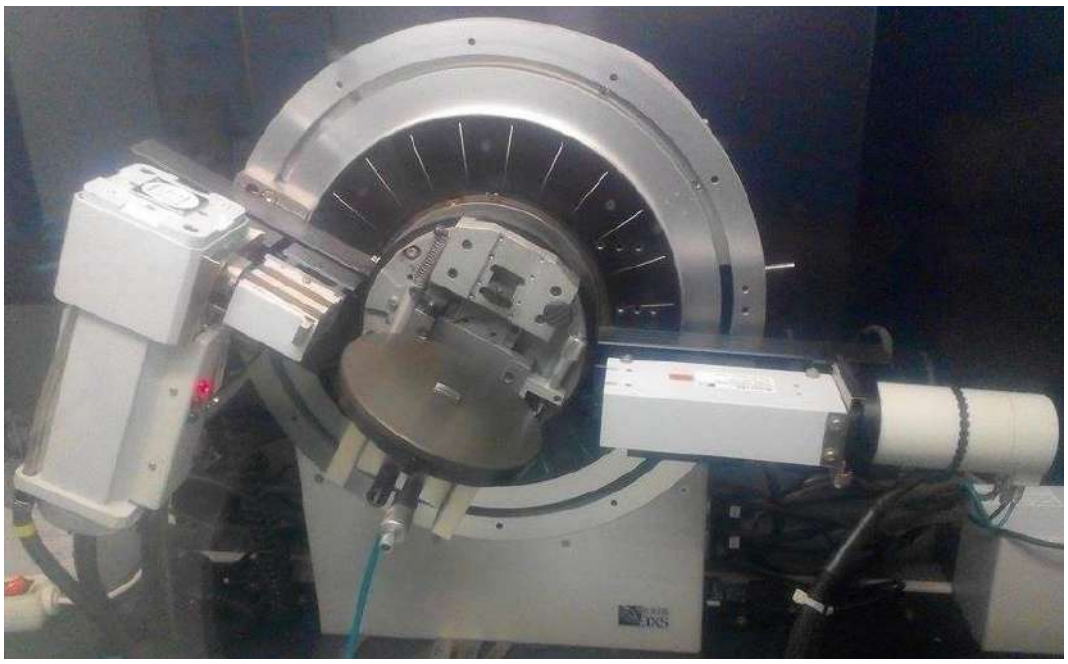


Figure 3.10 X-Ray Diffraction (XRD) setup of CDTA

Surface morphology and cross section of the coatings were analyzed by SEM (FEI Quanta 650, USA) coupled with EDS for the local chemical composition determination and it is shown in **Figure 3.11**. Before the SEM observations, the specimens were polished and etched in a nitric acid and diluted water.



Figure 3.11 Scanning Electron Microscopy (SEM) coupled with Energy-dispersive X-ray spectroscopy (EDS) of USDB

3.8. Mechanical Characterization

Nanohardness H and elastic modulus E of the different coatings are determined using a CSM Nano-indentation tester with a Berkovich diamond tip (pyramidal with triangular base geometry) of CDTA shown in **Figure 3.12**.



Figure 3.12 CSM Nano-indentation tester of CDTA

In order to reduce/avoid scale effect, substrate effect and the effect of the heterogeneous structure of the coating on the reliability of the indentation results 10 indentations at progressive depth values up to 10% of the thin film thicknesses to avoid the substrate effect and 4000 nm for the thick coatings. The nanoindentation depth values are chosen according to [3.9] recommendations, were the nanohardness value start to stabilize from a depth of 4 μm for the stainless steel thick coating (1.23 mm).

Table 3.9 summarizes the nanoindentation test parameters:

Number of indentations	10
Maximum indentation depth	4 μm for thick coatings 10% of the films thicknesses for thin films
Temperature	20 °C

Table 3.9 Nano-indentation test parameters

For the thick thermal sprayed coatings, nanoindentation tests are not sufficient and accurate due to the thickness of the coatings, so, Vickers hardness tests are necessary. Nemesis 9000 Vickers hardness tester of CRTI is used (**Figure 3.13**). The Vickers hardness parameters are 10 kgf of load and 15 s of loading time. Five indentations for each location of the coatings are made in order to get the hardness mean value.



Figure 3.13 Nemesis 9000 Vickers hardness tester of CRTI

3.9. Tribological characterization

The tribological tests are carried out using the CSM tribometer with ball-on-disc configuration of USTHB shown in **Figure 3.14**. The ball is mounted on a lever arm that associated with a displacement sensor. The coefficient of friction is determined during the test

by measuring the deflection of that elastic arm. The Tests performed by tribometer conforming to ASTM G99 & DIN 50324. The characteristics of the test are listed in **Table 3.10**.



Figure 3.14 CSM tribometer of USTHB

Geometry of the tip	Ball
Material of the tip	100Cr6 steel bearing balls
Radius of the ball	6 mm
Linear speed	2 cm/s
Normal load	5 N
Sliding distance	200 m
Sliding duration	166 min 40 s
Temperature (°C)	20 °C
Humidity	40 %

Table 3.10 Tribological tests parameters

Using higher normal loads, leads to the creation of oxide layers that can be considered as self-lubrication as reported by [3.10] who were used loads ranged between 10 N to 40 N. In order to avoid any overestimated results, the chosen normal load was 5 N which is lower than the minimum of that range.

The wear rates are measured experimentally using the Archard formula (2.1) [3.11].

$$k = \frac{V_k}{D \cdot F} \qquad (3.1)$$

k: Wear rate ($mm^3/N{\cdot}m$);

V_k: Wear volume losses (mm^3);

D: Sliding distance (m);

F: Normal load (N).

The wear volume is calculated from the wear track width and depth that are measured from the wear track 3D images obtained through the AFM (A100) of the University of UYFM with its Gwyddion program shown in **Figure 3.15**.



Figure 3.15 A100 AFM of UYFM

The wear tracks profiles were observed using the OM (Optika B-383 MET) of the UYFM, shown in **Figure 3.16**.



Figure 3.16 Optika B-383 MET OM of UYFM

3.10. Electrochemical characterization

Electrochemical characterization of the samples was carried out using a Parstat4000 potentiostat/Galvanostat of CDTA with its VesaStudio program shown in **Figure 3.17**. Electrochemical measurements were conducted in a conventional three electrode cell. The electrolyte used was a 3.5 wt. % NaCl aqueous solution, which is the conventional NaCl concentration for such tests. The studied specimens were used as the working electrodes, carbon electrode as the counter electrode and saturated calomel electrode as the reference electrode. Prior to the electrochemical tests, the samples were sealed with the epoxy resin. The immersion time was 3 hours. The Nyquist plots were used to describe the corrosion behaviours. E_{corr}, i_{corr}, and C_R are extracted from the plots with the Tafel extrapolation method [3.12].

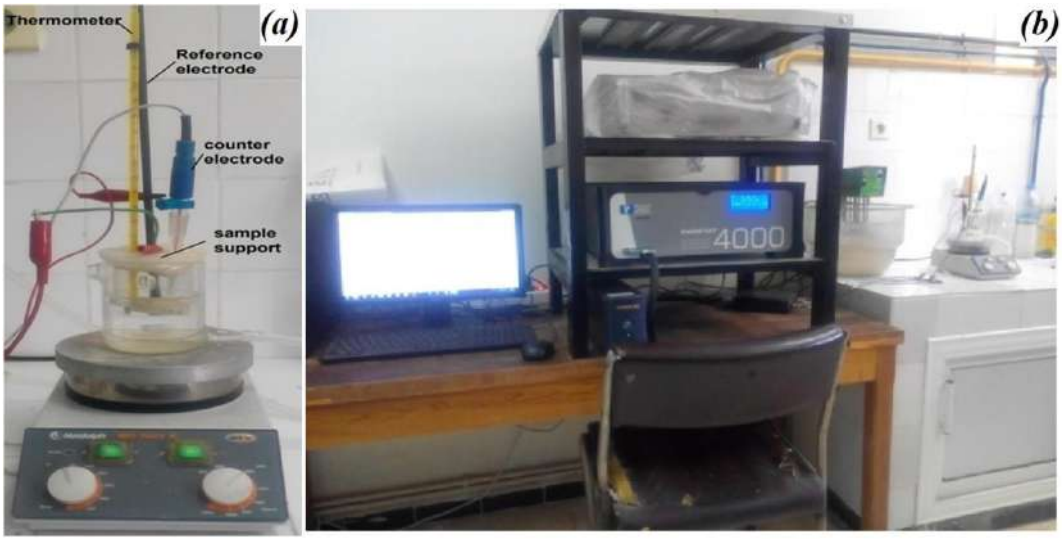


Figure 3.17 (a) Electrochemical test Cell, (b) Electrochemical test Assembly of CDTA

3.11. Performance factor K_p

This study is mainly a tribological study, its first objective is to optimize the tribological properties of the stainless steel coatings and in order to compare between coatings after each optimization step, the performance factor K_P is introduced. This factor will be used later to perform the techno- economic assessment between different optimized coatings.

The performance factor is depended on four parameters: Hardness H [N/mm^2], friction coefficient μ [N/N], Wear rate k [mm^3/N·m] and corrosion rate C_R [mm/year]. The first factor must be increased as much as possible and the others three factors must be decreased as much as possible, thereby, the performance factor formula will be given as (3.2):

$$K_p\ (\mu, k, C_R, H) = \frac{H}{C_r \cdot \mu \cdot k}\ [N^2 \cdot year/mm^5] \quad (3.2)$$

References

[3.1] http://www.steels-supplier.com/steel-standard/en10025_2_specification.html

[3.2] P.K. Chander, M. Vashista, K. Sabiruddin, S. Paul, and P.P. Bandyopadhyay, Effects of grit blasting on surface properties of steel substrates, *Mater. Des.*, 2009, **30**, p 2895-2902.

[3.3] S. Amada, T. Hirose and T. Senda, Quantitative evaluation of residual grits under angled blasting, *Surf. Coat. Technol.*, 1999, **111**, p 1-9.

[3.4] https://www.bosunsupplies.com/stainless-steel-info.html

[3.5] P. Coddet, C. Verdy, C. Coddet, F. Debray and F. Lecouturier, Mechanical properties of thick 304L stainless steel deposits processed by He cold spray, *Surf. Coat. Technol.*, 2015, **277**, p 74-80.

[3.6] M.M. Alim, N. Saoula, R. Tadjine, F. Hadj-Larbi, A. Keffous and M. Kechouane, Improvement in nano-hardness and corrosion resistance of low carbon steel by plasma nitriding with negative DC bias voltage, *Eur. Phys. J. Appl. Phys.*, 2016, **75**, 30801.

[3.7] M. M. Alim, R. Tadjine, A. Keffous and M. Kechouane, Improvement in Electromechanical and Electrochemical of Low Carbon Steel Samples by PIII Treatment, *Proceedings of the 1st International Conference on Renewable Energy and Energy Conversion*, 2019, p 523-530.

[3.8] K. Chemaa, Y. Chabani, M. Gaceb and S. Hassani, "Study of tribological properties of titanium-based thin films applied to the rubbing parts of internal combustion engines piston", Master degree Thesis, M'hamed Bougara University Boumerdes, 2017.

[3.9] J. Nohava, R. Mušálek, J. Matějíček and M. Vilémová, A contribution to understanding the results of instrumented indentation on thermal spray coatings - Case study on Al_2O_3 and stainless steel, *Surf. Coat. Technol.*, 2014, **240**, p 243-249.

[3.10] H. Guo, S. Zhang, W. Sun and J. Wang, Differences in dry sliding wear behavior between HVAF-sprayed amorphous steel and crystalline stainless steel coatings, *J. Mater. Sci. Technol.*, 2019, **35**, p 865-874.

[3.11] K. Sail, H. Aouici, S. Hassani, B. Fnides, A. Belaadi, A. Naitbouda and S. Abdi, Influence of tribological parameters on S335 steel filing Ti-W-N in dry sliding wear: Prediction model and sliding condition optimization, *Intern. J. Adv. Manufacturing Technol.*, 2017, **92**, p 4057-4071.

[3.12] A. Berradja, Electrochemical Techniques for Corrosion and Tribocorrosion Monitoring: Methods for the Assessment of Corrosion Rates, Corrosion Inhibitors, 2019.

Chapter 4

Surface behaviour optimization of austenite stainless steel coatings

4.1. Comparative investigation of 304L and 317L SSCs behaviours

4.1.1. Introduction to the first optimization

The aim of the first optimization is to choose a SSC with the best surface behaviour between 317L-SSC and 304L-SSC according to their mechanical, tribological and electrochemical properties. The both coatings have not been studied extensively before in comparison with the well-known 316L SSC. Massive 304-SSB is used as a reference material.

The coating with the best properties will be optimized more later on in this chapter.

4.1.2. Microstructural results of the first optimization

Figure 4.1 shows the surface morphologies with magnified regions of: (a) 304L-SSC, (b) 317L-SSC. It can be seen that 304L SSC and 317L SSCs are made up by the typical spray splats [4.1, 4.2] formed after a rapid solidification of the melted particles upon their impact [4.3], that are bonded to each other, with some semi-molten particles to give coatings with lamellar structure [4.4], suggesting that the most of the sprayed particles were well melted

before their impact to the substrate surface [4.5]. 304L-SSC microstructure shows reduced splats sizes which can be attributed to the intense plastic deformation of the semi-melted particles (spherical splats) during collision with the substrate [4.5]. With higher splats sizes, the number of the inter-splats boundaries which are responsible for decreasing the coating cohesive strength will be lower, resulting in a more compact coating and better surface properties.

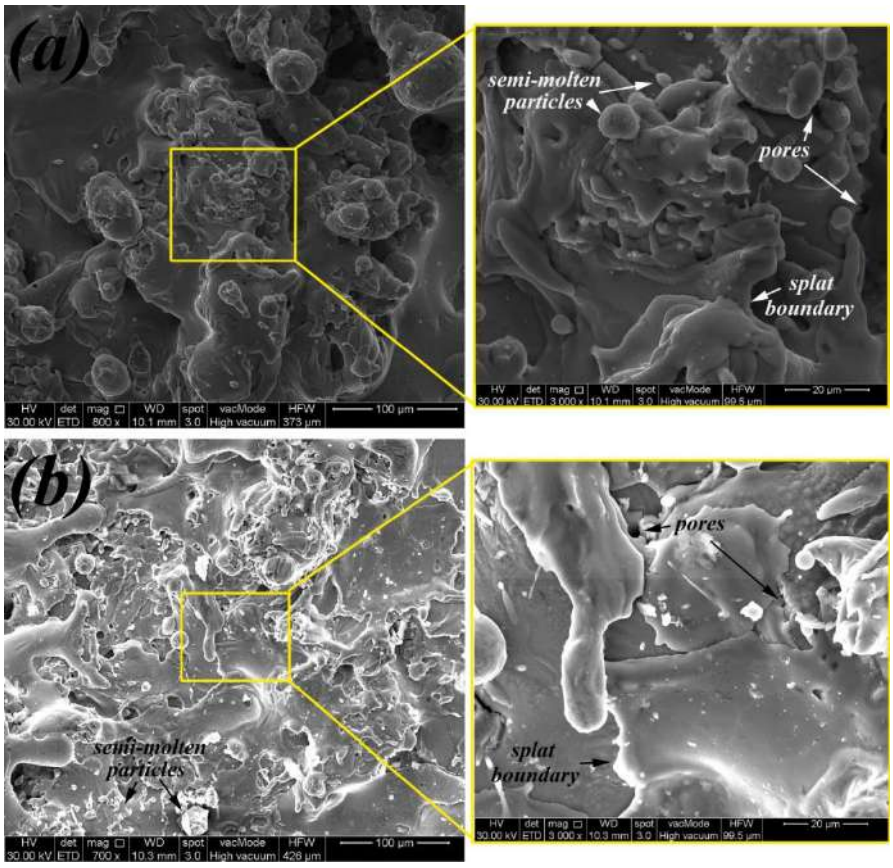
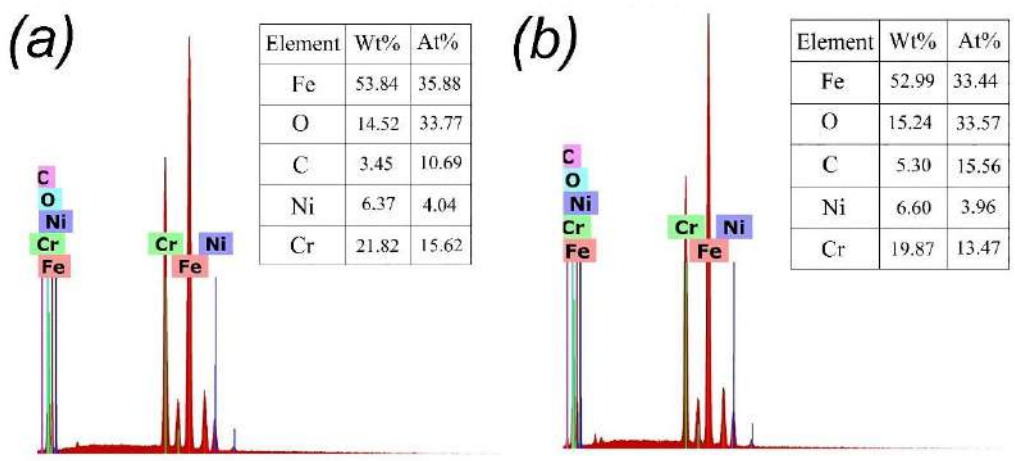


Figure 4.1 SEM micrographs of: (a) 304L-SSC and (b) 317L-SSC

EDS spectra shown in **Figure 4.2** (a) and (b) detects the presence of the elements: Fe, O, C, Ni and Cr. Additionally, quantitative analysis reveals that the oxides concentration in 317L-SSC surface (15.24 wt.%) is slightly higher than that in 304L-SSC (14.52 wt.%). The high oxides content in the coatings results from the oxidation of the particles in the arc and/or during the droplets in-flight to the substrate [4.6].



Element	Wt%	At%
Fe	53.84	35.88
O	14.52	33.77
C	3.45	10.69
Ni	6.37	4.04
Cr	21.82	15.62

Element	Wt%	At%
Fe	52.99	33.44
O	15.24	33.57
C	5.30	15.56
Ni	6.60	3.96
Cr	19.87	13.47

Figure 4.2 EDS spectra of: (a) 304L-SSC and (b) 317L-SSC

Figure 4.3 shows the roughness arithmetic mean (Ra) for the two coatings. 317L-SSC presents a lower Ra value than 304L-SSC (195.64±1.51 nm and 209.00±1.24 nm respectively). Roughness is related to the splats morphologies and to their sizes [4.6]. 317L-SSC has wider splats with low semi-melted particles. Thus, 317L-SSC has a fine surface with a lower roughness.

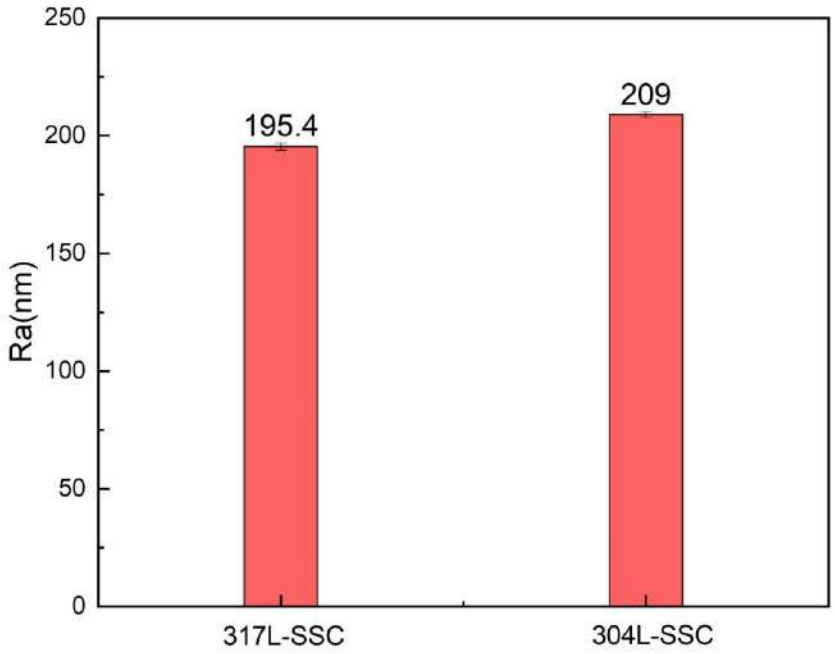


Figure 4.3 Roughness analysis results for 304L-SSC and 317L-SSC

SEM cross-section images for 304L-SSC and 317L-SSC are shown in **Figure 4.4** (a) and (b) respectively. It can be seen that both coatings are made up by smooth structures and that defects such as pores and interlamellar cracks can be observed also. The existence of pores is related to the lack of bonding between the different layers and the presence of the semi-molten particles [4.7]. The gas trapping during the solidification process of the coating can cause also the pores formation [4.8]. The formation of cracks is attributed to the distortion of the sprayed particles during the deposition. Those particles generate residual stresses inside the coatings and thereby, form cracks [4.9]. The obtained coatings thicknesses are 434.58±2.94 µm for 304L-SSC and 432.66±2.66 µm for 317L-SSC.

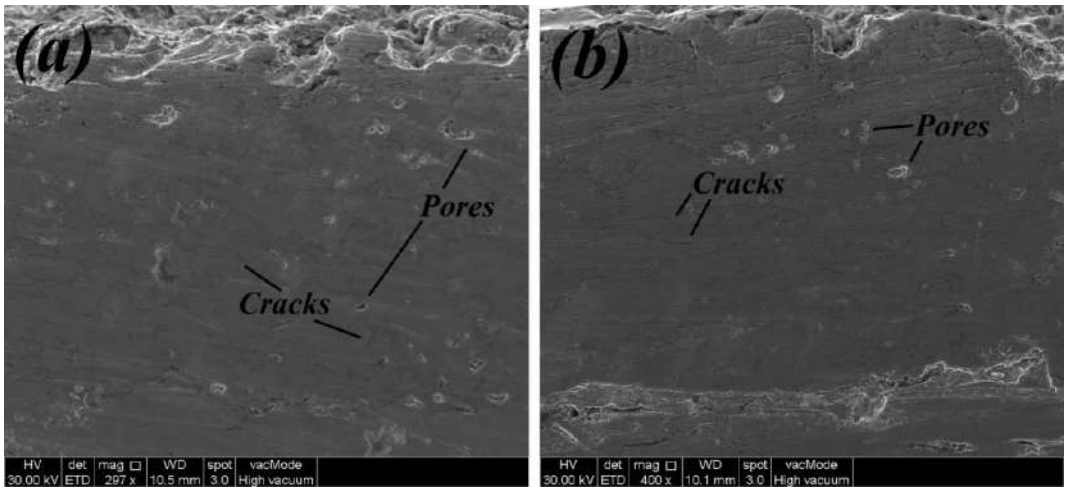


Figure 4.4 SEM cross-section of: (a) 304L-SSC and (b) 317L-SSC

Figure 4.5 presents the XRD patterns for 304-SSB, 304L-SSC and 317L-SSC. The metastable γ-Fe phase shows the highest intensity in both coatings [4.10] suggesting that is the main phase for both coatings.

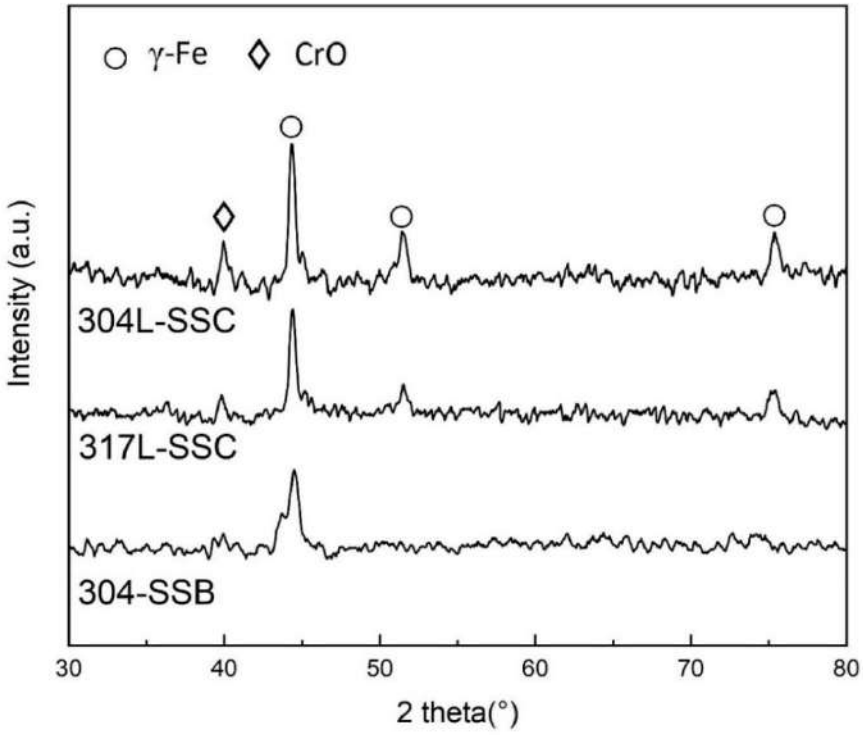


Figure 4.5 XRD diffraction patterns of: 304-SSB, 317L-SSC and 304L-SSC

CrO peaks are also observed [4.11, 4.12]. The high amount in austenite and the absence of ferrite/martensite (α-Fe) in the two coatings are because they were exposed to less heat during the arc spraying process, which leads to less phase transformation from γ-Fe into α-Fe [4.13].

4.1.3. Mechanical results of the first optimization

Figure 4.6 shows the nanohardness and the Vickers hardness measurements results for: 317L-SSC, 304L-SSC and 304-SSB. It can be seen that 317L-SSC has a Vickers hardness of H=213.7±5.6 HV_{10} and a nanohardness of H_N=9.1±1.0 GPa which is slightly higher than the hardness of 304L-SSC (H=204.9±6.8 HV_{10} and H_N=8.7±0.4 GPa), this can be related to the higher coating thickness which leads to an improved compactness [4.14] and hardness [4.15]. The two coatings have higher hardness than 304-SSB (H=201.3±1.2 HV_{10} and H_N=6.7±0.2 GPa).

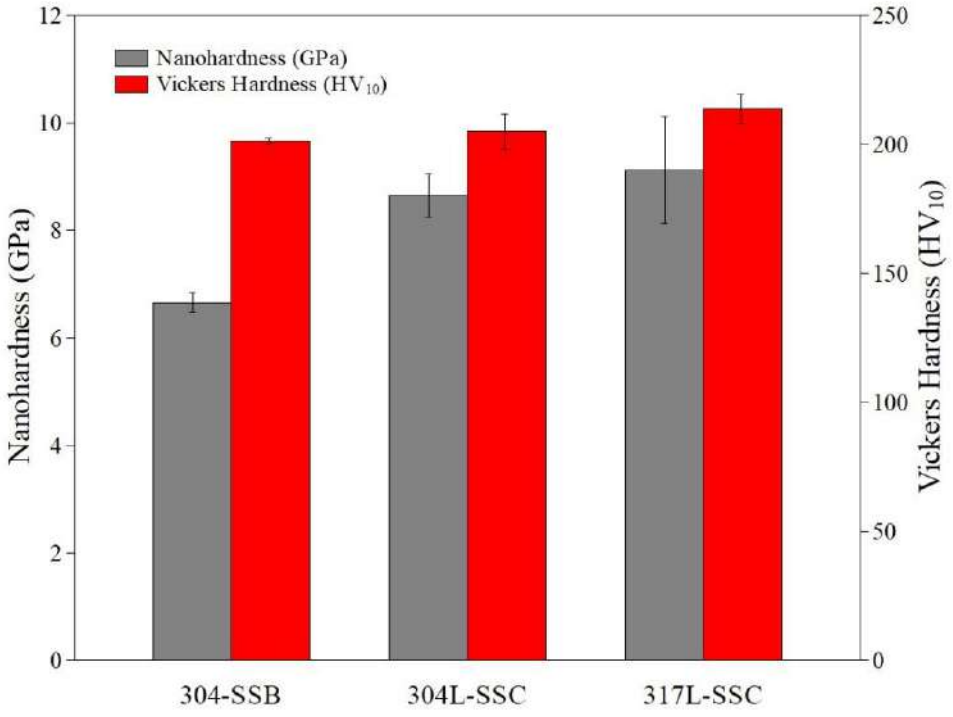


Figure 4.6 Hardness measurement results for: 317L-SSC, 304L-SSC and 304-SSB

Table 4.1 shows the nanoindentation test results for 317L-SSC, 304L-SSC and 304-SSB. For effective coatings protection, H^3/E^2 hardness to elastic modulus ratio known by resistance to plastic deformation, should be maximized. 317L-SSC has the highest H^3/E^2 value of 0.015 GPa followed by 304L-SSC with 0.013 GPa indicating a better wear resistance [4.16].

Samples	H (GPa)	E (GPa)	H^3/E^2 (GPa)
317L-SSC	9.1±1.0	226.1±9.3	0.015
304L-SSC	8.7±0.4	223.3±13.3	0.013
304-SSB	6.7±0.2	183.7±11.4	0.009

Table 4.1 Nanoindentation test results of: 317L-SSC, 304L-SSC and 304-SSB

The above resistances to plastic deformation results are confirmed by the typical nanoindentation load-displacement curves shown in **Fig.4.7**. The area between the loading and the unloading curves defines the plastic deformation work W_P. The smaller W_P, the higher the resistance to plastic deformation is [4.17]. The curves show that the resistance to plastic deformation of 317L-SSC is higher than that of 304L-SSC, followed by 304-SSB. From the nanoindentation load-displacement curves, the elastic recoveries for all the three samples are calculated and their values are 68% for 317L-SSC, 65% for 304L-SSC and 21% for 304-SSB.

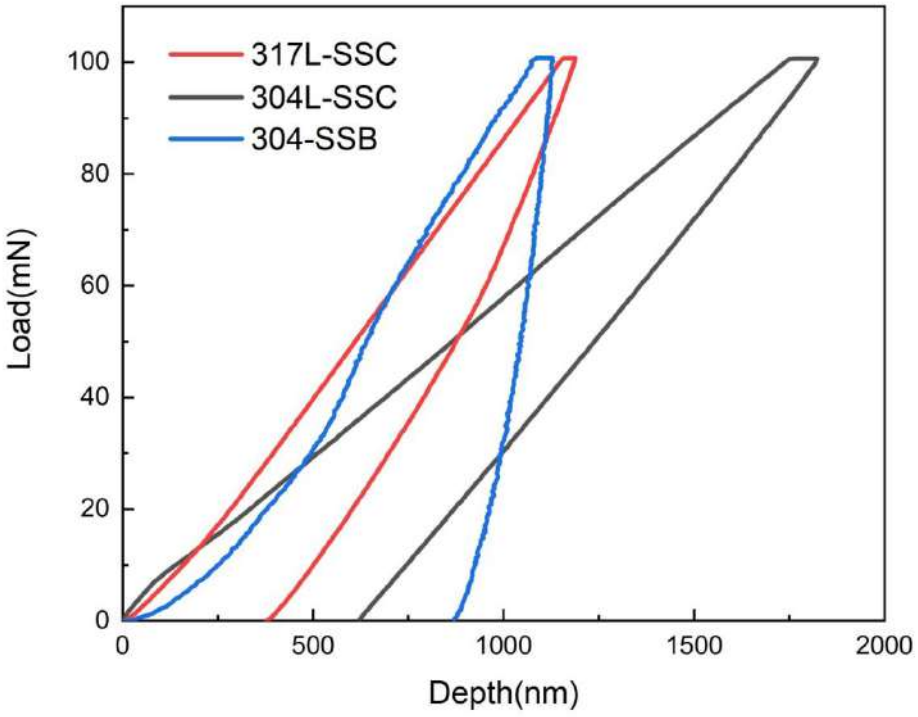


Figure 4.7 Typical nanoindentation curves for: 304L-SSC, 317L-SSC and 304-SSB

4.1.4. Tribological results of the first optimization

Figure 4.8 presents the COF variation as a function of the sliding distances for: 317L-SSC, 304L-SSC and 304-SSB. The friction curves for all the three samples exhibits two stages

according to their COF values. The first stage is characterized by a rapid increase of the COFs until they reach peak values of μ≈0.78 for 317L-SSC, μ≈0.73 for 304L-SSC and μ≈0.84 for 304-SSB. The second stage starts by a decreasing trend followed by stabilization. The rapid initial increase of the COF in first stage can be caused by the initially high adhesive contact between the steel ball counterbody and the coatings material [4.7]. The decreasing trend in the second stage can be ascribed to the work hardening of the coating under compressive stresses [4.8]. Finally, the generation and the spallation of wear debris reach a steady-state and oxide film can be formed on the worn surface resulting in the friction coefficient stabilization.

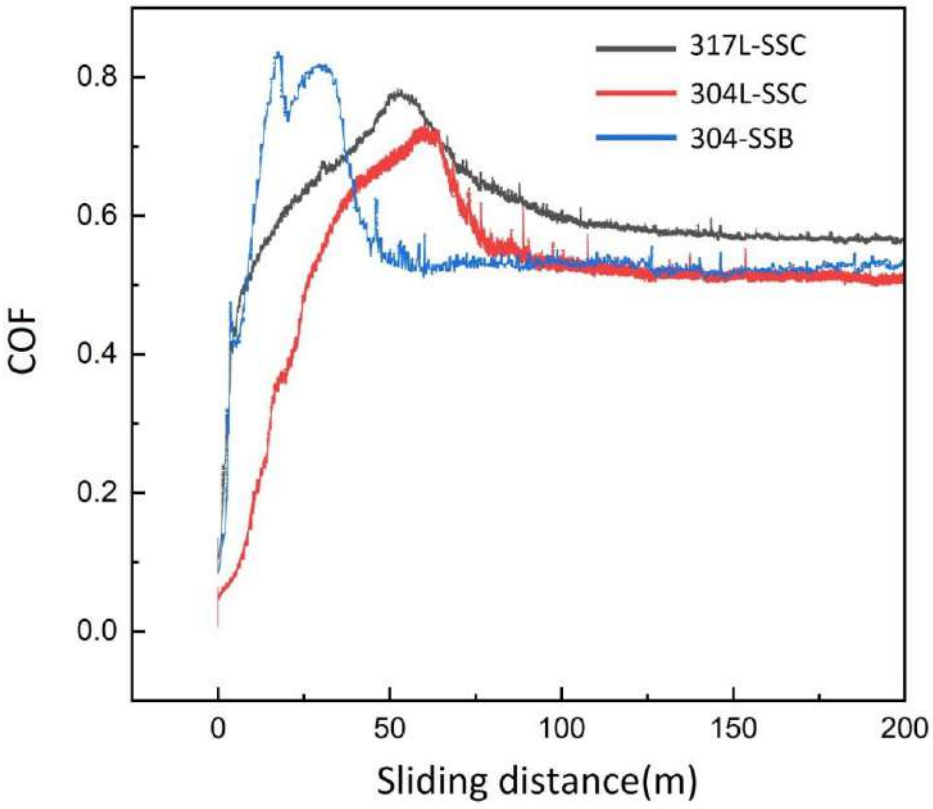


Figure 4.8 COF variations as function of the sliding distance for: 317L-SSC, 304L-SSC and 304-SSB

Table 4.2 lists the tribological test results. According to the **Table 4.2**, 304L-SSC presents the lowest COF of μ=0.52±0.15, while those of 317L-SSC and 304-SSB are respectively

μ=0.61±0.11 and μ=0.56±0.12. 317L-SSC presents the lowest wear rate (k=1.38±0.02·10^{-4} mm^3/N·m) and so the highest wear resistance than 304L-SSC and 304-SSB (k=2.63±0.06·10^{-4} mm^3/N·m and k=30.80±0.52·10^{-4} mm^3/N·m respectively). The lower wear rate of 317L-SSC can be attributed to its higher hardness than 304L-SSC and 304-SSB [4.3]. According to the Archard wear theory, the wear resistance of a coating is proportional to its hardness [4.17].

Samples	**317L-SSC**	**304L-SSC**	**304-SSB**
COF	0.61±0.11	0.52±0.15	0.56±0.12
k x10^{-4} (mm^3/N·m)	1.38±0.02	2.63±0.06	30.80±0.52

Table 4.2 Tribological test results of: 317L-SSC, 304L-SSC and 304-SSB

Figure 4.9 (a), (b) and (c) shows the AFM 3D images of the wear tracks and surface profiles for: 317L-SSC, 304L-SSC and 304-SSB respectively. 317L-SSC. 304L-SSC has the shallowest wear depth of D_P=0.08 mm, while that of 304-SSB is the deepest with D_P=1.41 mm. 317L-SSC has a wear depth of D_P=0.14 mm. Wear track width measurements reveal in the other side that 317L-SSC presents the narrowest wear track with w=0.063 mm and 304-SSB has the widest one with w=0.273 mm. 304L-SSC has a wear width of w=0.197 mm. Shallower and narrower wear tracks are obtained on the surface of the two coatings in than those of 304-SSB, suggesting excellent wear protection in comparison with the stainless steel ball valves material.

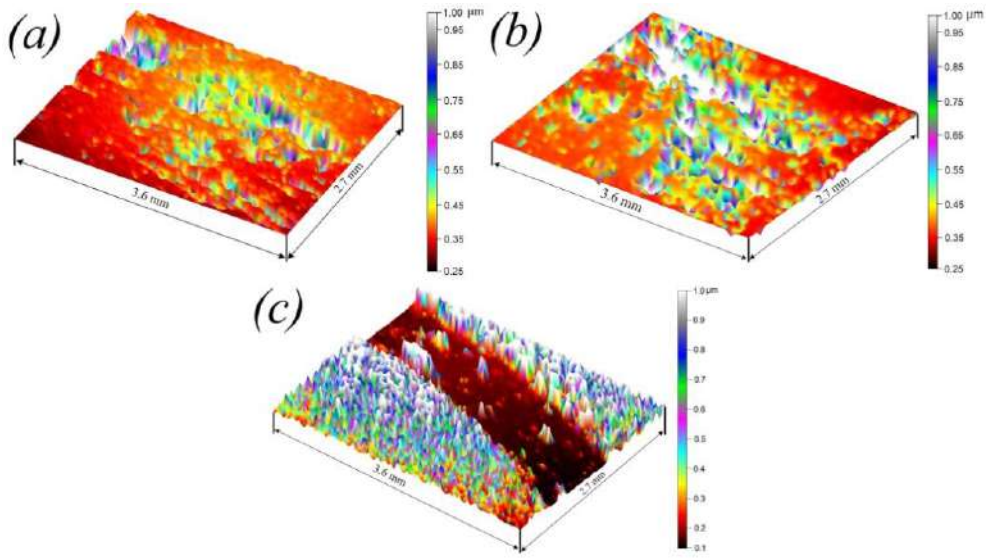


Figure 4.9 AFM 3D wear tracks profiles for: (a) 317L-SSC, (b) 304L-SSC and (c) 304-SSB

Figure 4.10 (a), (b), and (c) show the wear tracks observations for 317L-SSC, 304L-SSC and 304-SSB respectively. Deep grooves and scaling pits in the wear direction can be observed for the two coatings, suggesting that both of them are subjected to delamination wear that is accompanied with abrasive wear. For 304-SSB, deeper grooves can be seen, which are signs of severe abrasive wear [4.16].

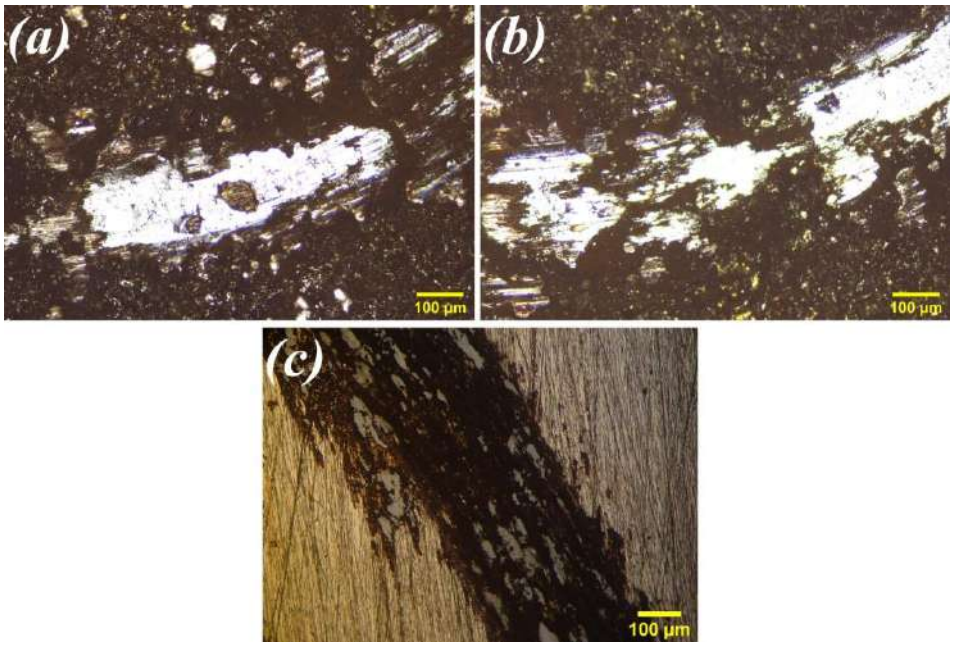


Figure 4.10 OM wear tracks observations for: (a) 317L-SSC, (b) 304L-SSC and (c) 304-SSB

In the beginning of the test, when the counterbody slides against the coatings surfaces, the coatings are subjected to alternate tensile stresses and compression stresses [4.18], those alternate stresses represent a low frequency fatigue process [4.19] that take place at shallower position beneath the coating surfaces [4.20] with intensities as high as the cohesive strengths of the coatings inter-splats [4.9]. When fatigue damage accumulates to a certain value, cracks initiates at the inter-splats boundaries [4.19]. Cracks can be easily generated in the inter-splats boundaries due to their weak bonds [4.20]. The cracks propagate in the boundaries and reduce as a consequence the coatings inter-splats cohesive strength, leading to the spallation of the splats and the formation of the scaling pits. By repeating the above process delamination wear will occur [4.18]. With increased sliding distance, the wear debris in the worn surfaces lie between the ball and the surfaces act as abrasive third bodies and accelerate the wear process more severely with abrasive wear mode.

4.1.5. Electrochemical results of the first optimization

The polarization curves of 317L-SSC, 304L-SSC and 304-SSB are shown in **Figure 4.11**. The corrosion fitting parameters E_{OCr}, i_{corr} and C_R are extracted from the polarization curves and listed in **Table 4.3**.

Samples	C_R (mpy)	E_{oc} (V)	i_{corr} (µA/cm^2)
317L-SSC	27.03	-0.618	62.26
304L-SSC	13.03	-0.615	30.02
304-SSB	0.772	-0.238	1.78

Table 4.3 Corrosion results extracted from the corrosion polarization curves

The two coatings present higher current density than 304-SSB and so lower corrosion protection owing to the coatings defects such as oxides and pores. Through the coatings pores,

the electrolyte penetrates to reach and to corrode the substrate surface. In addition, the coating oxides such as the iron oxide [4.21] and the chromium oxide [4.10] impair the corrosion protection ability of the coatings by changing their electrochemical potential after their dissolution in the electrolyte. Despite such low protection ability, the present two coatings have better corrosion behaviours than the 316L SSC deposited by CGS that has E_{OC} between -1.0 V and -0.53 V [4.22] and -1.01 V for the same coating deposited by HVOF [4.15]. Such results can be related to the low porosity of the two obtained coatings. 304L-SSC presents more positive E_{corr} and lower i_{corr} and so higher corrosion resistance than 317L-SSC. Such difference in the corrosion behaviour can be attributed to its denser microstructure and lower porosity [4.23]. The higher chromium content (21.82 wt.% for 304L-SSC and 19.87 wt.% for 317L-SSC) as it was shown in **Figure 4.2** can play also a significant role for such higher corrosion resistance [4.23].

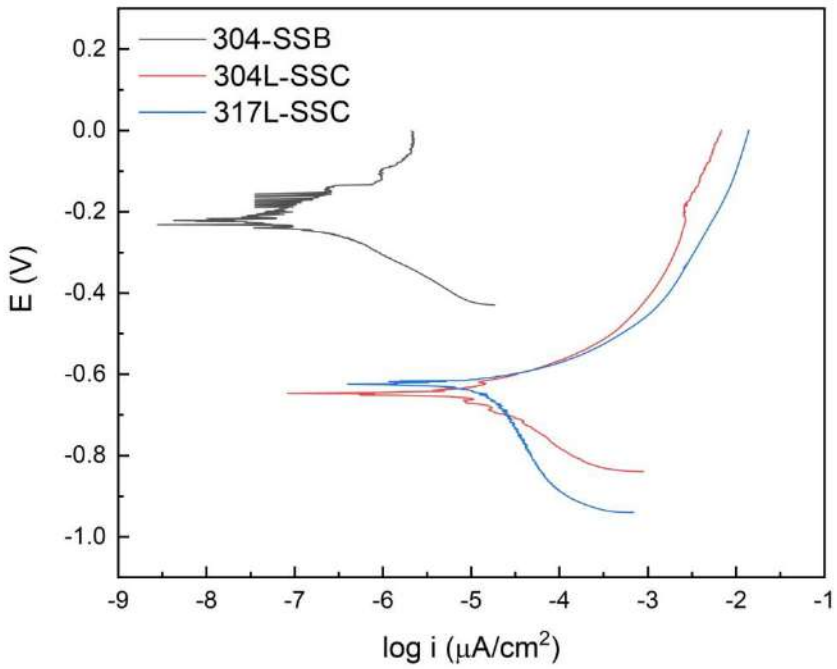


Figure 4.11 Polarization curves of: 317L-SSC, 304L-SSC and 304-SSB

4.1.6. The performance factors: $Kp_{1(304L\text{-}SSC)}$, $Kp_{1(304L\text{-}SSC)}$ and $Kp_{1(304\text{-}SSB)}$

A qualitative comparison between the different samples according to their hardness, elastic modulus, friction coefficient, wear rate and corrosion rate is given in the polar diagram shown in **Figure 4.12**. The diagram reveals that 304L-SSC has high hardness and elastic modulus, while having low wear rate and COF, suggesting that it has good surface behaviour.

The above qualitative assessment can be confirmed by calculating the performance factors of the four coatings using the equation (3.3), we can calculate the correspondent performance factors of the different sample in order to evaluate the optimal coating after carrying out the first optimization.

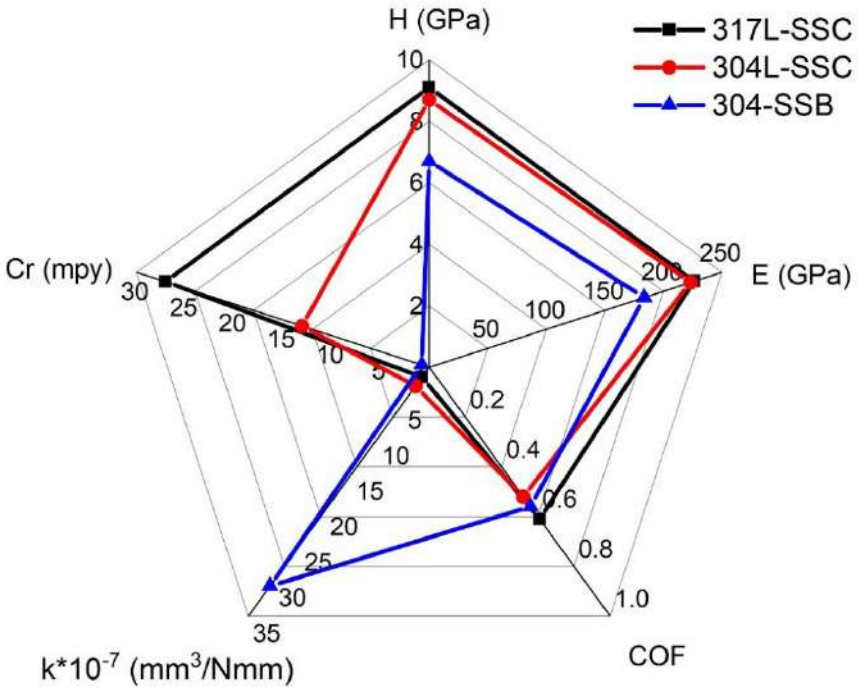


Figure 4.12 Polar diagrams providing a qualitative comparison of the samples: 317L-SSC, 304L-SSC and 304-SSB

The performance factors of: 317L-SSC, 304L-SSC and 304-SSB are respectively: $Kp_{1(317L\text{-}SSC)}$, $Kp_{1(304L\text{-}SSC)}$ and $Kp_{1(304\text{-}SSB)}$, and they can be calculated using respectively the laws: (4.1), (4.2) and (4.3), given as the following:

$$K_{P1(317L-SSC)} = \frac{H_{(317L-SSC)}}{C_{r(317L-SSC)} \cdot \mu_{(317L-SSC)} \cdot k_{(317L-SSC)}} \ [N^2 \cdot year/mm^5] \ (3.1)$$

$$K_{P1(304L-SSC)} = \frac{H_{(304L-SSC)}}{C_{r(304L-SSC)} \cdot \mu_{(304L-SSC)} \cdot k_{(304L-SSC)}} \ [N^2 \cdot year/mm^5] \ (3.2)$$

$$K_{P1(304-SSB)} = \frac{H_{(304-SS)}}{C_{r(304-SS)} \cdot \mu_{(304-SS)} \cdot k_{(304-SS)}} \ [N^2 \cdot year/mm^5] \ (3.3)$$

The different factors values are given in **Table 4.4**:

Samples	**H (N/mm^2)**	**C_R (mpy)**	**μ**	**k (mm^3/N·mm)**
317L-SSC	$9.1 \cdot 10^3$	27.03	0.61	$1.38 \cdot 10^{-7}$
304L-SSC	$8.7 \cdot 10^3$	13.03	0.52	$2.63 \cdot 10^{-7}$
304-SSB	$6.7 \cdot 10^3$	0.77	0.56	$30.80 \cdot 10^{-7}$

Table 4.4 Factors values of: 304L-SSC, 317L-SSC and 304-SSB

The calculated factors of performance are:

$$K_{P1(317L-SSC)} = 4.00 \cdot 10^9 \ N^2 \cdot year/mm^5$$

$$K_{P1(304L-SSC)} = 4.88 \cdot 10^9 \ N^2 \cdot year/mm^5$$

$$K_{P1(304-SSB)} = 5.04 \cdot 10^9 \ N^2 \cdot year/mm^5$$

It is clearly seen that the performance factor of 304L-SSC is higher than that of 307L-SSC and very close to 304-SSB due to its higher corrosion rate in comparison with 317L-SSC and

the lowest friction coefficient than 317L-SSC and 304-SSB, while it has slightly lower nanohardness (and Vickers hardness) and wear rate than 317L-SSC.

From the first optimization results, 304L-SSC will be optimized more in the next sub-chapters in order to enhance its surface properties using different optimizations methods given in chapter 1. PIII nitruration treatment and W-Ti-N thin film will be applied on the optimal 304L SSC in the next chapters.

4.2. Study of the surface behaviours of 304L-SSC multilayer

4.2.1. Introduction of the second optimization

Sample reference	Arc Voltage (V)	Arc Current (A)	Air pressure (MPa)	Spray distance (mm)	Wire feed rate (m/s)	Number of layers
SS-1L	38	100	0.38	130	0.06	1 layer
SS-2L						2 Layers
SS-3L						3 Layers
SS-4L						4 Layers

Table 4.5 Spray parameters of the second optimization

After selecting the SSC grade that has best surface behaviour which is the 304L-SSC, it is now time to do the second optimization step in order to enhance its surface properties. The second optimization consists of the variation of the number of layers from 1 to 4, doing the different surface characterizations and then introduce the obtained results into the performance factor K_p equation to select the optimal number of layers and to compare it with that of the 304-SSB. To know more about the effect of using multilayered SSCs on the

surface properties see chapter 1. The spray parameters are listed in **Table 4.5**. We should mention that the 304L-SSC coating will be referred to by SS-1L coating in the current sub-chapter. All the characterization equipment and parameters are listed with details in chapter 3.

4.2.2. Microstructural results of the second optimization

Figure 4.13 shows the XRD patterns for SS-1L, SS-2L, SS-3L and SS-4L.

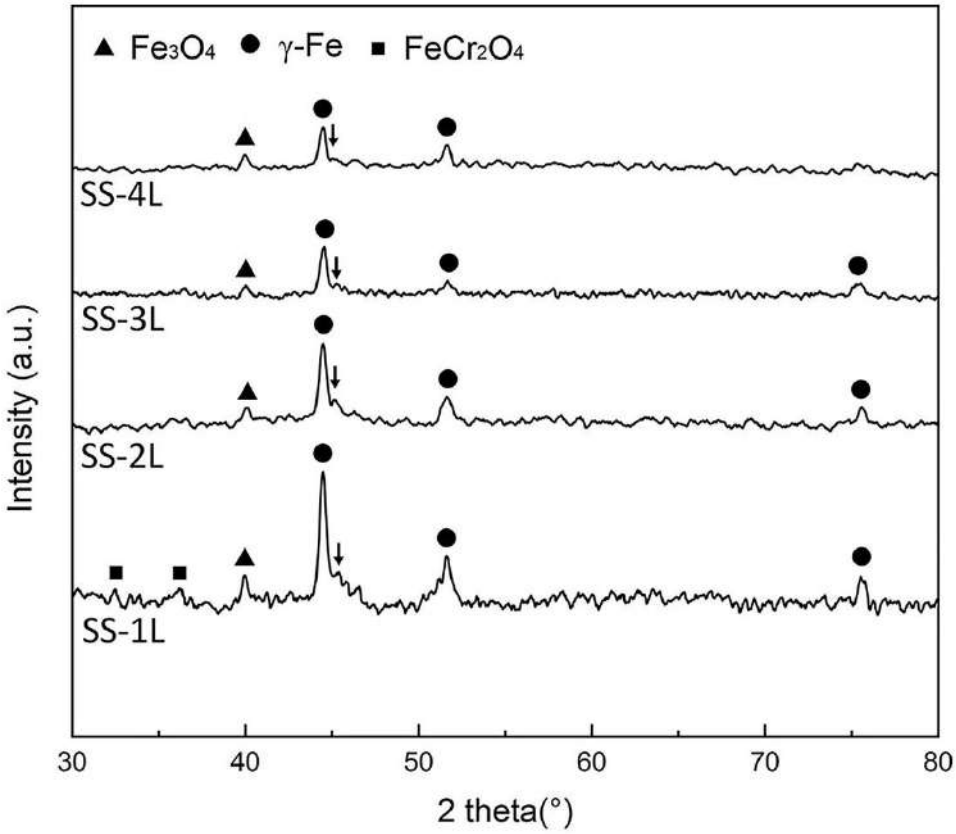


Figure 4.13 XRD diffraction patterns for SS-1L, SS-2L, SS-3L and SS-4L

The metastable γ-Fe phase peak presents the highest relative intensity for all the samples. The intensity of austenite is reduced with increasing the number of layers. The more layers are deposited, the more the coating is exposed to heat during spraying and so, the more heat treatment is produced which enhance the γ-Fe phase transformation into α-Fe phase [4.24]

(indicated by arrows) that is mostly martensite rather than ferrite due to the rapid cooling during spraying [4.25]. The α-Fe is not clearly detected in the diffraction. Another reason behind the γ-Fe phase transformation is the oxidation of the alloying elements such as Cr and Ni that reduce the stability of austenite [4.24]. In addition, Fe_3O_4 (magnetite) can be observed in all the four coatings and $FeCr_2O_4$ (chromite spinel) in SS-1L.

Figure 4.14 shows the SEM surface morphologies with magnified regions for: (a) SS-1L, (b) SS-2L, (c) SS-3L and (d) SS-4L. All the four coatings present the typical arc spray splats that are bonded to each other, suggesting that the most of the sprayed particles were well melted before their impact with the substrate/previous layers surface [4.4]. Thereafter, the coatings cooling down are occurred due to the heat exchange with the room temperature. The shape and the size of the obtained splats increase with the number of layers.

In fact, the splats size depends on the temperature of the sprayed particles during their deformation and solidification, which have a direct relation to the substrate/previous layers surface temperature. When the substrate/previous layers surface temperature is high, the necessary time for the solidification of the splats increases, and so does the time for the particles deformation [4.1], which gives wider splats. With higher splats size, the number of the inter-splats boundaries which are responsible for decreasing the coating cohesive strength will be lower, resulting in a more compact coating and thereby better surface properties are expected for the coatings with higher number of layers.

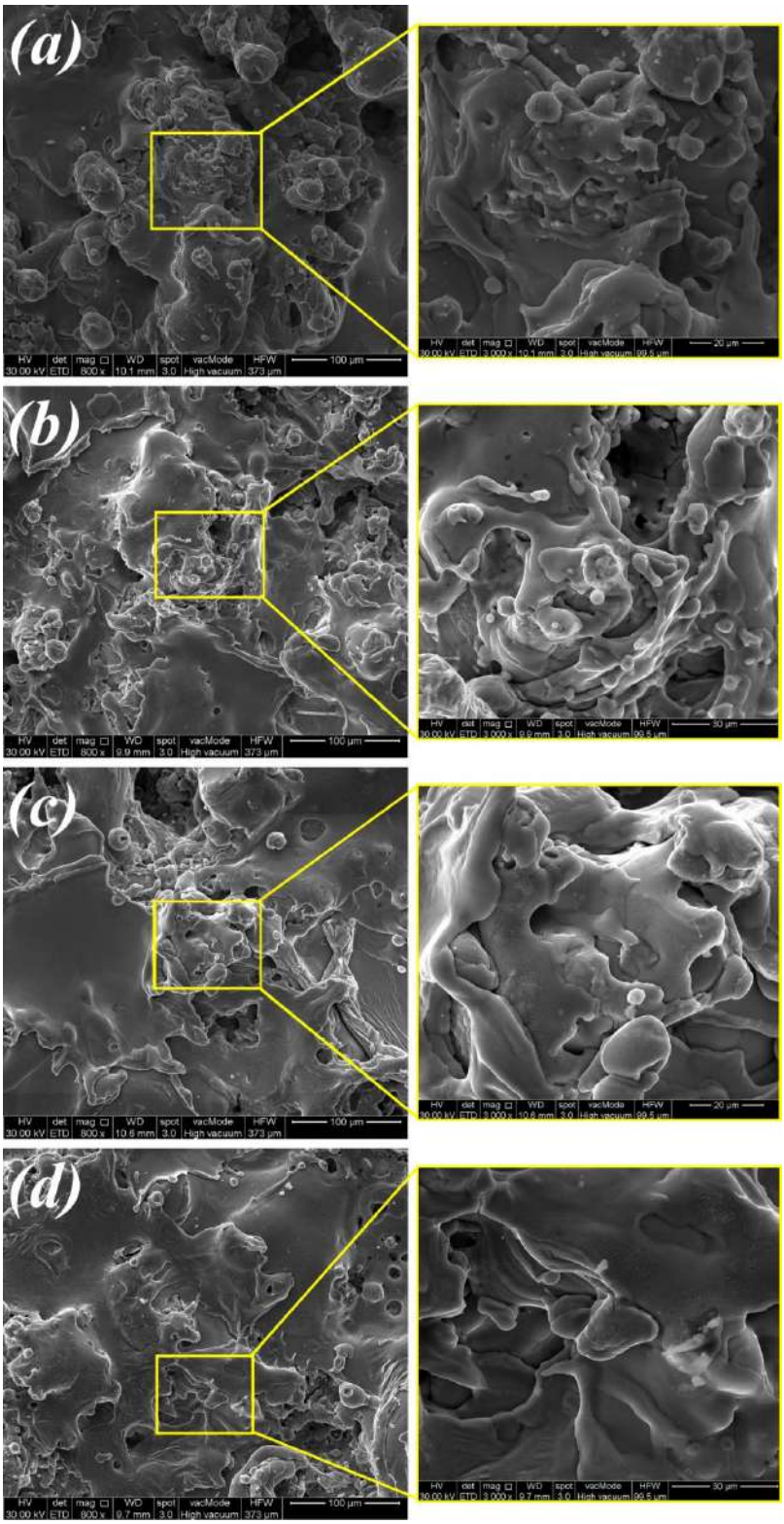


Figure 4.14 SEM top view images with magnifications for: (a) SS-1L, (b) SS-2L, (c) SS-3L and (d) SS-4L

Figure 4.15 shows the SEM cross-section images for SS-1L, SS-2L, SS-3L and SS-4L respectively. The coatings thicknesses are 434.6±2.9 μm for SS-1L, 554.8±1.9 μm for SS-2L, 676.4±3.9 μm for SS-3L and 799.4±0.4 μm for SS-4L. In **Figure 4.15**, the elemental composition of the coatings interfaces with the substrates are obtained by the EDS analysis. The different coatings present a high amount of oxides that is ranged from 12.68 wt.% for SS-3L, 13.16 wt.% for SS-2L, 14.52 wt.% for SS-1L and finally 29.03 wt.% for SS-4L. Such high oxides compositions are due to the high spraying temperature of the TWAS process [4.25, 4.26]. Mainly, there are two types of the oxides that can exist in the thermal sprayed multilayers coatings: the interlayer oxides that exist between each deposited layer, and the oxides exist around the splats and the semi-melted particles [4.27]. The interlayer oxides are obtained after the interaction of each hot deposited layer with the surrounding oxygen in the air, leading to the formation of a protective oxide film before the deposition of the next layer. The rapidity of the oxide layers formation is related to the high temperature of the arc. Nevertheless, the oxides that are formed around the splats and the semi-melted particles are originated from the interactions of the molten stainless steel particles with the oxygen in the air during the inflight time with high temperatures.

SS-4L coating has the highest oxides amount because it is exposed to the quenching effect with every deposited layer due to the rapid cooling down. As a consequence, the oxides existing between layers are defused through the coating pores into the interface, and thereby, higher oxides amount are detected [4.28].

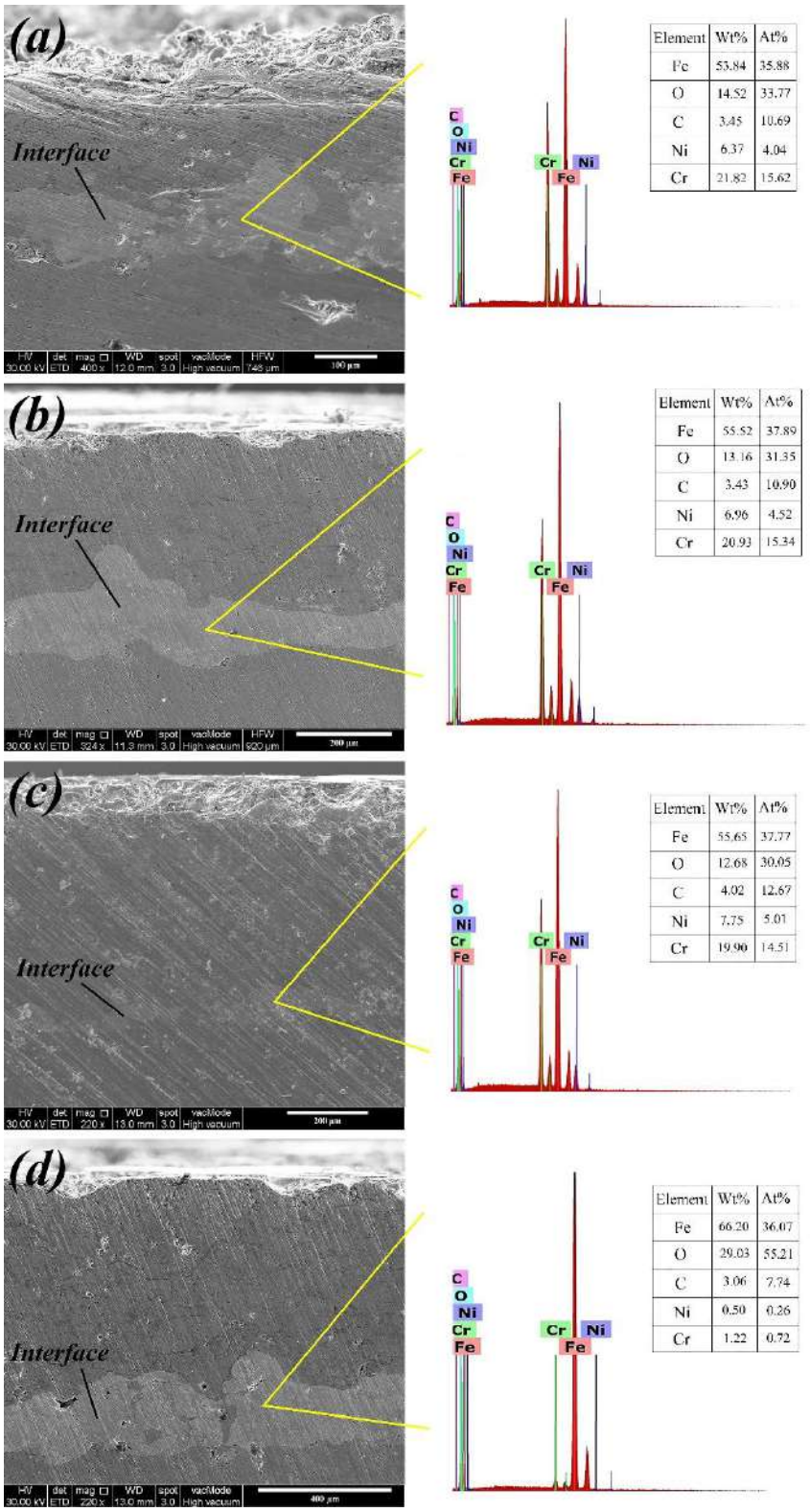


Figure 4.15 SEM cross-section images with the EDS analysis for: (a) SS-1L, (b) SS-2L, (c) SS-3L, (d) SS-4L

Figure 4.16 shows the roughness arithmetic mean (Ra) for SS-1L, SS-2L, SS-3L and SS-4L. It can be seen that the Ra values are reduced with the number of layers, from 209.0±1.2 nm for the 1 layer coating to 182±1.5 nm with 2 layers, 174.1±1.5 nm with 3 layers and 171.7±1.6 nm with 4 layers which confirms the relation between the splats sizes and the roughness suggested in the first optimization above.



Figure 4.16 Roughness analysis results for: SS-1L, SS-2L, SS-3L and SS-4L

4.2.3. Mechanical results for the second optimization

Figure 4.17 shows the nanohardness and the Vickers hardness measurements results for: SS-1L, SS-2L, SS-3L and SS-4L. The hardness increases when increasing the number of layers from 1 to 4. SS-4L coating present the highest hardness with H=344.4±4.9 HV_{10} and nanohardness of H_N=13.9±1.9 GPa, followed by SS-3L with hardness of H=246.1±4.6 HV_{10} and nanohardness of H_N=10.7±1.7 GPa, while SS-2L and SS-1L have the lowest hardness

values of H=222.3±5.4 HV_{10}, H_N=8.8±0.6 GPa and H=204.9±6.8 HV_{10}, H_N=8.7±0.4 GPa respectively.

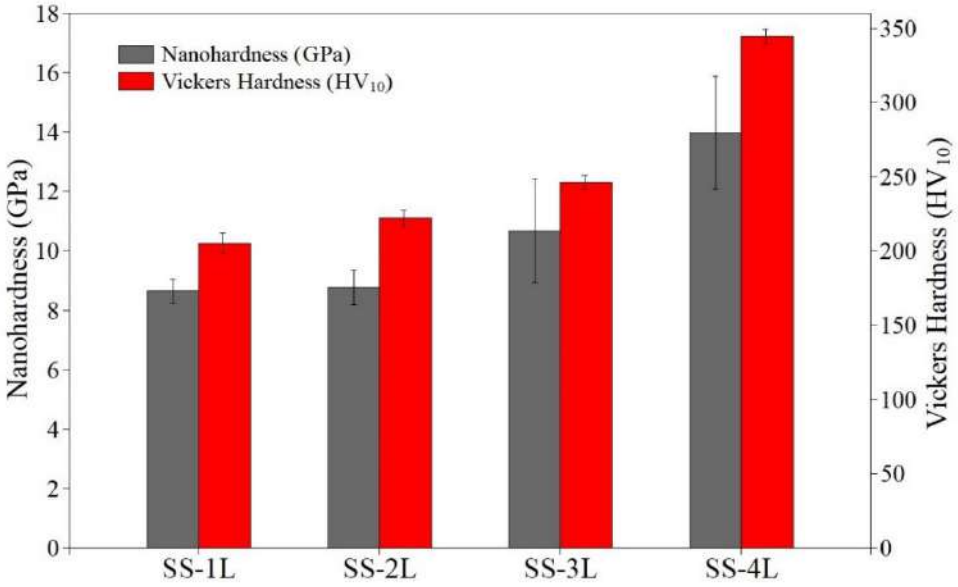


Figure 4.17 Hardness measurement results for: SS-1L, SS-2L, SS-3L and SS-4L

Similar trend of the hardness variation with the number of layers was reported previously by [4.27, 4.14] for 316L stainless steel coatings deposited by HVOF thermal spray with 328 $HV_{0.1}$ for the 1 layer coating, 349 $HV_{0.1}$ for the 2 layers coating, 392 $HV_{0.1}$ for the 3 layers coating and 433 $HV_{0.1}$ for the 4 layers coating.

The increasing in the hardness of the multilayers coatings and especially for that of SS-4L is due to their higher compactness [4.15], and this is related to the effect of the layers pile up on the top of the others, which deforms the previously deposited layers, reducing their porosity and increasing their hardness [4.27]. The quenching effect that increases with increasing the number of layers due to the multilayer cooling down to room temperature can induce the generation of the quenching stresses that increase the hardness of the coatings [4.27]. Also, the difference in the TECs between every layer and the previous layers/substrate prompts the

initiation of the thermal stresses which have a high effect on increasing the hardness of the coatings [4.2]. In addition, with the deposition of each layer, the sprayed particles impact on the previous layers, causing plastic deformation and thereby penning stresses will be generated which contribute on the hardness increasing [4.27].

Table 4.6 shows the nanoindentation test results for SS-1L, SS-2L, SS-3L and SS-4L.

Samples	**H (GPa)**	**E (GPa)**	**H^3/E^2 (GPa)**
SS-1L	8.7±0.4	223.3±13.3	0.013
SS-2L	8.8±0.6	163.3±6.1	0.026
SS-3L	10.7±1.7	212.4±5.1	0.027
SS-4L	13.9±1.9	184.8±5.4	0.079

Table 4.6 Nanoindentation test results for: SS-1L, SS-2L, SS-3L and SS-4L

SS-4L has the highest H^3/E^2 value of 0.079 GPa followed by SS-3L with 0.027 GPa indicating a better wear resistance [4.16].

Figure 4.18 represent the typical nanoindentation load-displacement curves for the four coatings, where the area between the loading and the unloading curves defines the plastic deformation work W_P. According to the curves, the plastic deformation work of SS-4L is the lowest followed by SS-3L, SS-2L and finally SS-1L that reveals a high plastic deformation work. From the nanoindentation load-displacement curves, the elastic recoveries of all the four coatings are calculated and their values are 60.39% for SS-4L, 27.53% for SS-3L, 26.06% for SS-2L and 15.34% for SS-1L.

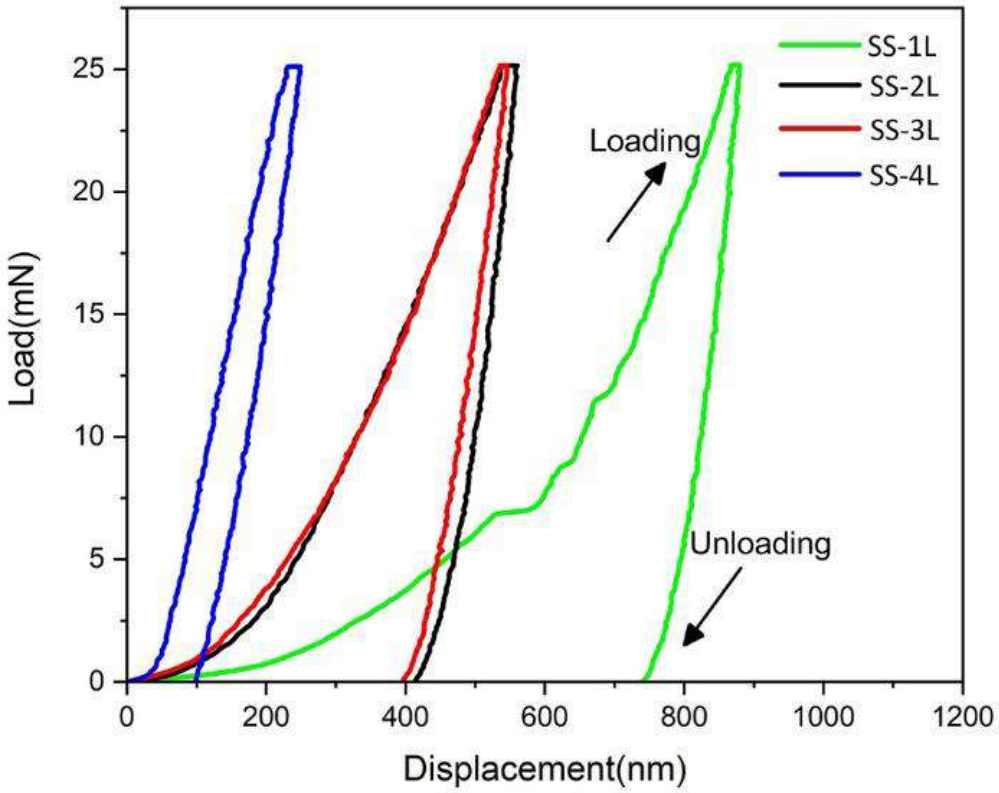


Figure 4.18 Typical nanoindentation curves for: SS-1L, SS-2L, SS-3L and SS-4L

4.2.4. Tribological results for the second optimization

Figure 4.19 presents COF variation as a function of the friction path for: SS-1L, SS-2L, SS-3L and SS-4L. The friction curves for all the coatings exhibits two stages. The first stage is characterized by a sharp increase of COFs until they reach their peak values of μ≈0.73 at 60 m for SS-1L, μ≈0.80 at 72 m for SS-2L, μ≈0.66 at 11 m for SS-3L and μ≈0.70 at 21 m for SS-4L. The second stage starts by a decreasing trend followed by stabilization at COFs of μ≈0.51 for SS-1L, μ≈0.60 for SS-2L, μ≈0.50 for SS-3L and μ≈0.48 for SS-4L.

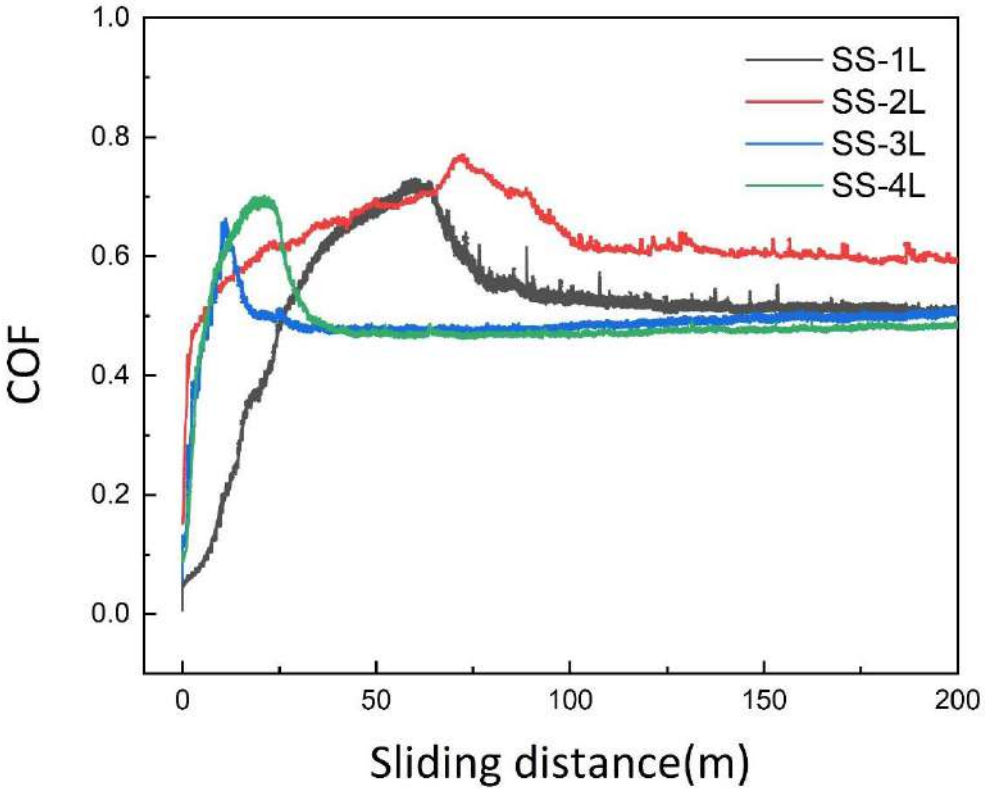


Figure 4.19 COF variations as function of the sliding distance for: SS-1L, SS-2L, SS-3L and SS-4L

Table 4.7 presents the principal tribological results for the different coatings.

Samples	**SS-1L**	**SS-2L**	**SS-3L**	**SS-4L**
COF	0.52±0.15	0.63±0.14	0.49±0.06	0.49±0.07
k x10^{-4} (mm^3/N·m)	2.63±0.06	1.45±0.06	0.97±0.08	0.54±0.03

Table 4.7 Tribological test results for: SS-1L, SS-2L, SS-3L and SS-4L

SS-3L and SS-4L have the lowest COFs of μ=0.49±0.06 and μ=0.49±0.07 respectively, while those of SS-1L and SS-2L are respectively μ=0.52±0.15 and μ=0.63±0.14. SS-4L has also the lowest wear rates of k=0.54±0.03·10^{-4} mm^3/ N·m. The low wear rate measurement of SS-4L can be related to its high hardness and low COF in accordance with the Archard wear theory

[4.29]. The high amount of oxides in SS-4L coating that can play the role of self-lubrication, is another reason for the low wear rate.

Figure 4.20 shows the wear tracks 3D profiles for: SS-1L, SS-2L, SS-3L and SS-4L. SS-4L coating has the shallowest wear depth of D_P=0.012 mm, while that of SS-2L is the deepest with D_P=0.126 mm. SS-1L and SS-3L have respectively wear depths of: D_P=0.082 mm and D_P=0.111 mm. Wear track width measurements reveal that SS-3L presents the narrowest wear tracks with w=0.055 mm followed by SS-2L with w=0.072 mm, while those of SS-1L and SS-4L are respectively: w=0.197 mm, w=0.273 mm and w=1.41 mm.

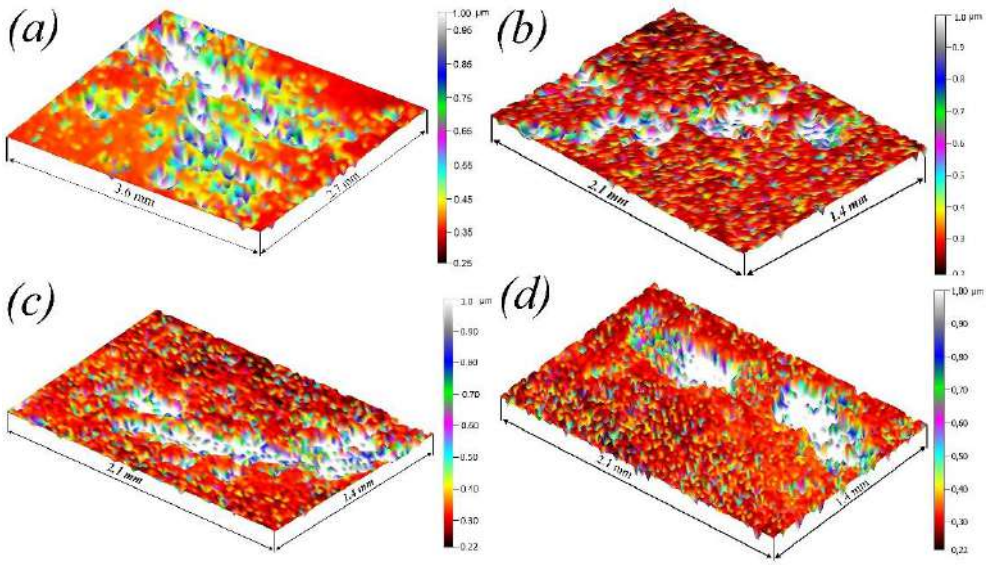


Figure 4.20 AFM 3D images of wear tracks profiles for: (a) SS-1L, (b) SS-2L, (c) SS-3L and (d) SS-4L

Figure 4.21 shows the wear tracks observations for: SS-1L, SS-2L, SS-3L and SS-4L. Deep grooves in the sliding direction which are the signs of the abrasive wear can be clearly seen in all the coatings, except for SS-1L that is featured with shallower and almost unnoticeable grooves. Scaling pits in the wear direction can be observed also in all the coatings, suggesting that all of them were subjected also to the delamination wear. Less scaling pits can be observed in SS-4L.

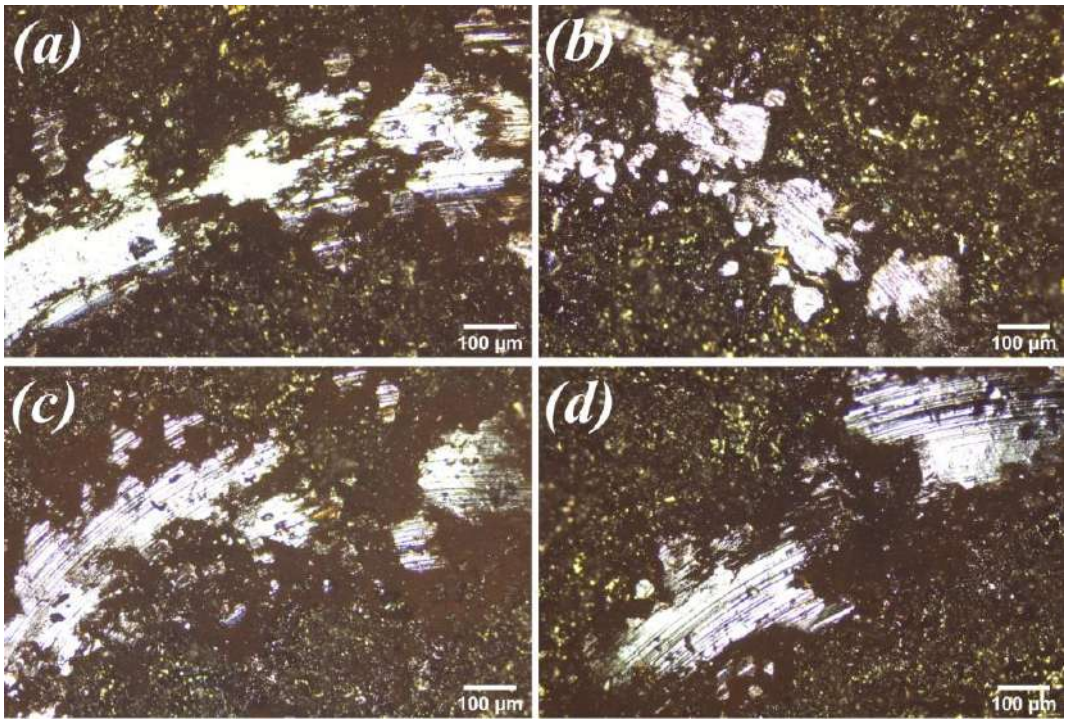


Figure 4.21 Wear tracks observations for: (a) SS-1L, (b) SS-2L, (c) SS-3L and (d) SS-4L

For SS-1L and due to its high amount of inter-splats boundaries because of its small splats sizes as observed in **Figure 4.14**, which are responsible for decreasing the coating cohesive strength, splats can be easily separated [4.30], resulting in more delamination and less abrasion. With increasing the number of layers from 2 to 4, the splats sizes increase and the coatings cohesive strength becomes higher and thereby more compact coatings are obtained and a main wear mode transition takes place from delamination wear to abrasive wear. For SS-4L that is characterized by wider splats, the cracks propagation during the test is less [4.9], and the wear mechanism will be mainly abrasive wear and only abrasion grooves with some tiny scaling pits can be seen on the worn surface. The high scaling pits roughs the worn surfaces which leads to the formation of local asperities that increase the wear rate [4.9]. This can be considered as another explanation of the decreased wear rate when increasing the coatings number of layers.

4.2.5. Electrochemical results for the second optimization

Figure 4.22 presents the polarization curves of: SS-1L, SS-2L, SS-3L and SS-4L.

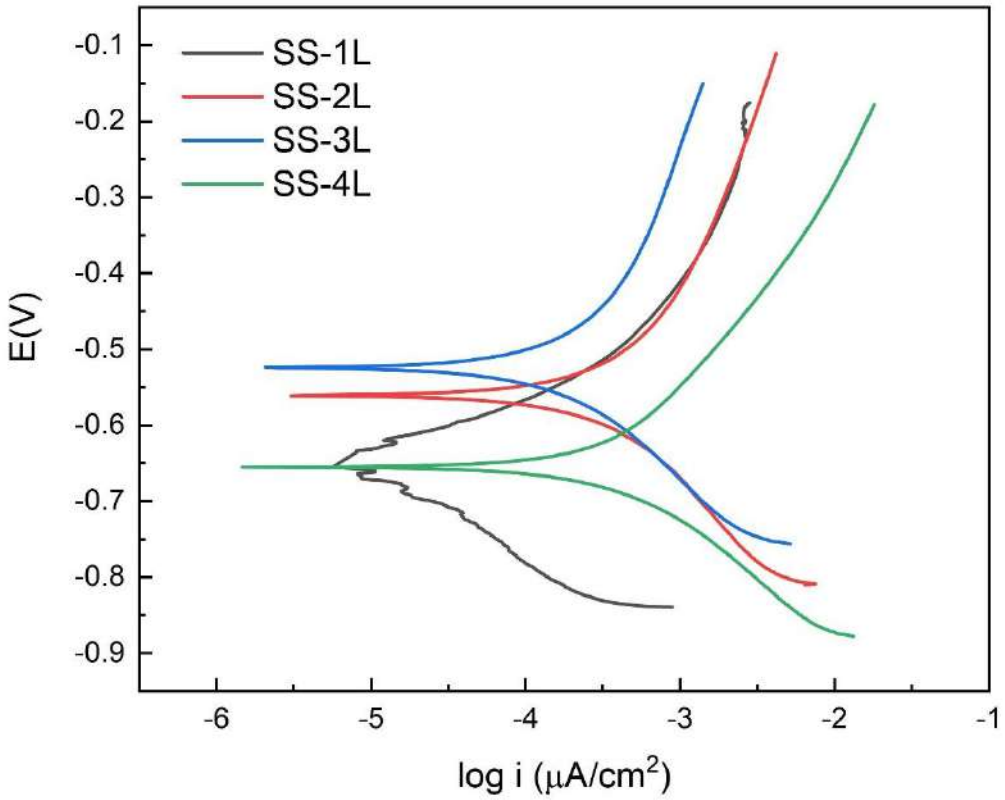


Figure 4.22 Polarization curves of: SS-1L, SS-2L, SS-3L and SS-4L

E_{OC}, i_{corr} and C_R of the coatings are listed in **Table 4.8**. i_{corr} is related to the corrosion kinetics [4.27], thereby, coatings with lower i_{corr} have more uniform corrosion. i_{corr} is also known as the most accurate result for comparing the corrosion behaviour of metallic materials [4.31]. SS-2L presents the lowest corrosion current density of i_{corr}=1.47 μA cm^{-2} followed by SS-3L with i_{corr}=2.08 μA cm^{-2} and then SS-4L with i_{corr}=3.03 μA cm^{-2}. All those three coatings have very low i_{corr} in comparison to SS-1L with i_{corr}=30.02 μA cm^{-2}. E_{OC} on the other side is related to the thermodynamic characteristics of the reaction system [4.27], and the coatings tendency to form metal ions and corrosion process [4.32].

Coatings	C_R (mpy)	E_{OC} (V)	i_{corr} (µA/cm^2)
SS-1L	13.03	-0.62	30.02
SS-2L	0.09	-0.66	1.47
SS-3L	0.13	-0.65	2.08
SS-4L	0.19	-0.52	3.03

Table 4.8 Electrochemical test results for: SS-1L, SS-2L, SS-3L and SS-4L

SS-4L presents the highest E_{OC} than all the other coatings (E_{OC}=-0.52 V) while it has not the lowest i_{corr}. This is an indication of a different corrosion mechanism [4.15]. SS-4L contains more oxides and thereby more burnout of alloying elements which leads to chromium reduction in the locations where the corrosion is occurred more strongly, and as a result increasing its current density [4.23]. In the contrary, with increasing the number of layers, the coating microstructure become denser with low porosity, resulting in a less ability of electrolyte to penetrate through the coating pores to reach and corrode the substrate surface and to form a galvanic couple between the coating (cathode) and the substrate (anode) and as a consequence, a higher E_{OC} can be obtained. SS-2L and SS-3L present very interesting corrosion rates with respectively C_R=0.09 mpy and C_R=0.13 mpy which are lower by more than 8 times and 6 times respectively than that of the massive stainless steel 304-SSB. Evidence of their effectiveness as corrosion protective coatings.

4.2.6. The performance factors $K_{P2(SS\text{-}1L)}$, $K_{P2(SS\text{-}2L)}$, $K_{P2(SS\text{-}3L)}$, $K_{P2(SS\text{-}4L)}$

A qualitative comparison between the different coatings according to their hardness, elastic modulus, friction coefficient, wear rate and corrosion rate is given in the polar diagram shown

in **Figure 4.23**. The diagram reveals that SS-1L coating has high elastic modulus, wear rate and corrosion rate while having low hardness value. In the contrary, SS-4L displays low elastic modulus, friction coefficient, wear rate and corrosion rate while having high hardness value, suggesting that SS-4L coating has desirable values comparing with the rest of the coatings.

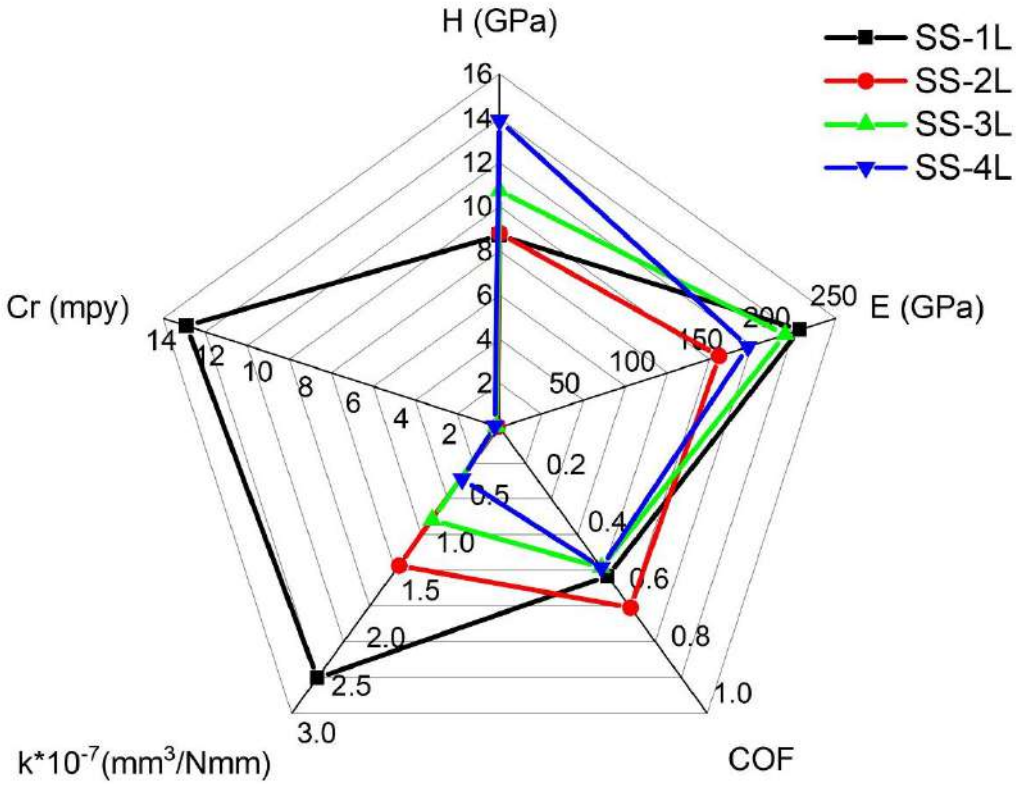


Figure 4.23 Polar diagrams providing a qualitative comparison of the coatings: SS-1L, SS-2L, SS-3L and SS-4L

The above qualitative assessment can be confirmed by calculating the performance factors of the four coatings using the equation (3.3) to choose the best coating and so the optimal number of layers.

The performance factor of SS-1L coating was already calculated in the previous sub-chapter and it has as value:

$$K_{P2(SS-1L)} = K_{P1(304L-SSC)} = 4.88 \cdot 10^9\ N^2 \cdot year/mm^5$$

The performance factors of SS-2L, SS-3L and SS-4L are respectively: $K_{P2(SS-2L)}$, $K_{P2(SS-3L)}$ and $K_{P2(SS-4L)}$, and they can be calculated using respectively the equations: (4.4), (4.5) and (4.6), given as the following:

$$K_{P2(SS-2L)} = \frac{H_{(SS-2L)}}{C_{R(SS-2L)} \cdot \mu_{(SS-2L)} \cdot k_{(SS-2L)}}\ [N^2 \cdot year/mm^5] \quad (4.4)$$

$$K_{p2(SSC-3L)} = \frac{H_{(SS-3L)}}{C_{R(SS-3L)} \cdot \mu_{(SS-3L)} \cdot k_{(SS-3L)}}\ [N^2 \cdot year/mm^5] \quad (4.5)$$

$$K_{p2(SSC-4L)} = \frac{H_{(SS-4L)}}{C_{R(SS-4L)} \cdot \mu_{(SS-4L)} \cdot k_{(SS-4L)}}\ [N^2 \cdot year/mm^5] \quad (4.6)$$

The different factors values are given in **Table 4.9**.

Coatings	**H (N/mm^2)**	**C_R (mpy)**	**COF**	**k (mm^3/N·mm)**
SS-2L	$8.8 \cdot 10^3$	0.09	0.63	$1.45 \cdot 10^{-7}$
SS-3L	$10.7 \cdot 10^3$	0.13	0.49	$0.97 \cdot 10^{-7}$
SS-4L	$13.9 \cdot 10^3$	0.19	0.49	$0.54 \cdot 10^{-7}$

Table 4.9 Factors values of: SS-2L, SS-3L and SS-4L

The calculated factors of performance are:

$$K_{P2(SS-2L)}\ (H, C_r, \mu, k) = 107.04 \cdot 10^9\ N^2 \cdot year/mm^5$$

$$K_{P2(SS-3L)}\ (H, C_r, \mu, k) = 173.17 \cdot 10^{10}\ N^2 \cdot year/mm^5$$

$$K_{P2(SS-4L)}\ (H, C_r, \mu, k) = 276.48 \cdot 10^{10}\ N^2 \cdot year/mm^5$$

SS-4L has the highest factor of performance then all the rest of the coatings because it has the highest hardness and wear rate and the lowest friction coefficient and relatively a low

corrosion rate. The three coatings have higher factor of performance than the massive stainless steel 304-SSB that has as value: $K_{P1(304\text{-}SSB)}$ =5.04·10^9 N^2·year/mm^5.

From the above results, SS-4L coating will be optimized more in the next sub-chapter using the post-spray annealing. PIII nitruration treatment and W-Ti-N thin film will be applied on the optimal SSC later in the next chapters.

4.3. Effect of annealing temperature on the surface behaviour of four layered SSC

4.3.1. Introduction to the third optimization

In the previous two sub-chapters, 304L stainless steel multilayer coating with 4 layers was selected according to its surface behaviour (H, COF, k and C_R). In the present sub-chapter, a third optimization for that coating will be applied using a post-spraying annealing treatment. Three different annealing temperatures were chosen according to the literature. Those temperatures are: 800°C, 1000°C and 1100°C. To find more about the effect of post-spraying annealing treatment on the properties of SSCs, see chapter 1, section 3. After obtaining the different results, performance factors K_{P3} for the different coatings will be calculated to choose the optimal annealing temperature that can enhance the 304L multilayer coating properties.

The coated samples were subjected to annealing post-treatment in OTF-1200X-II-UL vacuum split tube furnace (see chapter 3) with 10^{-5} MPa (8·10^{-2} torr) of vacuum. The annealing parameters are listed in **Table 4.10**. All the samples were furnace cooled. SS-4L will be referred to by SS-0.

coating reference	Temperature (°C)	Time (h)	Heating/Cooling rate (°C/min)
SS-0 (as-deposited)	N/A	N/A	N/A
SS-800	800	4	10
SS-1000	1000	4	10
SS-1100	1100	4	10

Table 4.10 Annealing parameters for the different coatings

The characterization equipment and parameters are the same to those of the previous sub-chapters. Detailed lists of the equipment are given also in chapter 3.

4.3.2. Microstructural results for the third optimization

Figure 4.24 presents the cross-section images of the as-sprayed and the annealed coatings observed by SEM. The microstructure of SS-0 consists of lamellar splats (a) interspersed with semi-molten particles (b), cracks (c) and porosity (d). The origin of this porosity is the gas trapping during the solidification process of the coating and the imperfect packing of the droplets of the molten material [4.8]. Compared with the SS-0 coating, the annealed coatings SS-800, SS-1000 and SS-1100 are very dense, smooth and look more like a bulk material than sprayed coatings. The bright areas are full of oxides and they represent the coatings interfaces that are clearly visible for the SS-0, those bright areas become more unclear with increasing the annealing temperature up to 1100°C for the SS-1100 coating, where the coating cannot be distinguished from the substrate without using the EDS analysis. The above observations indicate that oxides diffusions from the interface to the surface are taking place during the vacuum annealing [4.33]. The coatings thicknesses measurements are: 799.4±0.4 µm for SS-0, 767.8±4.6 µm for SS-800, 662.5±8.5 µm for SS-1000 and 652.2±1.9 µm for SS-1100.

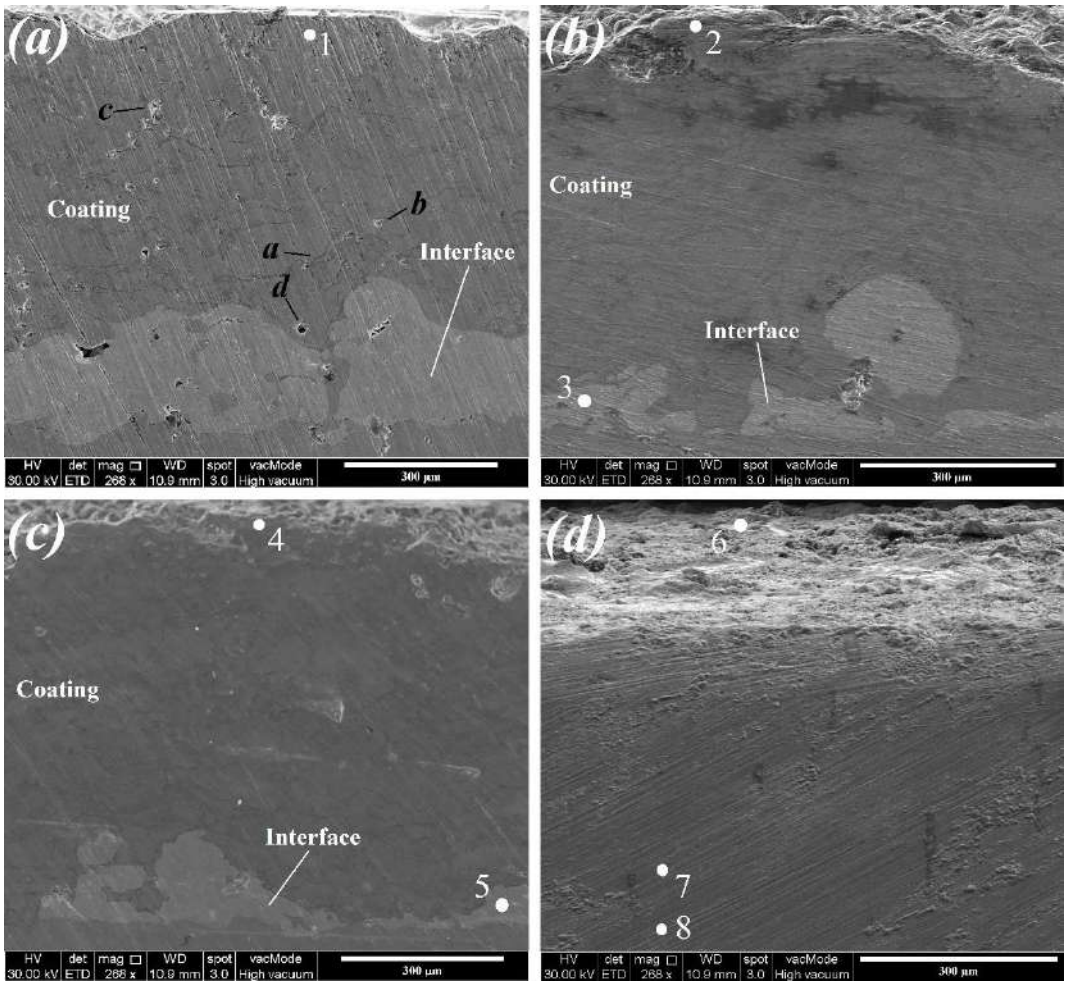


Figure 4.24 SEM cross-section images for: (a) SS-0, (b) SS-800, (c) SS-1000, (d) SS-1100

Figure 4.25 shows the EDS analysis results of the different locations indicated in **Figure 4.24**. For SS-800 coating, and after vacuum annealing with 800°C, the coating's chromium is oxidized into the favorable Cr_2O_3 that can cover the coating pores [4.28], therefore, the amount of the diffused oxides into the surface will decrease drastically and the detected surface oxides falls from 29.03 wt.% to 11.70 wt.% in the coating surface at location 2. Approximately, the same oxides amount is detected in the coating/substrate interface in location 3, with Ni and Cr composition of 7.79 and 17.87 respectively that are similar to their amount in the 304L stainless steel wire material. At higher annealing temperatures in the case of SS-1000 and SS-1100 coatings, the formation of chromite spinel $FeCr_2O_4$ from the Cr_2O_3

is taking place [4.28], leading to the diffusion of more oxides into the coatings surface in order to form more $FeCr_2O_4$, and the detected oxides in both coatings is rose again into 23.58 wt.% for SS-1000 and 24.51 wt.% for SS-1100. As it was mentioned above, for SS-1100, it is impossible to distinguish the coating from the substrate without the EDS analysis. In location 8, the absence of Cr and Ni is an indication of the carbon steel substrate. SS-1100 thickness was calculated in the medium between the locations 7 and 8.

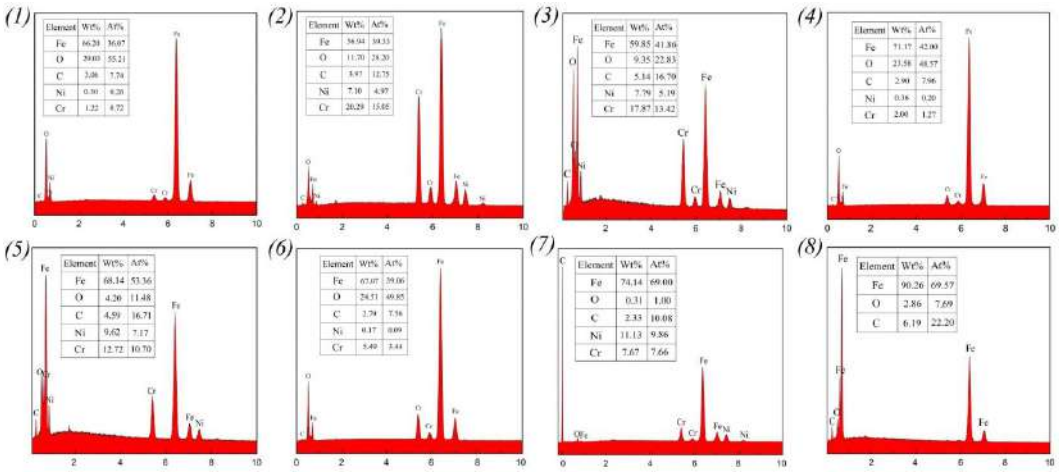


Figure 4.25 EDS analysis results for: (1) SS-0, (2,3) SS-800, (4,5) SS-1000 and (6,7,8) SS-1100

Figure 4.26 shows the XRD patterns of the coatings. Austenite (γ-Fe) peak has a low intensity for all the coatings which reveals the metastable state of this phase in the stainless steel coatings [4.25], in the contrary, ferrite (α-Fe) presents a higher intensity, especially in SS-800, suggesting a phase transformation from austenite into ferrite [4.16]. Generally, steels at equilibrium are made of ferrite more than any other phase [4.25], thereby, the more the coating is consist of ferrite phase, the more it is in the equilibrium state. In addition, magnetite (Fe_3O_4) oxides peaks are observed in all the four coatings showing the stable state of that oxide even after annealing. In addition, Cr_2O_3 can be observed in the annealed coatings, $FeCr_2O_4$ in SS-1100 and Fe-Cr in SS-800. Wuestite (FeO) oxide that is observed in SS-800

coating only, transforms completely into magnetite oxide after annealing the coating at higher temperatures, following the reaction [4.25]:

$$FeO \rightarrow Fe_3O_4 + F_e$$

According to that reaction, more stable ferrite phase will be obtained in SS-1000 and SS-1100.

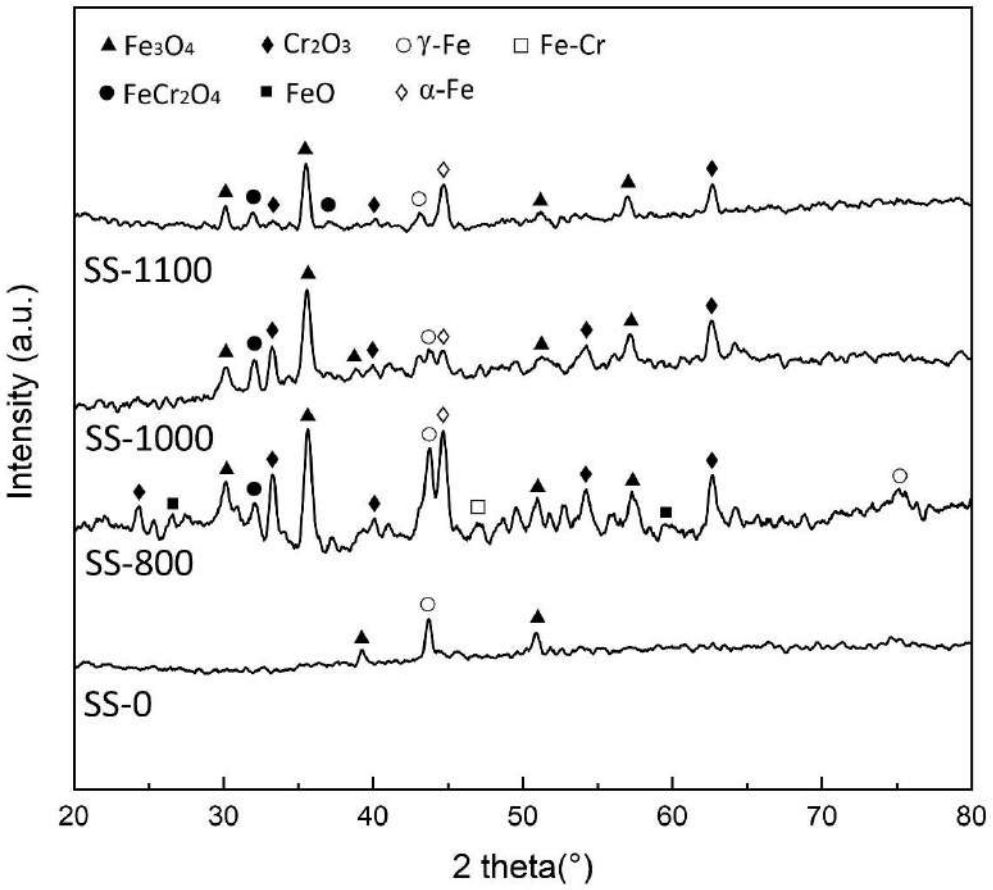


Figure 4.26 XRD diffraction patterns for: SS-0, SS-800, SS-1000 and SS-1100

Figure 4.27 shows SEM surface observations with magnified regions for: (a) SS-0, (b) SS-800, (c) SS-1000 and (d) SS-1100.

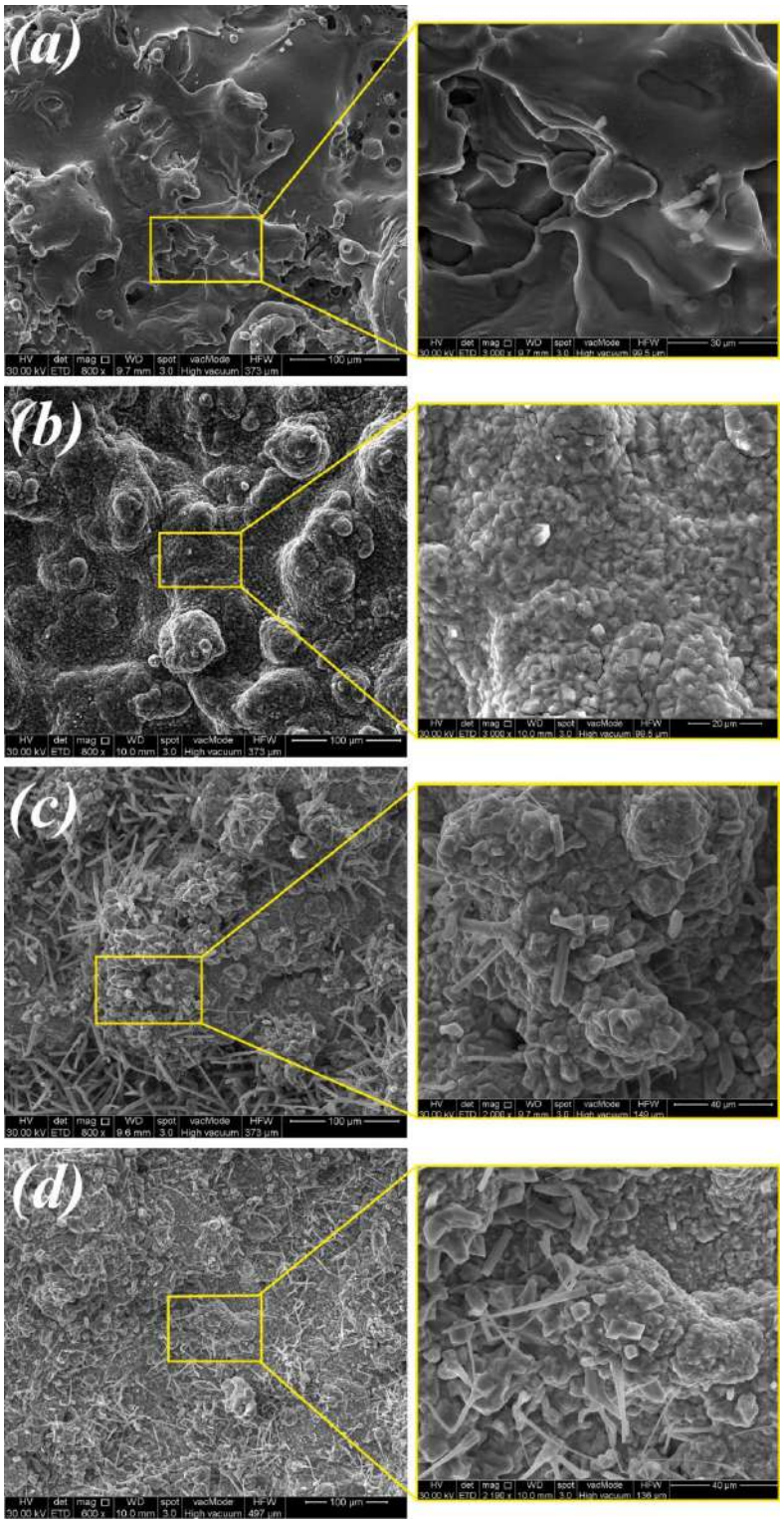


Figure 4.27 SEM top view images for: (a) SS-0, (b) SS-800, (c) SS-1000 and (d) SS-1100

For SS-0 coating, fine splats are obtained, suggesting that the most of the sprayed particles were well melted before impacting the substrate/previous layers surfaces [4.25]. After annealing at the different temperatures, the coatings microstructure is obviously changed. SS-800 coating exhibits a dense microstructure with no visible pores and defects. SS-800 is formed by dot-like shapes that represent the Fe_3O_4 oxide according to [4.28].

It was reported also before [4.34] that the annealed Fe-based coatings at 750°C have similar surface aspect and they contain high Cr_2O_3 amount, the SEM images correlated well with the above suggestion about the formation of the favorable Cr_2O_3 in the SS-800 coating. SS-1000 coating surface revealed flakes and needle-like shapes microstructures which are the common forms of the Fe_2O_3 and the $FeCr_2O_4$ oxides [4.28], along with some dot-like shapes, while SS-1100 coating showed a surface full of needle-like shapes.

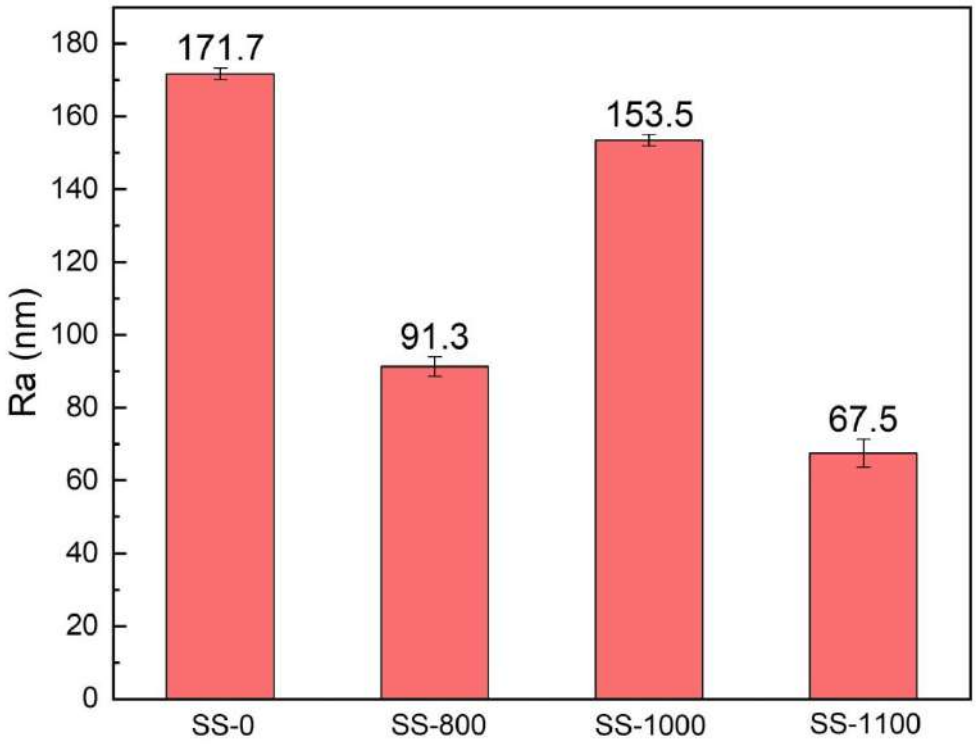


Figure 4.28 Roughness analysis results for: SS-0, SS-800, SS-1000 and SS-1100

Figure 4.28 shows the roughness arithmetic mean (Ra) for SS-0, SS-800, SS-1000 and SS-1100. It can be seen that SS-1100 presents the lowest roughness with Ra=67.5±3.8 nm suggesting a denser and a lubricating surface. SS-800 presents also a low roughness with Ra=91.3±2.7 nm. In the contrary, SS-0 and SS-1000 have the roughest surfaces with Ra=171.7±1.6 nm and Ra=153.5±1.6 nm.

4.3.3. Mechanical results of the third optimization

Figure 4.29 shows the nanohardness and the Vickers hardness measurements results for: SS-0, SS-800, SS-1000 and SS-1100. SS-0 has the highest hardness with H=344.4±4.9 HV_{10} and nanohardness of H_N=13.9±1.9 GPa.

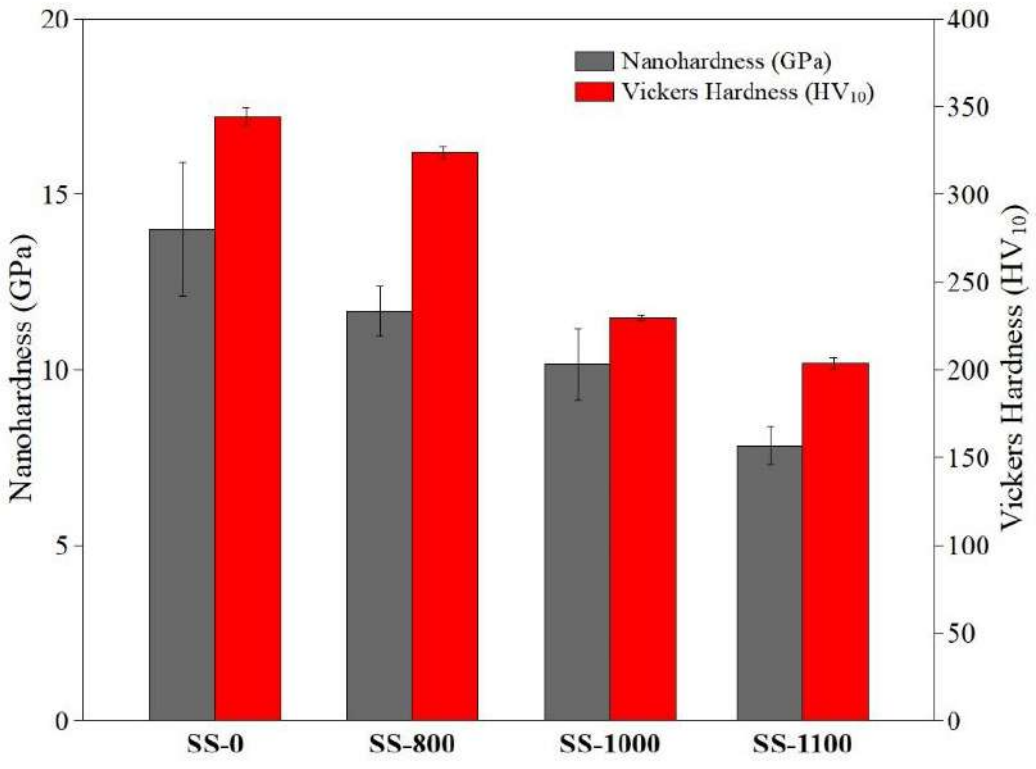


Figure 4.29 Hardness measurement results for: SS-0, SS-800, SS-1000 and SS-1100

The high hardness of the as-sprayed coating is related to the generation of the residual stresses and the strain-hardening effect during the coating deposition [4.35]. In general, there are three

forms of induced residual stresses that can be generated in the thermal sprayed coatings: the quenching stresses, the thermal stresses and the phase transformation stresses. The quenching stresses occur generally during the coating deposition, when the coating droplets hit the surface of the substrate or the previous sprayed layers and quench them to their high temperature in milliseconds leading to the generation of thermal contractions between the coating splats. The thermal stresses are generated after the coating cooling down to the ambient temperature, because of the difference in the TECs between the coating and the substrate [4.9]. In the case of SS-0, the main induced residual stress form is the quenching stress that can be generated after the impact of the molten particles on the surface of the previous deposited layers with high temperature of around 5000°C and quench them to the ambient temperature.

When the coatings are annealed, their hardness decrease with the increased temperature with H=324.0±3.5 HV_{10} and nanohardness of H_N=11.7±0.7 GPa at 800°C, H=229.9±1.7 HV_{10} and nanohardness of H_N=10.2±1.0 GPa at 1000°C and finally H=203.7±3.2 HV_{10} and nanohardness of H_N=7.8±0.5 GPa at 1100°C. The softening of the hardness after annealing can be related to the γ-Fe phase transformation into α-Fe, since it is well known that γ-Fe is harder than α-Fe [4.8]. In addition, this reduction in the hardness is due to the elimination of the residual stresses [4.36] and of the persistent dislocation loops that are formed during the arc spraying [4.35]. At 1100°C, the measured hardness is close to that of the massive 304 bulk material 304-SSB ((H=201.3±1.2 HV_{10} and H_N=6.7±0.2 GPa).), this result confirms the assumption reported by [4.37] who recommends a temperature range of 1010-1120°C for the 304L stainless steel coatings to have surface properties close to those of the bulk material. The softening effect of the annealed coatings has benefit in avoiding micro-cracks initiation by decreasing internal stresses in the lamellar structure [4.38].

Table 4.11 shows the nanoindentation test results for: SS-0, SS-800, SS-1000 and SS-1100.

Coating	H (GPa)	E (GPa)	H^3/E^2 (GPa)
SS-0	13.9±1.9	184.8±5.4	0.079
SS-800	11.7±0.7	182.6±2.8	0.048
SS-1000	10.2±1.0	171.5±6.0	0.036
SS-1100	7.8±0.5	155.7±6.7	0.020

Table 4.11 Nanoindentation test results for: SS-0, SS-800, SS-1000 and SS-1100

The elastic modulus (E) values decrease when increasing the annealing temperature from E=184.8±5.4 GPa for SS-0, E=182.6±2.8 GPa for SS-800, E=171.5±6.0 GPa for SS-1000, and E=155.7±6.7 GPa for SS-1100. The microstructure reorganizing and the reduction in the rate of stack dislocations after annealing the coatings at higher temperatures leads to the reduction in the elastic modulus [4.37].

The resistance to plastic deformation H^3/E^2 of SS-0 coating is approximately 0.079 GPa and it is higher than that of SS-800 with 0.048 GPa, SS-1000 with 0.036±0.49 GPa and SS-1100 with 0.020±0.06 GPa, suggesting better wear resistances for SS-0 [4.17].

Figure 4.30 presents the typical nanoindentation load-displacement curves for all the four coatings. According to the curves, W_P of SS-0 coating is the lowest, followed by SS-800, SS-1000 and finally SS-1100. Those results are well correlated with the resistance to plastic deformation H^3/E^2 results listed above in **Table 4.11**. From the nanoindentation load-displacement curves, the elastic recoveries of all the four coatings are calculated and their values are 60.39% for SS-0, 34.66% for SS-800, 29.27% for SS-1000 and 25.64% for SS-1100.

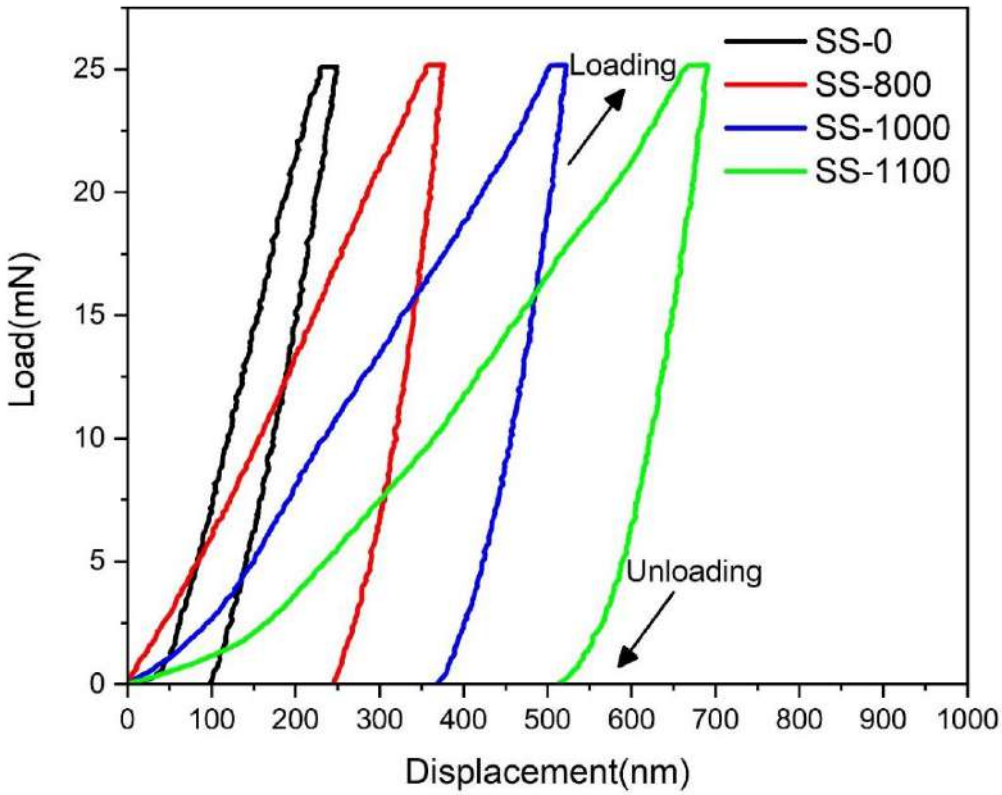


Figure 4.30 Typical nanoindentation curves for: SS-0, SS-800, SS-1000 and SS-1100

4.3.4. Tribological results for the third optimization

Figure 4.31 presents COF variation versus the sliding distance for: SS-0, SS-800, SS-1000 and SS-1100 coatings. The friction curves of SS-1000 and SS-1100 coatings show different variation trends than SS-0 and SS-800. SS-0 and SS-800 exhibit two stages according to their COF values. The first stage is characterized by a sharp increase of COFs up to peaks of $\mu \approx 0.70$ at 21 m for SS-0 and $\mu \approx 0.58$ at 6.8 m for SS-800. The second stage starts by a decreasing trend followed by stabilization at COFs of $\mu \approx 0.48$ for SS-0 and $\mu \approx 0.53$ for SS-800. For SS-1000 and SS-1100 coatings, the friction coefficients first increase sharply and with less velocity for SS-1100, then they reach stable values of $\mu \approx 0.56$ for SS-1000 and $\mu \approx 0.46$ for SS-1100.

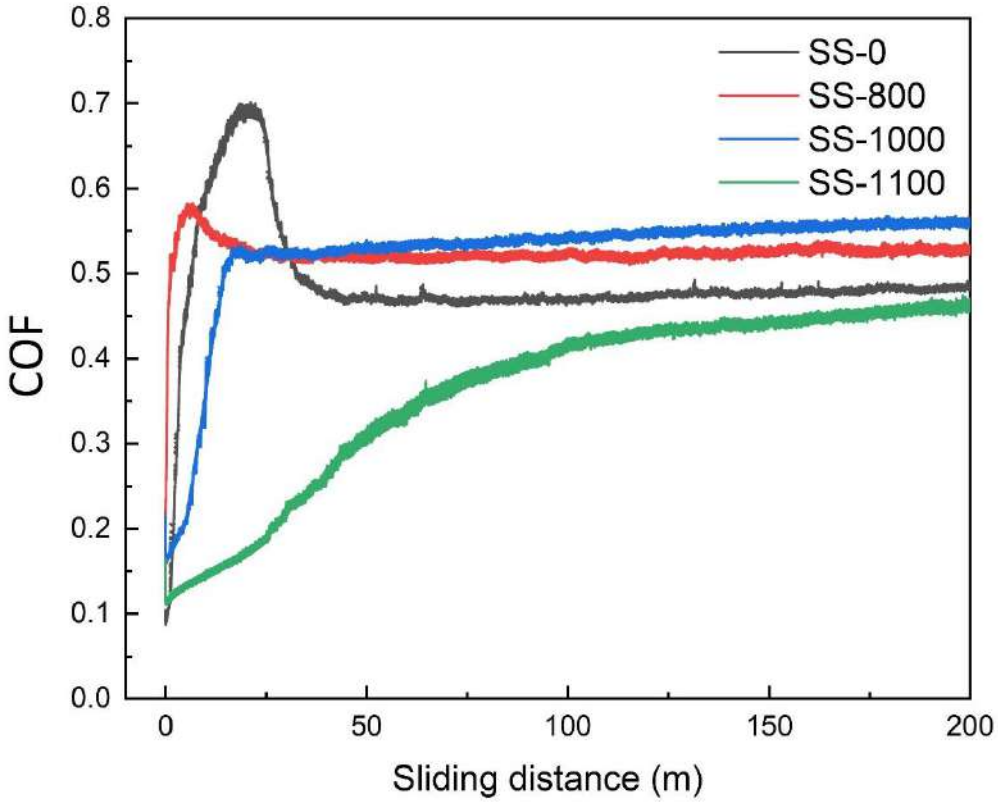


Figure 4.31 COF variations as function of the sliding distance for: SS-0, SS-800, SS-1000 and SS-1100

Table 4.12 shows the tribological test results of all the four coatings. SS-1100 has the lowest COF of μ=0.36±0.12. SS-0 presents also a low COF of μ=0.49±0.07, while the highest COFs are those measured for SS-800 and SS-1000 with μ=0.52±0.07 and μ=0.52±0.09 respectively. The high microstructure density of SS-1100 coating has a significant effect on the reduced COF. SS-0 has the lowest wear rate of $k=5.43\pm0.30\cdot10^{-5}$ $mm^3/N\cdot m$, followed by SS-800 with $k=7.07\pm0.43\cdot10^{-5}$ $mm^3/N\cdot m$, and SS-1000 with $k=7.35\pm0.24\cdot10^{-5}$ $mm^3/N\cdot m$, while SS-1100 has a high wear rate of $k=8.39\pm0.60\cdot10^{-5}$ $mm^3/N\cdot m$. The wear rate measurements are proportional to the hardness results listed above in section 4.3.3 and in correlation with the Archard wear theory [4.37].

Coatings	SS-0	SS-800	SS-1000	SS-1100
COF	0.49±0.07	0.52±0.07	0.52±0.09	0.36±0.12
k x10^{-5} (mm^3/N·m)	5.43±0.30	7.07±0.43	7.35±0.24	8.39±0.60

Table 4.12 Tribological test results for: SS-0, SS-800, SS-1000 and SS-1100

Figure 4.32 shows the wear tracks observations. Deep grooves and scaling pits can be observed in all the four coatings wear tracks, suggesting delamination wear mechanism that is accompanied with abrasive wear. Large flake-like debris that are delaminated from the coating surfaces can be observed also. The flake-like debris sizes are reduced with the increased annealing temperature.

SS-800 coating was under the same wear mechanism as the SS-0 coating characterized above in section 4.2.4.

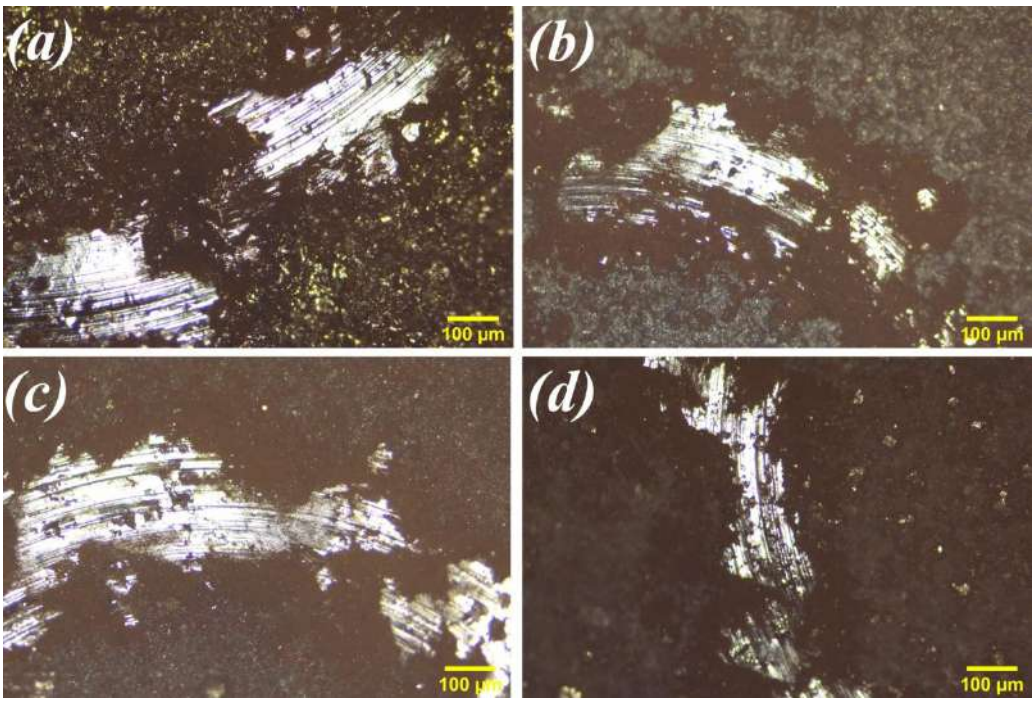


Figure 4.32 Optic microscope wear tracks observations for: (a) SS-0, (b) SS-800, (c) SS-1000 and (d) SS-1100

For SS-1000 and SS-1100 coatings, with the high diffused oxides to the surface as it was observed by the EDS analysis above in **Figure 4.25**, the dominate wear mechanism is the delamination wear [4.25], owing to the presence of a high amount of oxides in their surfaces that lowers the amount of the inter-splats bounding and thereby reduce their toughness and wear resistance [4.10]. So, at the beginning of the test, severe delaminations wear that are accompanied later with the abrasive wear are taking place. Then, the formation of the protective oxide layers on the wear tracks stabilizes the wear process and the obtained COFs.

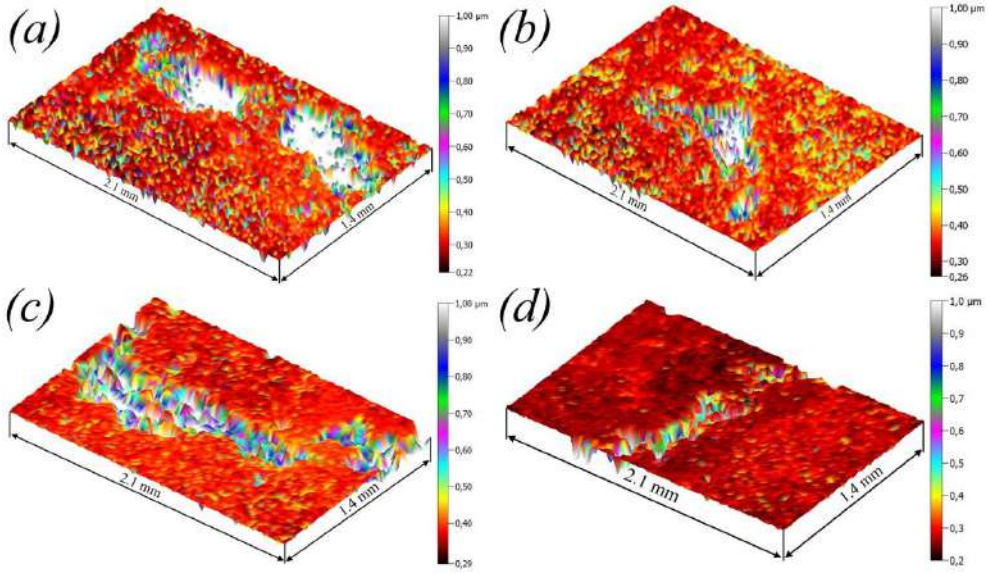


Figure 4.33 AFM 3D images of wear tracks profiles for: (a) SS-0, (b) SS-800, (c) SS-1000 and (d) SS-1100

Figure 4.33 shows 3D images of the wear tracks profiles for the four coatings. SS-0, SS-800 and SS-1000 present the same wear depth value of D_P=0.012 mm, while SS-1100 have a higher wear depth of D_P=0.018 mm. The shallow depths of the first three coatings are related to their high hardness that leads to the initiation and the propagation of the micro-cracks at a shallower position below the surface, giving lower delamination wear depths and grooves [4.20]. Wear track width measurements reveal that SS-0 and SS-1100 have the narrowest

profiles with respectively: w=0.273 mm and w=0.280 mm. SS-800 have a wear track width of w=0.331 mm, while SS-1000 has the widest wear track of w=0.363 mm.

4.3.5. Electrochemical results for the third optimization

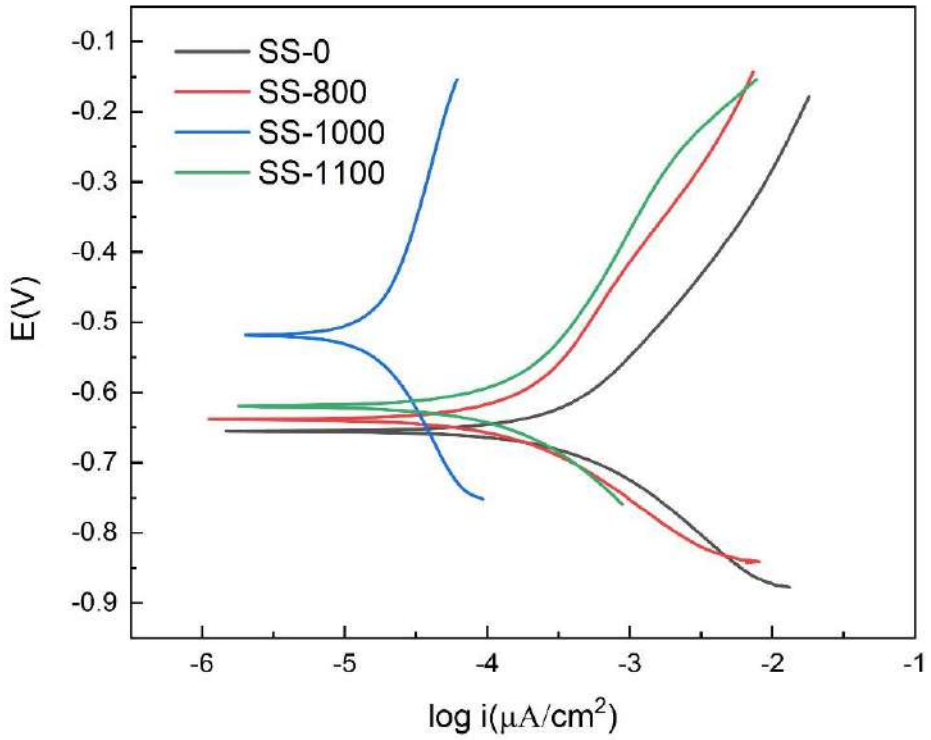


Figure 4.34 Polarization curves for: SS-0, SS-800, SS-1000 and SS-1100

Figure 4.34 presents the polarization curves for the different coatings. E_{OC}, i_{corr} and C_R are given in **Table 4.13**.

E_{OC} values present its highest value for SS-1000 with E_{OC}=-0.518 V. i_{corr} reveals a low value in the case of SS-800 and SS-1100 with i_{corr}=1.122 μA/cm^2 and i_{corr}=1.809 μA/cm^2 respectively, while for the as-sprayed coating a high i_{corr} value is obtained with i_{corr}=3.032 μA/cm^2. According to the **Table 4.13** results, it can be conclude that the annealed coatings have better corrosion resistance than the as-sprayed coating, that can be attributed to the reduction in their porosity and the strengthening of their inter-particles bounding, because the

corrosion process starts first around the pores and the inter-particles boundaries [4.39], then, the electrolyte penetrates through the interconnected pores, where the rate of penetration is depending on the number of the pores. After the penetration of the electrolyte into the substrate, a galvanic pair is formed in the interface between the coating and the substrate because of the noble nature of the stainless steel coating, causing the acceleration of the corrosion and the detachment of the coating at the end [4.40].

Sample	**C_R (mpy)**	**E_{OC} (V)**	**i_{corr} (µA/cm^2)**
SS-0	0.186	-0.655	3.032
SS-800	0.069	-0.638	1.122
SS-1000	0.124	-0.518	2.019
SS-1100	0.111	-0.619	1.809

Table 4.13 Electrochemical test results for: SS-0, SS-800, SS-1000 and SS-1100

SS-800 has the highest resistance to corrosion than the other annealed coatings, and that is related to two reasons: the low oxides amount and the high Cr and Ni amount in their surface as it was presented above in the EDS analysis in **Figure 4.25**. Coating oxides such as iron oxides [4.21] and chromium oxides [4.23] impaired the corrosion resistance of the Stainless steel coatings by changing their electrochemical potential after the dissolution of the oxides in the electrolyte. In the same time, the diffusion of Cr and Ni into the coating surface after annealing has a major role in enhancing the corrosion resistance of the stainless steel coatings [4.39].

4.3.6. The performance factors $K_{P3(SS-800)}$, $K_{P3(SS-1000)}$) and $K_{P3(SS-1100)}$

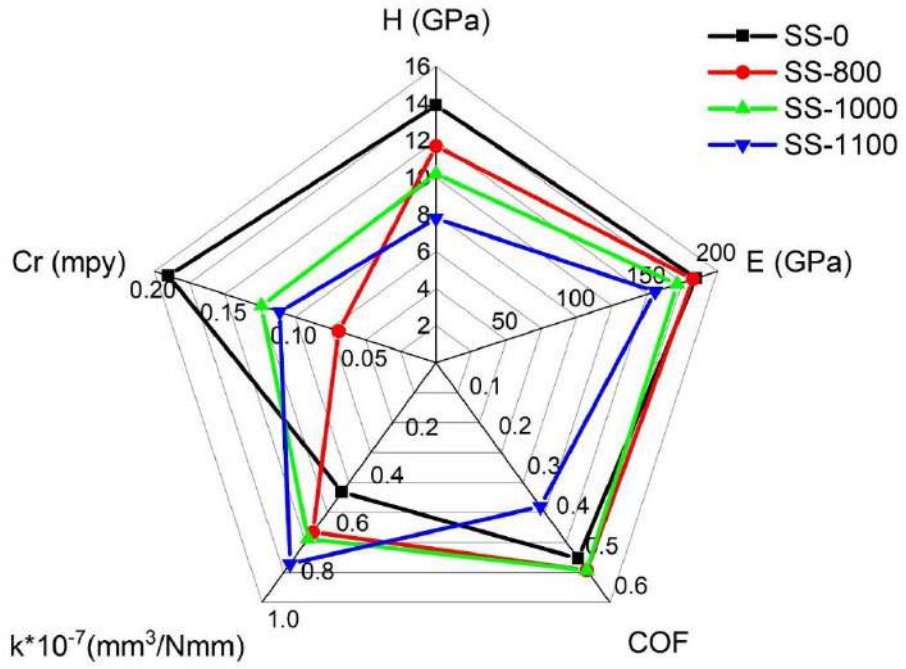


Figure 4.35 Polar diagrams providing a qualitative comparison of the coatings: SS-0, SS-800, SS-1000 and SS-1100

A qualitative comparison between the different coatings according to their hardness, elastic modulus, friction coefficient, wear rate and corrosion rate is given in the polar diagram shown in **Figure 4.35**. The diagram reveals that the SS-0 coating has high hardness, elastic modulus, COF and corrosion rate while having low wear rate value. In the contrary, SS-800 displays high hardness, elastic modulus, COF and wear rate while having low corrosion rate, suggesting that the SS-800 coating has good surface behaviour comparing with the rest of the coatings.

The above qualitative assessment can be confirmed by calculating the performance factors of the four coatings using the equation (3.3) to choose the best coating and so the optimal annealing temperature.

The performance factor of the SS-0 coating was already calculated in the previous sub-chapter and it has as value:

$$K_{P3(SS-0)} = K_{P2(SSC-4L)} = 276.48 \cdot 10^{10}\ N^2 \cdot year/mm^5$$

The performance factors for SS-800, SS-1000 and SS-1100 are respectively: $K_{P3(SS-800)}$, $K_{P3(SS-1000)}$ and $K_{P3(SS-1100)}$, and they can be calculated using respectively the equations: (4.7), (4.8) and (4.9), given as the following:

$$K_{P3(SS-800)} = \frac{H_{(SS-800)}}{C_{R(SS-800)} \cdot \mu_{(SS-800)} \cdot k_{(SS-800)}}\ [N^2 \cdot year/mm^5] \quad (6.1)$$

$$K_{P3(SS-1000)} = \frac{H_{(SS-1000)}}{C_{R(SS-1000)} \cdot \mu_{(SS-1000)} \cdot k_{(SS-1000)}}\ [N^2 \cdot year/mm^5] \quad (6.2)$$

$$K_{P3(SS-1100)} = \frac{H_{(SS-1100)}}{C_{R(SS-1100)} \cdot \mu_{(SS-1100)} \cdot k_{(SS-1100)}}\ [N^2 \cdot year/mm^5] \quad (6.3)$$

The different factors values are given in **Table 4.14**.

coatings	H_N (N/mm^2)	C_R (mpy)	COF	k (mm^3/N·mm)
SS-800	$11.7 \cdot 10^3$	0.069	0.52	$7.07 \cdot 10^{-8}$
SS-1000	$10.2 \cdot 10^3$	0.124	0.52	$7.35 \cdot 10^{-8}$
SS-1100	$7.8 \cdot 10^3$	0.111	0.36	$8.39 \cdot 10^{-8}$

Table 4.14 Factors values of: SS-800, SS-1000 and SS-1100

The calculated factors of performance are:

$$K_{P3(SS-800)} = 461.23 \cdot 10^{10}\ N^2 \cdot year/mm^5$$

$$K_{P3(SS-1000)} = 215.22 \cdot 10^{9}\ N^2 \cdot year/mm^5$$

$$K_{P3(SS-1100)} = 232.65 \cdot 10^{10}\ N^2 \cdot year/mm^5$$

SS-800 has the highest factor of performance then all the rest of the coatings because it has a high hardness and wear rate and the lowest corrosion rate.

From the above results, SS-800 coating will be considered as the optimal and will be chosen as the base coating for the PIII nitruration treatment and W-Ti-N thin film in the next chapters.

4.4. Conclusions

The aim of the present chapter is to obtain an optimal SSC obtained through TWAS that have better surface properties than the massive stainless steel 304-SSB. The optimal SSC will be used as the base coating for the PIII nitruration treatment and W-Ti-N thin film in the next chapters.

In the first part, two grades of stainless steels which are not sufficiently studied, 304L and 317L are deposited. The microstructural results revealed that 304L-SSC contains lower porosity and oxides than 317L-SSC, while 317L-SSC has lower surface roughness. Mechanical characterization showed that 317L-SSC has higher hardness than 304L-SSC and 304-SSB. The Tribological tests results showed that a lower COF value was obtained for 304L-SSC ($\mu=0.52\pm0.15$), hence, the lower wear rate was measured for 317L-SSC ($k=1.35\pm0.02$ $m^3/N\cdot m$). The delamination wear combined with the abrasive wear were the main wear mechanisms for the two coatings. The electrochemical characterization revealed that the lowest corrosion rate was obtained for 304L-SSC with $C_R=13.03$ mpy. Pitting then galvanic corrosion were the main corrosion mechanisms for both coatings. The calculated factures of performance showed that 304L-SSC has higher factor than 317L-SC, with low corrosion behaviour that need to be enhanced more.

The second part consists of enhancing the 304L-SSC behaviour by increasing the number of layers from 1 to 4. Microstructural analysis showed that the SS-4L has the highest oxides amount and the wider sprayed splats and that the splats sizes increase with the number of layers. The surface roughness was reduced when increasing the number of layers from 209±1.2 nm for SS-1L to 171.0±1.6 nm for SS-4L. Mechanical analysis results revealed that SS-4L and SS-3L have the highest hardness. Tribological analysis showed that both SS-3L and SS-4L have the lowest COFs of μ=0.49±0.06 and μ=0.49±0.07 respectively, and that the SS-4L has the lowest wear rate with $k=0.54\pm0.03\cdot10^{-4}$ $mm^3/N\cdot m$. Electrochemical tests results showed that both SS-2L and SS-3L have very interesting corrosion behaviours. The calculated factors of performance of the 4 coatings show that SS-4L presents the highest value.

In the last part, annealing post-treatment is applied on the optimized multilayer coating with 3 different temperatures that are 800°C, 1000°C and 1100°C. Microstructural analysis showed that the coating without annealing treatment contains the highest amount of oxides of 29.03 wt.%. The aspect of the coating surface was transformed from the typical arc sprayed splats aspect into a coating surface full of dot-like shapes after annealing at 800°C and of dense flakes and needle-like shapes at 1000°C and 1100°C. Mechanical analysis showed that with increasing the annealing temperature, the hardness decrease with the annealing temperatures. The same trend was observed for the elastic modulus. Roughness and tribological analysis revealed that the coating annealed at 1100°C has lubricated surface behaviours with very a smooth surface (Ra=67.5±3.8 nm) and very low COF (μ=0.36±0.12). For the coatings wear rates, it is observable that they increase with increasing the annealing temperatures in correlation with the surface hardness. The lowest wear rate is that obtained for the coating without annealing treatment with $k=5.43\cdot10^{-5}\pm0.30$ $mm^3/N\cdot m$. The electrochemical test

results revealed that the coating annealed at 800°C has a very interesting corrosion rate of C_R=0.069 mpy. The coating with the highest factor of performance is the one annealed at 800°C.

After obtaining an optimal 304L stainless steel multilayer coating with higher surface properties than the massive stainless steel. It is now time to apply an optimized duplex system made from the PIII nitriding treatment and the W-Ti-N thin film, which is the objective of the next chapters.

References

[4.1] L. Pawlowsky, *The science and engineering of thermal spray coatings*, John Wiley & Sons, England, 2008.

[4.2] H.K. Kang, Development of a cathode layer ($La_{0.8}Sr_{0.2}MnO_3$) in a solid oxide fuel cell using a reactive plasma spray, *Met. Mater. Int.*, 2004, **10**, p 479-483.

[4.3] J. Nohava, R. Musalek, J. Matejıcek, and M. Vilemova, A contribution to understanding the results of instrumented indentation on thermal spray coatings-case study on Al_2O_3 and stainless steel, *Surf. Coat. Technol.*, 2014, **240**, p 243-249.

[4.4] M.H.A. Malek, N.H. Saad, S.K. Abas, and N.M. Shah, Thermal arc spray overview, *IOP Conference Ser.: Mater. Sci. Eng.*, 2013, **46**, 012028.

[4.5] B. Sun, H. Fukanuma, and N. Ohno, Study on stainless steel 316L coatings sprayed by a novel high pressure HVOF, *Surf. Coat. Technol.*, 2014, **239**, p 58-64.

[4.6] A. Kocaman, and O. Keles, Antibacterial efficacy of wire arc sprayed copper coatings against various pathogens, *J. Therm. Spray Tech.*, 2019, **28**, p 504-513.

[4.7] X. Meng, J. Zhang, W. Han, and J. Zhao, Fracture behavior of cold sprayed 304 stainless steel coating during cold rolling, *J. Iron Steel Res. International*, 2012, **19**, p 57-63.

[4.8] A. Belamri, A. Ati, M. Braccini, and S. Azem, Hypereutectoid steel coatings obtained by thermal flame spraying - Effect of annealing on microstructure, tribological properties and adhesion energy, *Surf. Coat. Technol.*, 2015, **263**, p 86-99.

[4.9] Y. Chen, B. Xu, Y. Liu, X. Liang, and Y. Xu, Structure and sliding wear behavior of 321 stainless steel/Al composite coating deposited by high velocity arc spraying technique, *Transactions Nonferrous Metals Soc. China*, 2008, **18**, p 603-609.

[4.10] M. Villa, S. Dosta, and J.M. Guilemany, Optimization of 316L stainless steel coatings on light alloys using Cold Gas Spray, *Surf. Coat. Technol.*, 2013, **235**, p 220-225.

[4.11] V.E. Porsev, A.L. Ulyanov, and G.A. Dorofeev, Atomic redistribution in a Fe-Cr system in the course of mechanical alloying and subsequent annealing, *Metallurgical Mater. Transactions A*, 2019, **50**, p 5977-5989.

[4.12] M.M. Abdullah, F.M. Rajab, and S.M. Al-Abbas, Structural and optical characterization of Cr_2O_3 nanostructures: evaluation of its dielectric properties, *AIP Adv.*, 2014, **4**, 027121.

[4.13] H. Edris, A. Shafyei, H. Salimi-Jazi, and E. Abdolvand, Evaluation of hydrogen permeation through standalone thermally sprayed coatings of AISI 316L stainless steel, *International J. Hydrogen Energy*, 2018, **43**, p 4657-4670.

[4.14] S. García-Rodríguez, B. Torres, N. Pulido-González, E. Otero, and J. Rams, Corrosion behavior of 316L stainless steel coatings on ZE41 magnesium alloy in chloride environments, *Surf. Coat. Technol.*, 2019, **378**, 124994.

[4.15] S. García-Rodríguez, A.J. López, B. Torres, and J. Rams, 316L stainless steel coatings on ZE41 magnesium alloy using HVOF thermal spray for corrosion protection, *Surf. Coat. Technol.*, 2016, **287**, p 9-19.

[4.16] K. Chemaa, Y. Chabani, M. Gaceb, and S. Hassani, “Study of tribological properties of titanium-based thin films applied to the rubbing parts of internal combustion engines piston”, Master degree Thesis, M'hamed Bougara University Boumerdes, 2017.

[4.17] L. Fan, H. Chen, Y. Dong, L. Dong, and Y. Yin, Wear and corrosion resistance of laser-cladded Fe-based composite coatings on AISI 4130 steel, *Int. J. Miner. Metall. Mater.*, 2018, **25**, p 716-728.

[4.18] N.P. Suh, *Tribophysics*, Prentice-Hall, New Jersey, 1986.

[4.19] B. Xu, Z. Zhu, S. Ma, W. Zhang, and W. Liu, Sliding wear behavior of Fe-Al and Fe-Al/WC coatings prepared by high velocity arc spraying, *Wear*, 2004, **257**, p 1089-1095.

[4.20] G. Jin, B. Xu, H. Wang, Q. Li, and S. Wei, Microstructure and tribological properties of stainless steel coatings sprayed by two methods based on spraying, *Surf. Coat. Technol.*, 2007, **201**, p 5261-5263.

[4.21] J.M. Guilemany, J. Fernández, N. Espallargas, P.H. Suegama, and A.V. Benedetti, Influence of spraying parameters on the electrochemical behaviour of HVOF thermally sprayed stainless steel coatings in 3.4% NaCl, *Surf. Coat. Technol.*, 2006, **200**, p 3064-3072.

[4.22] K. Spencer, and M. Zhang, Optimisation of stainless steel cold spray coatings using mixed particle size distributions, *Surf. Coat. Technol.*, 2011, **205**, p 5135-5140.

[4.23] L. Zhao, and E. Lugscheider, Influence of the spraying processes on the properties of 316L stainless steel coatings, *Surf. Coat. Technol.*, 2002, **162**, p 6-10.

[4.24] M. Moshref-Javadi, H. Edris, A. Shafyei, H. Salimi-Jazi, and E. Abdolvand, Evaluation of hydrogen permeation through standalone thermally sprayed coatings of AISI 316L stainless steel, *International J. Hydrogen Energy*, 2018, **43**, p 4657-4670.

[4.25] E.P. Song, B. Hwang, S. Lee, N.J. Kim, and J. Ahn, Correlation of microstructure with hardness and wear resistance of stainless steel blend coatings fabricated by atmospheric plasma spraying, *Mater. Sci. Eng. A*, 2006, **429**, p 189-195.

[4.26] H. Zhao, H. Zhang, X. Chen, A. McDonald, and H. Li, Effect of chlorella vulgaris biofilm adhesion on electrochemical behaviors of wire arc-sprayed aluminum coatings, *J. Therm. Spray Technol.*, 2020, **29**, p 1991-2000.

[4.27] S. García-Rodríguez, B. Torres, A.J. López, E. Otero, and J. Rams, Characterization and mechanical properties of stainless steel coatings deposited by HVOF on ZE41 magnesium alloy, *Surf. Coat. Technol.*, 2019, **359**, p 73-84.

[4.28] P.H. Gao, S.T. Cao, J.P. Li, Z. Yang, Y.C. Guo, and Y.R. Wang, High temperature oxidation resistance of M42C stainless steel coatings deposited on the surface of cast iron through atmospheric plasma spraying, *J. Alloys Compounds*, 2016, **684**, p 188-194.

[4.29] M.I. Boulos, P. Fauchais, and E. Pfender, Wire-Arc Spray Torches, *Handbook of Thermal Plasmas*, Springer International Publishing, Switzerland, 2018, p 1-52.

[4.30] E.P. Song, J. Ahn, S. Lee, and N.J. Kim, Effects of critical plasma spray parameter and spray distance on wear resistance of Al_2O_3-8 wt.%TiO_2 coatings plasma-sprayed with nanopowders, *Surf. Coat. Technol.*, 2007, **202**, p 3625-3632.

[4.31] B. Dikici, H. Yilmazer, I. Ozdemir, and M. Isik, The effect of post-heat treatment on microstructure of 316L cold-sprayed coatings and their corrosion performance, *J. Therm. Spray. Technol.*, 2016, **25**, p 704-714.

[4.32] A.H. Ettefagh, and S. Guo, Electrochemical behavior of AISI316L stainless steel parts produced by laser-based powder bed fusion process and the effect of post annealing process, *Addit. Manufacturing*, 2018, **22**, p 153-156.

[4.33] J. Lin, Z. Wang, P. Lin, J. Cheng, X. Zhang, and S. Hong, Effects of post annealing on the microstructure, mechanical properties and cavitation erosion behavior of arc-sprayed FeNiCrBSiNbW coatings, *Mater. Des.*, 2015, **65**, p 1035-1040.

[4.34] W. Guo, Y. Wu, J. Zhang, and W. Yuan, Effect of the long-term heat treatment on the cyclic oxidation behavior of Fe-based amorphous/nanocrystalline coatings prepared by high-velocity arc spray process, *Surf. Coat. Technol.*, 2016, **307**, p 392-398.

[4.35] X.M. Meng, J.B. Zhang, W. Han, J. Zhao, and Y.L. Liang, Influence of annealing treatment on the microstructure and mechanical performance of cold sprayed 304 stainless steel coating, *Appl. Surf. Sci.*, 2011, **258**, p 700-704.

[4.36] Q.Y. Wang, Y.C. Xi, Y.H. Zhao, S. Liu, S.L. Bai, and Z.D. Liu, Effects of laser re-melting and annealing on microstructure, mechanical property and corrosion resistance of Fe-based amorphous/crystalline composite coating, *Mater. Characterization*, 2017, **127**, p 239-247.

[4.37] P. Coddet, C. Verdy, C. Coddet, F. Debray, and F. Lecouturier, Mechanical properties of thick 304L stainless steel deposits processed by He cold spray, *Surf. Coat. Technol.*, 2015, **277**, p 74-80.

[3.38] C. Godoy, E. Souza, M. Lima, and J.C. Batista, Correlation between residual stresses and adhesion of plasma sprayed coatings: effects of a post-annealing treatment, *Thin Solid Films*, 2002, **420-421**, p 438-445.

[4.39] J. Frattolin, R. Roy, S. Rajagopalan, M. Walsh, S. Yue, O.F. Bertrand, and R. Mongrain, A manufacturing and annealing protocol to develop a cold-sprayed Fe-316L stainless steel biodegradable stenting material, *Acta Biomaterialia*, 2019, **99**, p 479-494.

[4.40] P.H. Suegama, C.S. Fugivara, A.V. Benedetti, J. Fernández, J. Delgado, and J.M. Guilemany, Electrochemical behavior of thermally sprayed stainless steel coatings in 3.4% NaCl solution, *Corrosion Sci.*, 2005, **47**, p 605-620.

Chapter 5

Improving the tribological behaviour of the stainless steel coating nitrided by PIII

5.1. Introduction

After obtaining an optimal stainless steel coating with upgraded surface properties than the massive stainless steel in the previous chapter, this coating will be nitrided using PIII process in order to improve their tribological properties in one side and to form an interlayer for the W-Ti-N thin film in another side. This will be the objective of the present chapter. The experimental details and the PIII system setup description were already presented in the section 3.5. The optimized stainless steel coating which is SS-800 will be referred to in this chapter by SSC. The coating nitrided with injected power of 200 W will be referred to by PIII-200 and finally the coating nitrided with injected power of 300 W will be referred to by PIII-300.

5.2. Microstructural characterization

Figure 5.1 shows the XRD diffraction patterns of: (a) SSC, (b) PIII-200, (c) PIII-300. The

XRD patterns of the nitrided coatings shows the formation of iron nitrides such as $Fe_{2-3}N$ known by ε phase and Fe_4N known by γ' phase. At 200 W, the nitrided coating has ε phase with higher relative intensity than the coating nitrided at 300 W, inversely, at 300 W the coating has higher relative intensity of γ' phase, this is an indication of phase transformation from ε phase to γ' phase with increasing the nitriding discharge power from 200 W to 300 W [5.1]. It was reported elsewhere [5.2] that with increasing the time or the temperature of the classical plasma nitriding process, the composition of ε and γ' phases was changed inversely, this can be explained according to the Koelbel's models [5.1] which reported that while the plasma bombardment is carried on during the nitriding process, the iron nitride phases are unstable and they transformed first into ε phase and later on into γ' phase. With PIII process, the phase transformation after increasing the discharge power is related to the increasing in the coatings self-heating due to the higher ion bombardment energy which is proportional with the discharge power.

It is also remarkable that with increasing the nitriding discharge power from 200 W to 300 W, the γ' phase relative peaks are shifted to lower angles which is an indication of larger lattice expansion due to the insertion of more nitrogen atoms [5.3].

The relative intensity of γ' phase is higher than that of γ phase in both nitrided coatings, indicating that γ' phase is abundant in the near surface of the coatings [5.4] and that is related to the PIII process that promote an effective nitrogen implantation at low depths in the order of nanometers. γ' phase is a metastable fcc solid solution supersaturated in nitrogen. This phase is characterized by a high hardness and wear resistance [5.5], suggesting a superior surface property of the nitrided coatings in one side and of the coating nitrided at 300 W in the other.

Cubic chromium nitride CrN phase is also obtained. Generally, when nitriding massive 304 stainless steels at high temperatures (more than 500°C) using PIII process, this phase starts to appear simultaneously with the disappearance of γ' phase [5.6]. In addition, the hexagonal Cr_2N and Ni_3N phases are also observed [5.7, 5.8], with higher intensity in the nitrided coating at 300 W phase.

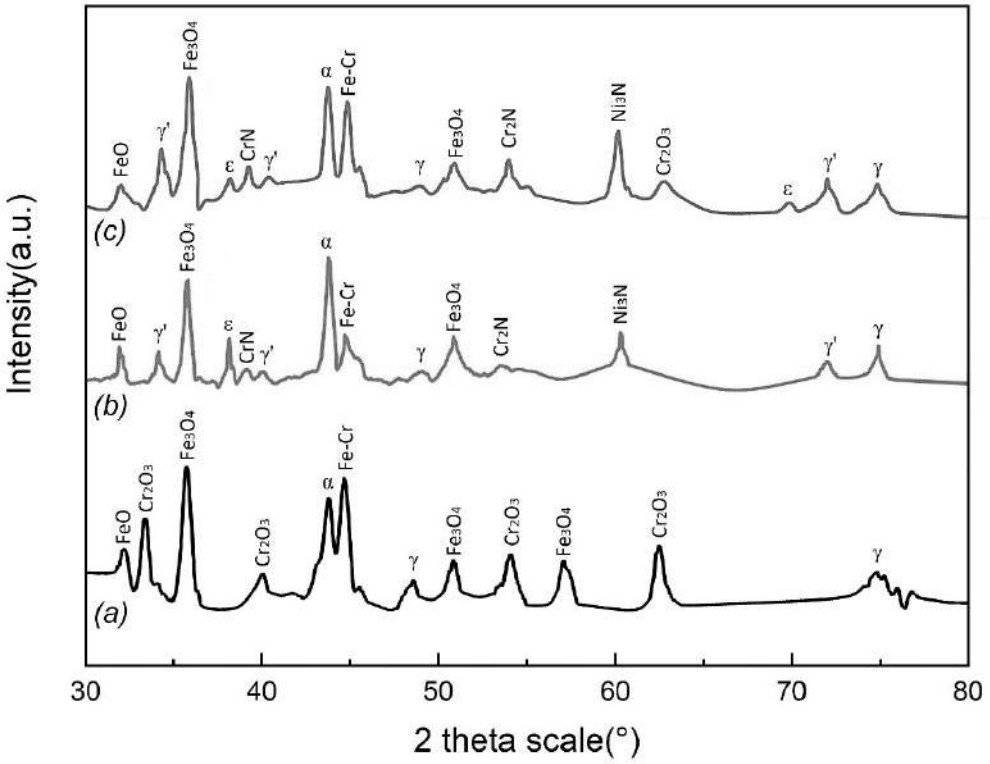


Figure 5.1 XRD diffraction patterns of: (a) SSC, (b) PIII-200, (c) PIII-300

Figure 5.2 shows the SEM surface morphologies for: (a) SSC, (b) PIII-200 and (c) PIII-300. SSC has a surface morphology with dot-like shapes. After nitriding, the dot-like shapes start to disappear, probably due to the nitrogen atoms diffusion. The surface become uniform with increasing the discharge power.

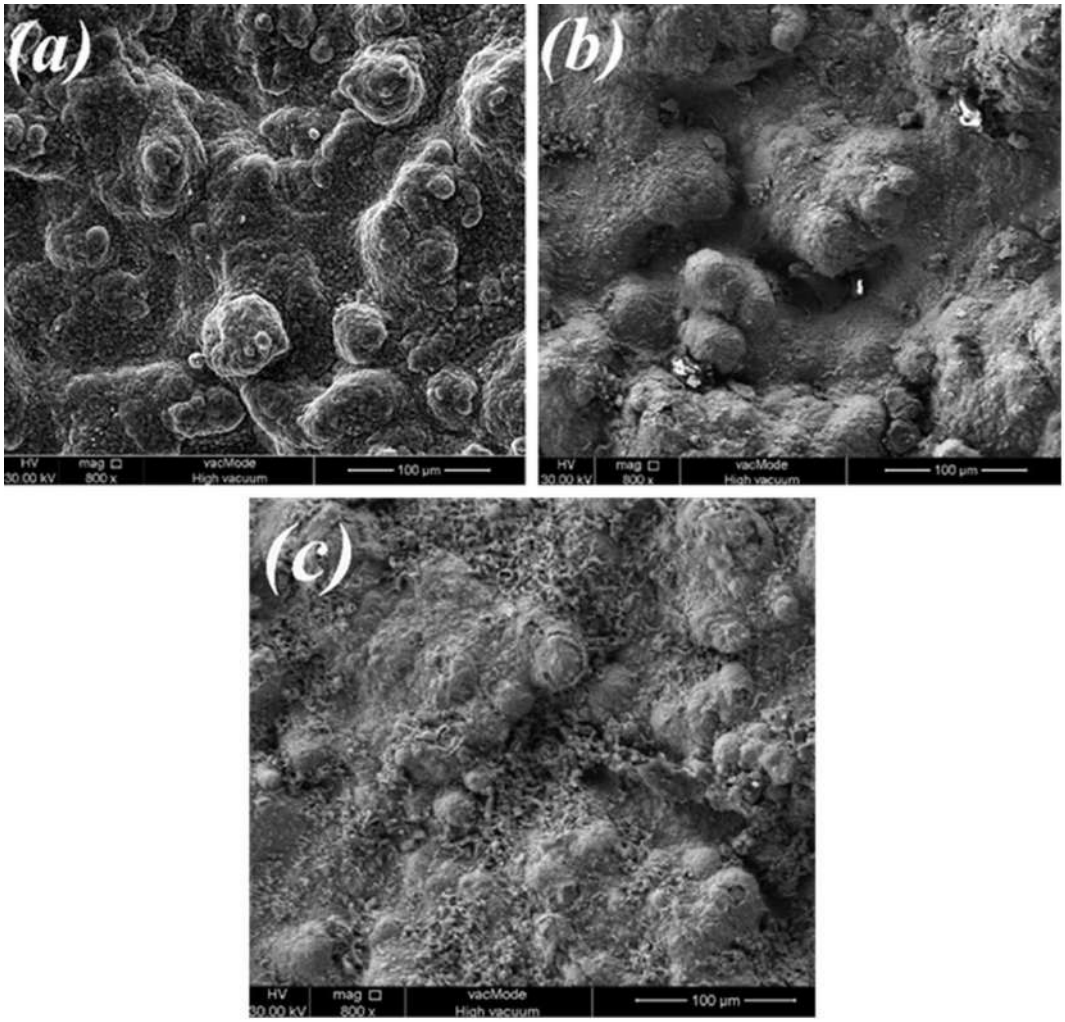


Figure 5.2 SEM surface morphologies for: (a) SSC, (b) PIII-200 and (c) PIII-300

Figure 5.3 presents the cross-section images of: (a) SSC, (b) PIII-200 and (c) PIII-300. All the three coatings display the dense and the smooth microstructure. The bright zones full of oxides represent the coatings interfaces. The coatings thicknesses are in the order of 800 µm. After nitriding under 200 W, the nitrided layers show similar morphologies of the rest of the coating because the nitrogen atoms diffuse in the interface direction along the interstitial sites [5.2]. While the nitrided layers under 300 W has different morphology than the rest of the coating.

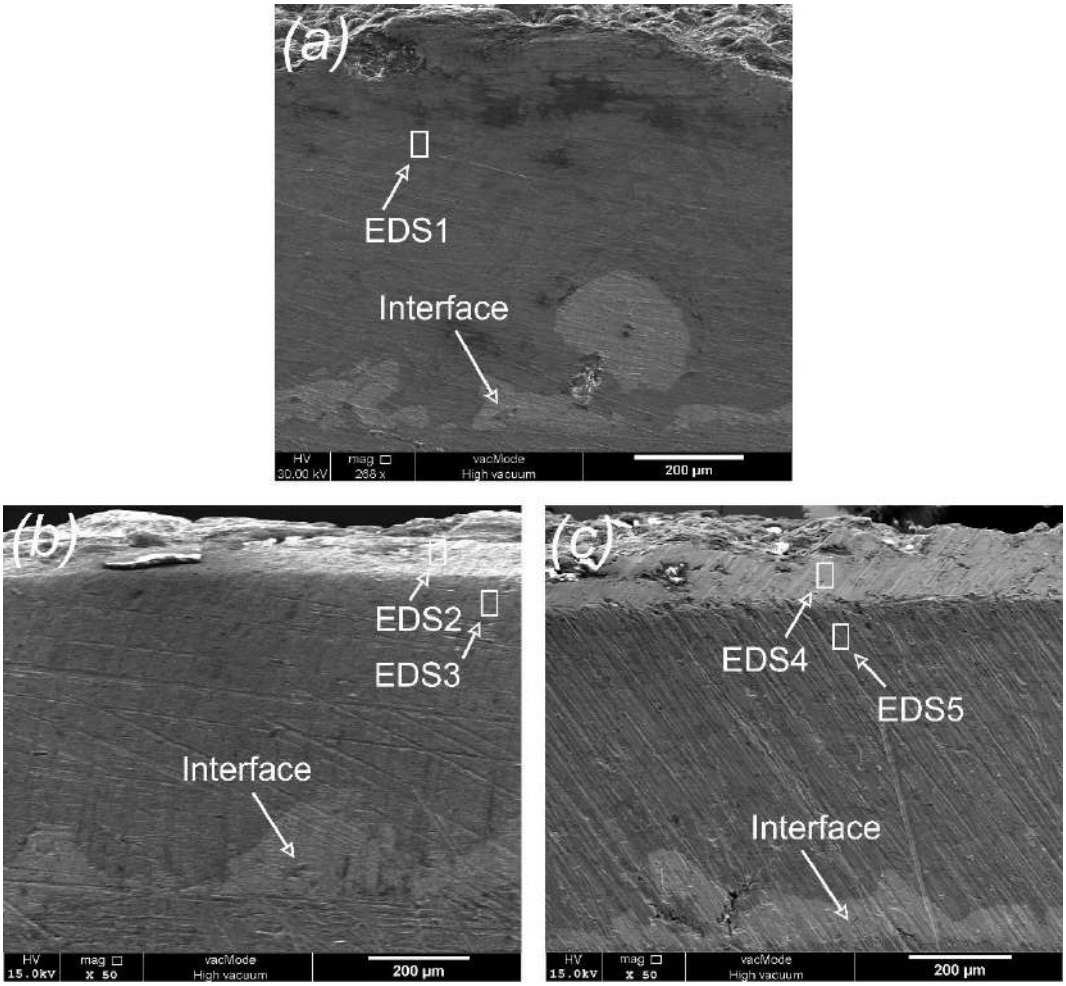


Figure 5.3 Cross-section images of: (a) SSC, (b) PIII-200 and (c) PIII-300

Figure 5.4 shows the EDS analysis results at the different zones indicated in **Figure 5.2**. For SSC, the oxides amount is 11.70 wt.% and the Ni and Cr compositions are respectively of 7.79 wt.% and 17.87 wt.%. For PIII-200 a small amount of nitrogen was detected in the surface with 3.10 wt.%, while no nitrogen atom was detected at EDS3 zone. The oxides amount was increased after nitriding under 200 W from 11.70 wt.% into 23.66 wt.% which is a sign of oxides diffusion from the interface into the surface of the coating at the vacuum conditions through the coatings pores. For PIII-300, higher amount of nitrogen of 9.72 wt.% was detected in the surface whereas small amounts of oxides were detected (3.30 wt.% at EDS4 and 1.27 wt.% at EDS5).

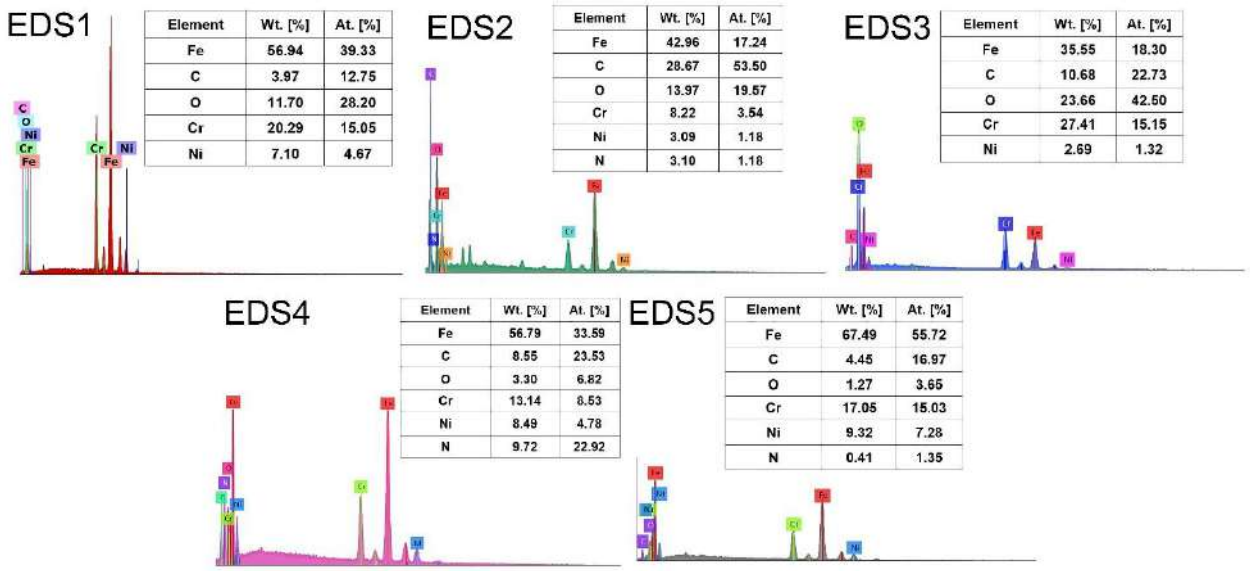


Figure 5.4 EDS analysis results at the different zones

Figure 5.5 shows the roughness arithmetic mean (Ra) for: (a) SSC, (b) PIII-200 and (c) PIII-300. The roughness is reduced after nitriding from: Ra≈ 43 nm for the non nitrided coating into Ra≈ 40 nm and Ra≈ 33 nm for PIII-200 and PIII-300 respectively. This reduction is related to the application of Ar^+ ion bombardment before nitriding that modifies the surface morphology by increasing the energy associated with atoms on the nitrided coatings surfaces that produce a reduction of roughnesses and grain sizes [5.8]. The lower roughness of PIII-

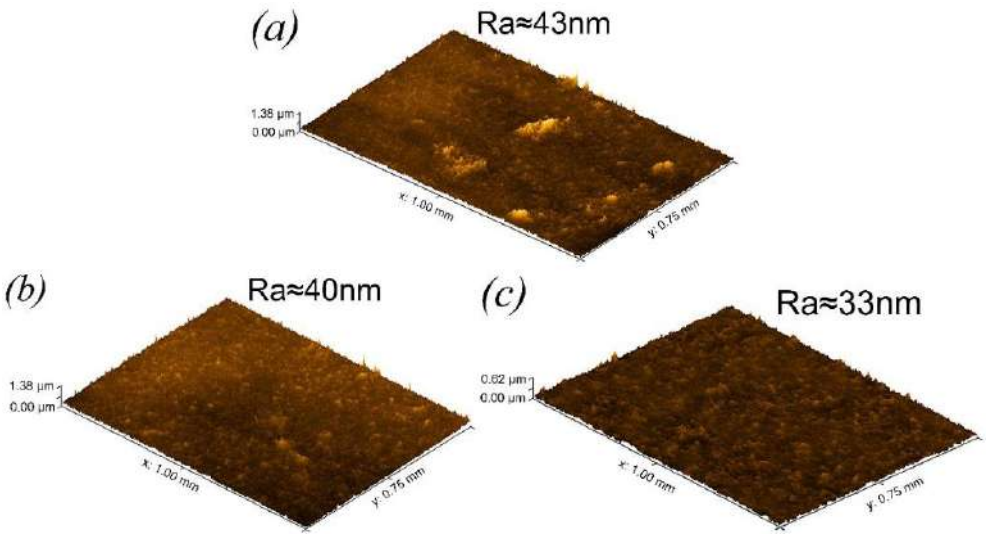


Figure 5.5 Three-dimensional surface topography of: (a) SSC, (b) PIII-200 and (c) PIII-300

300 in comparison with PIII-200 is due to the deformation of the grains because of their higher nitrogen content [5.9].

5.3. Mechanical characterization

Figure 5.6 shows the typical nanoindentation load-displacement curves for: (a) PIII-200, (b) PIII-300 and (c) SSC.

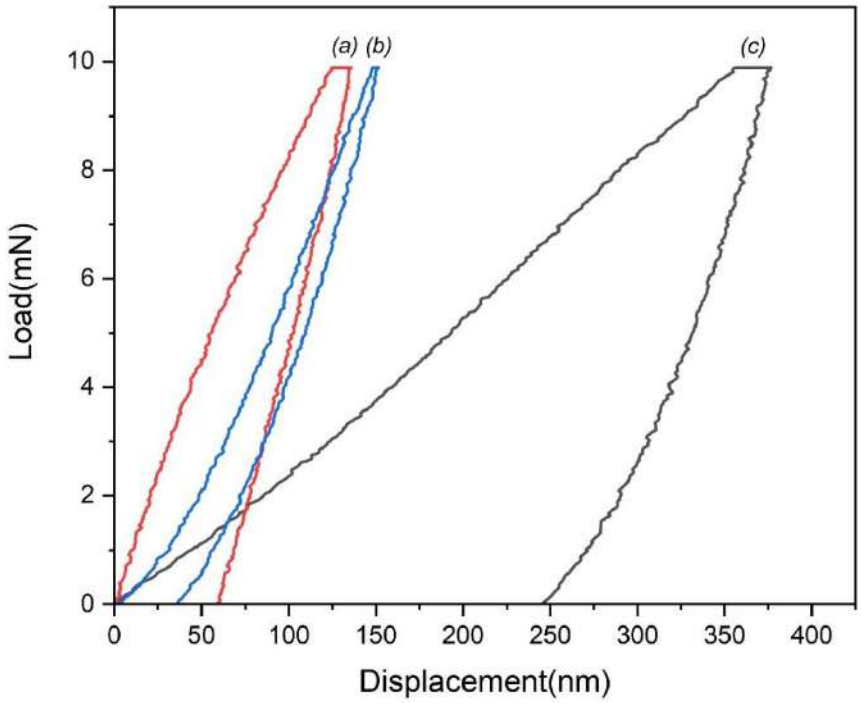


Figure 5.6 Typical nanoindentation curves for: (a) PIII-200, (b) PIII-300 and (c) SSC

The area between the loading and the unloading curves defines the plastic deformation work W_P. According to the curves, the plastic deformation work of PIII-300 is the lowest followed by PIII-200 and finally SSC. From the nanoindentation load-displacement curves, the elastic recovery of the coatings can be calculated and their values are: 76% for PIII-300, 52.81% for PIII-200 and 34.3% for SSC.

The nanoindentation test results are listed in **Table 5.1**. SSC presents a hardness of 11.7 GPa. After nitriding, the hardness increases to 14.5 GPa for PIII-200 and to 16.4 GPa for PIII-300. The increased surface hardness after annealing is attributed to the formation of γ' and ε nitride phases that can be considered as the sources of surface hardening [5.10, 5.11]. The mechanism of hardening by those phases are the precipitation and the dispersion [5.12], where precipitates acts as obstacles to the movement of dislocations [5.13].

γ' and ε phases increase also the resistance to plastic deformation of the coatings [5.12] that can be confirmed through **Table 5.1** with H^3/E^2 hardness to elastic modulus ratio results, where, PIII-300 and PIII-200 present high H^3/E^2 values comparing with the non nitrided coating. The H^3/E^2 values suggest a high wear resistance for the nitrided coatings [5.14].

PIII-300 and due to its increased amount of nitrogen diffusion and γ' and ε phases amounts has higher hardness than that of PIII-200.

Coating	**H (GPa)**	**E (GPa)**	**H^3/E^2 (GPa)**
SSC	11.7±0.7	182.6±2.8	0.05
PIII-200	14.5±0.5	120.7±3.2	0.21
PIII-300	16.4±3.2	130.6±1.2	0.26

Table 5.1 Nanoindentation test results for: SSC, PIII-200 and PIII-300

5.4. Tribological characterization

Figure 5.7 (a) presents the friction curve of SSC which exhibits two stages. First, COFs increase sharply up to a peak of μ≈0.58 at 6.8 m, then, the COFs decrease and stabilize at μ≈0.53.

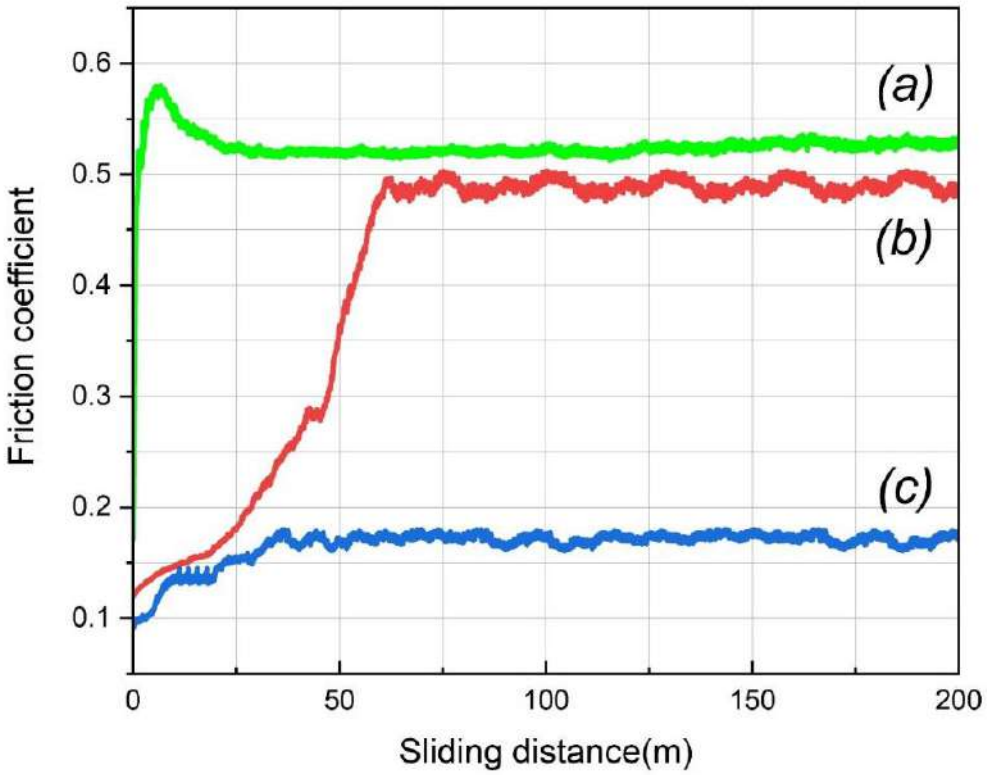


Figure 5.7 Friction coefficient variations as function of the sliding distance for: (a) SSC, (b) PIII-200, (c) PIII-300

For PIII-200 coating friction curve shown in **Figure 5.7 (b)**. COFs increase sharply first until reaching a value of about μ≈0.49 at 61.5 m, then, COFs are stabilized at this value until the end of the test. The same friction curve trend is observed for PIII-300 in **Figure 5.7 (c)**, but the sharp increase is observed until 31.6 m of sliding where COFs are reaching their steady value of about μ≈0.18. For the two nitrided coatings, their COF values were first depending on the hardness difference between the two mating surfaces [5.15], then the wear debris in the interface between the two surfaces work as an abrasive third bodies which increase the wear severity and so COF values. The later stabilization in COFs are attributed to the formation of the protective oxide layers on the wear profiles.

Table 5.2 shows the tribological test results of all the coatings. PIII-300 has a very low COF of: μ=0.16. PIII-200 has also a low COF of: μ=0.30. The nitrided coatings have lower COFs than the SSC with μ=0.52. PIII-300 presents also the lowest wear rate of $k=2.97\cdot10^{-7}$ $mm^3/N\cdot m$ which is lower by more than two orders of magnitude of SSC, followed by PIII-200 with $k=6.03\cdot10^{-6}$ $mm^3/N\cdot m$ which is lower by one order of magnitude than that of SSC. The reduction in the wear rates of the nitrided coatings can be attributed to the formation of γ' nitride phase that is characterized by its extreme ductility and wear resistance [5.5, 5.16].

The wear rates measurements are proportional to the hardness results listed above in **Table 5.1** and in correlation with the Archard wear theory [5.14].

Coatings	**SSC**	**PIII-200**	**PIII-300**
Friction coefficient	0.52	0.30	0.16
Wear rate ($mm^3/N\cdot m$)	$7.07\cdot10^{-5}$	$6.03\cdot10^{-6}$	$2.97\cdot10^{-7}$

Table 5.2 Tribological results after PIII nitriding

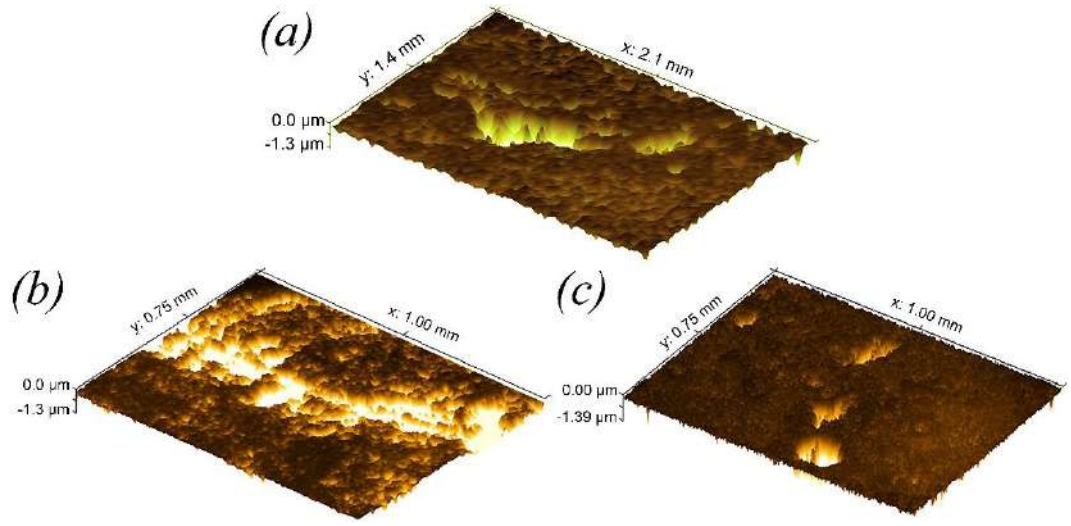


Figure 5.8 AFM 3D images of wear tracks profiles for: (a) SSC, (b) PIII-200 and (c) PIII-300

Figure 5.8 shows 3D images of the wear tracks profiles. SSC has a deep wear track of D_P=12.0 µm, while those of PIII-300 and PIII-200 are respectively D_P=0.46 µm and D_P=0.61 µm. Wear track width measurements reveal that SSC has also a wide wear track of w=0.33 mm, followed by PIII-200 with w=0.29 mm and PIII-300 with w= 0.15 mm.

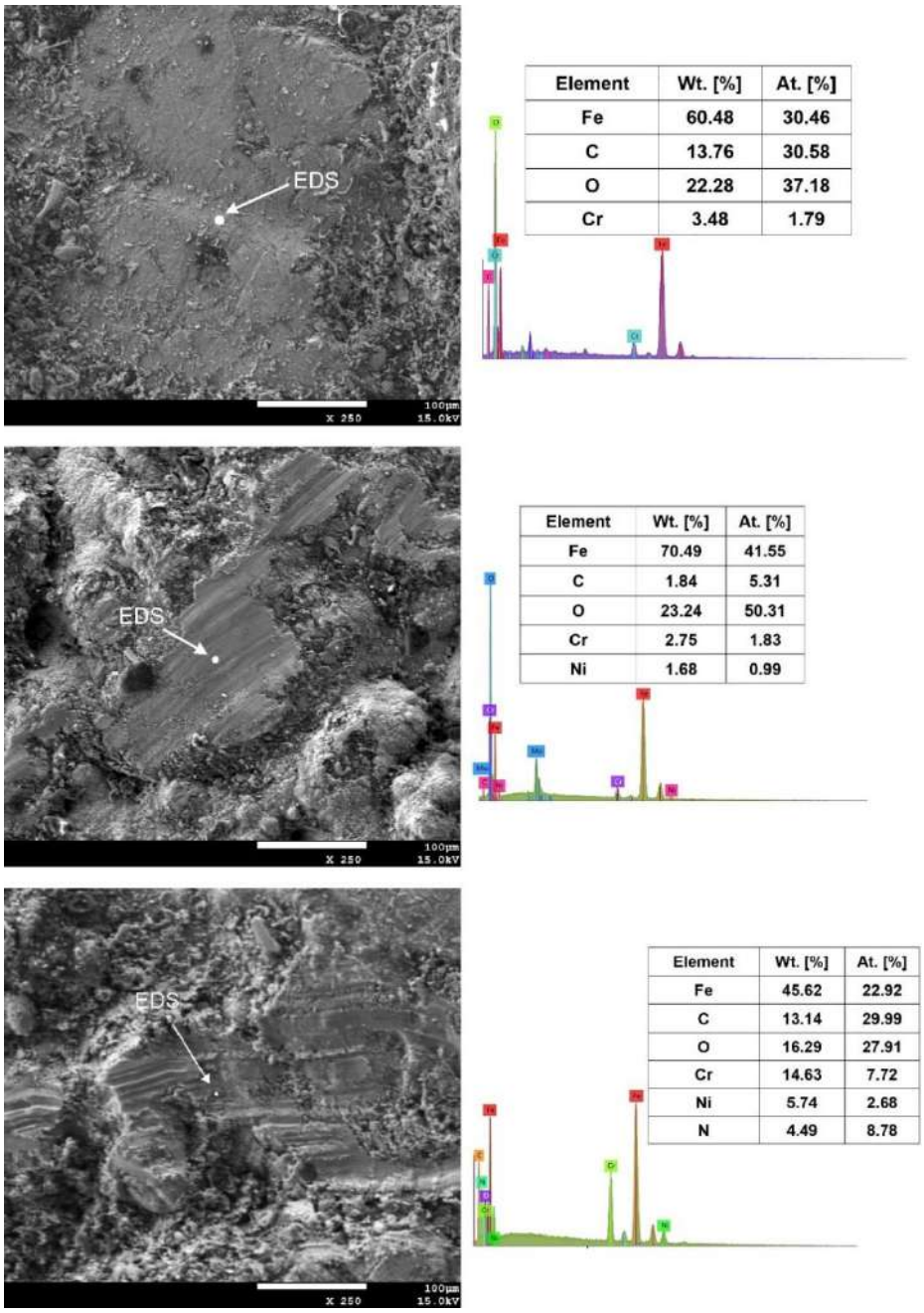


Figure 5.9 SEM wear tracks and EDS punctual analysis of the worn surfaces of: (a) SSC, (b) PIII-200 and (c) PIII-300

Figure 5.9 shows the wear tracks observed by the SEM and the EDS punctual analysis for: (a) SSC, (b) PIII-200 and (c) PIII-300. Flack-like debris associated with some scaling pits (in dark) can be seen in the SSC wear track, suggesting that delamination is the dominate wear mechanism. The protective oxide layers on the wear tracks, which are responsible for the stabilization of the friction coefficients, are detected in the punctual EDS analysis. For the nitrided coatings PIII-200 and PIII-300, abrasive grooves are clearly seen, suggesting the abrasive wear mechanism. EDS analysis on both coatings shows high amount of oxides that are probably iron oxides. Those oxides are formed during the ball counterbody sliding [5.12]. For PIII-300, nitrogen is detected in the wear track in the contrary of PIII-200, which explain their higher wear resistance.

5.5. Conclusions

The present chapter aims to study the effect of PIII nitriding on improving the tribological properties of the optimized SSC. Two values of the injected powers were used: 200 W and 300 W in order to use the one that gives the best tribological properties in the next and the final chapter. The microstructural characterization showed that both nitrided coatings were contained ε and γ' nitride phases in addition to CrN, Cr_2N and Ni_3N. Surface topography presented that the surface roughness was reduced after nitriding. Mechanical characterization showed that the hardness of the nitrided coatings was increased with the discharge power from 14.5 GPa at 200 W into 16.4 GPa at 300 W. Tribological characterization showed that both COFs and wear rates were decreased with the discharge power from μ=0.30 to μ=0.16 respectively for COFs and $k=6.03\cdot10^{-6}$ $mm^3/N\cdot m$ to $k=2.97\cdot10^{-7}$ $mm^3/N\cdot m$ for wear rates. The coating nitrided at 300 W gave a very interesting and improved surface properties either for

hardness, COF and wear rate. In the next chapter, W-Ti-N thin film will be deposited on the nitrided coating to form a duplex treatment with more developed surface properties.

References

[5.1] M. Tošić, I. Terzić, and R. Gligorijević, Plasma nitriding of powder metal steel, *Vac.*, 1990, **40**, p 131-134.

[5.2] J. Lutz, J.W. Gerlach and S. Mändl, PIII nitriding of fcc-alloys containing Ni and Cr, *physica status solidi*, 2008, **205**, p 980-984.

[5.3] R. Valencia, R. López-Callejas, A. Muñoz-Castro, S.R. Barocio, A.E. Chávez and O. Godoy-Cabrera, Nitriding of AISI 304 stainless steel by PIII in DC and RF toroidal discharges, *Brazilian J. Phys.*, 2004, **34**, p 1594-1597.

[5.4] K. Kostov, M. Ueda, M. Lepiensky, P. Soares, G. Gomes, M. Silva and H. Reuther, Surface modification of metal alloys by plasma immersion ion implantation and subsequent plasma nitriding, *Surf. Coat. Technol.*, 2004, **186**, p 204-208.

[5.5] J.F. Lin, K.W. Chen, C.C. Wei, and C.F. Ai, The effects of differing nitrogen implantation conditions on penetration depth, mechanical properties and tribological behavior of plasma-nitrided AISI 304 stainless steel, *Surf. Coat. Technol.*, 2005, **197**, p 28-38.

[5.6] L. Shen, and N. Wang, Effect of Nitrogen Pressure on the Structure of Cr-N, Ta-N, Mo-N, and W-N Nanocrystals Synthesized by Arc Discharge, *J. Nanomaterials*, 2011, **2011**, p 1-5.

[5.7] D. Vempaire, S. Miraglia, A. Sulpice, L. Ortega, E.K. Hlil, D. Fruchart, and J. Pelletier, Structure and magnetic properties of nickel nitride thin film synthesized by plasma-based ion implantation, *J. Magnetism Magn. Mater.*, 2004, **272-276**, p E843-E844.

[5.8] J.C. Caicedo, L. Yate, and J. Montes, Improving the physicochemical surface properties on AISI D3 steel coated with Ti-W-N, *Surf. Coat. Technol.*, 2011, **205**, p 2947-2953.

[5.9] G.A. Collins, R. Hutchings, K.T. Short, J. Tendys, X. Li, and M. Samandi, Nitriding of austenitic stainless steel by plasma immersion ion implantation, *Surf. Coat. Technol.*, 1995, **74-75**, p 417-424.

[5.10] M.M. Alim, R. Tadjine, A. Keffous and M. Kechouane, Improvement in Electromechanical and Electrochemical of Low Carbon Steel Samples by PIII Treatment, *Proceedings of the 1st International Conference on Renewable Energy and Energy Conversion*, 2019, p 523-530

[5.11] M.F. Yan, Y.Q. Wu, and R.L. Liu, Plasticity and ab initio characterizations on Fe_4N produced on the surface of nanocrystallized 18Ni-maraging steel plasma nitrided at lower temperature, *Appl. Surf. Sci.*, 2009, **255**, p 8902–8906.

[5.12] B.C.E.S. Kurelo, W.R. DeOliveira, F.C. Serbena and G.B. DeSouza, Surface mechanics and wear resistance of supermartensitic stainless steel nitrided by plasma immersion ion implantation, *Surf. Coat. Technol.*, 2018, **353**, p 199-209.

[5.13] M. Meyers, and K. Chawla, *Mechanical Behavior of Materials*, Cambridge University Press, New York, 2009.

[5.14] K. Chemaa, Y. Chabani, M. Gaceb and S. Hassani, "Study of tribological properties of titanium-based thin films applied to the rubbing parts of internal combustion engines piston", Master degree Thesis, M'hamed Bougara University Boumerdes, 2017.

[5.15] S. Hassani, M. Bielawski, W. Beres, L. Martinu, M. Balazinski, J.E. Klemberg-Sapiehaa, Predictive tools for the design of erosion resistant coatings, Surf. Coat. Technol., 2008, **203**, p 204-210.

[5.16] M.H. Farazmand, H. Khorsand and H. Ebrahimnezhad-Khaljiri, The Effect of the Plasma-Nitriding Process on the Structure and Wear Properties of the Sintered Low Alloy Steel, *Metallography Microstructure Anal.*, 2018, **7**, p 711-723.

Chapter 6

Improving the tribological behaviour by W-Ti-N duplex treatment

6.1. Introduction

The aim of this final chapter is to deposit a W-Ti-N thin film by the means of magnetron PVD system on the nitrided stainless steel coating that is optimized previously in the chapters 4 and 5, in order to obtain a duplex treated coating with improved tribological properties, which is the main objective of the thesis study. The experimental details and the magnetron PVD system description were already presented in the section 3.6. The optimized stainless steel coating from chapter 4 which is the SS-800 coating will be referred to by SSC. The optimal nitrided coating from chapter 5 will be referred to by PIII/SSC and finally, the duplex treated coating will be referred to by W-Ti-N/PIII/SSC.

6.2. Microstructural characterization

Figure 6.1 shows the XRD patterns of: (a) SSC, (b) PIII/SSC and (c) W-Ti-N/PIII/SSC multilayer coatings. W-Ti-N/PIII/SSC multilayer coating patterns exhibit two crystallographic

orientations of W_2N and TiN: the (220) and the preferential orientation (111) [6.1]. In addition, α-Ti phase is observed.

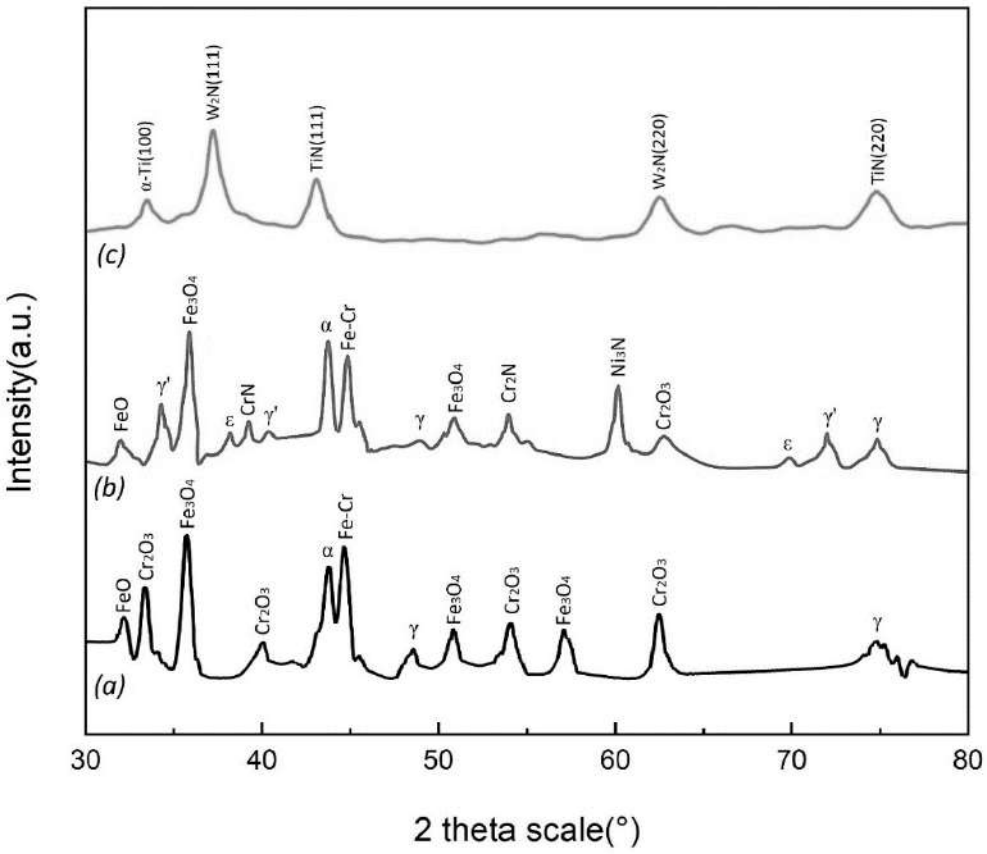


Figure 6.1 XRD diffraction patterns of: (a) SSC, (b) PIII/SSC and (c) W-Ti-N/PIII/SSC multilayer coatings

Figure 6.2 presents the cross-section images of: (a) SSC, (b) PIII/SSC and (c) W-Ti-N/PIII/SSC multilayer coatings. All the three multilayers display dense and smooth microstructures. For W-Ti-N thin film showed in **Figure 6.2 (c)**, compact columnar-like structures can be seen that are of type T of the Thornton's classification [6.2]. The thin film thickness is about 970±12 nm.

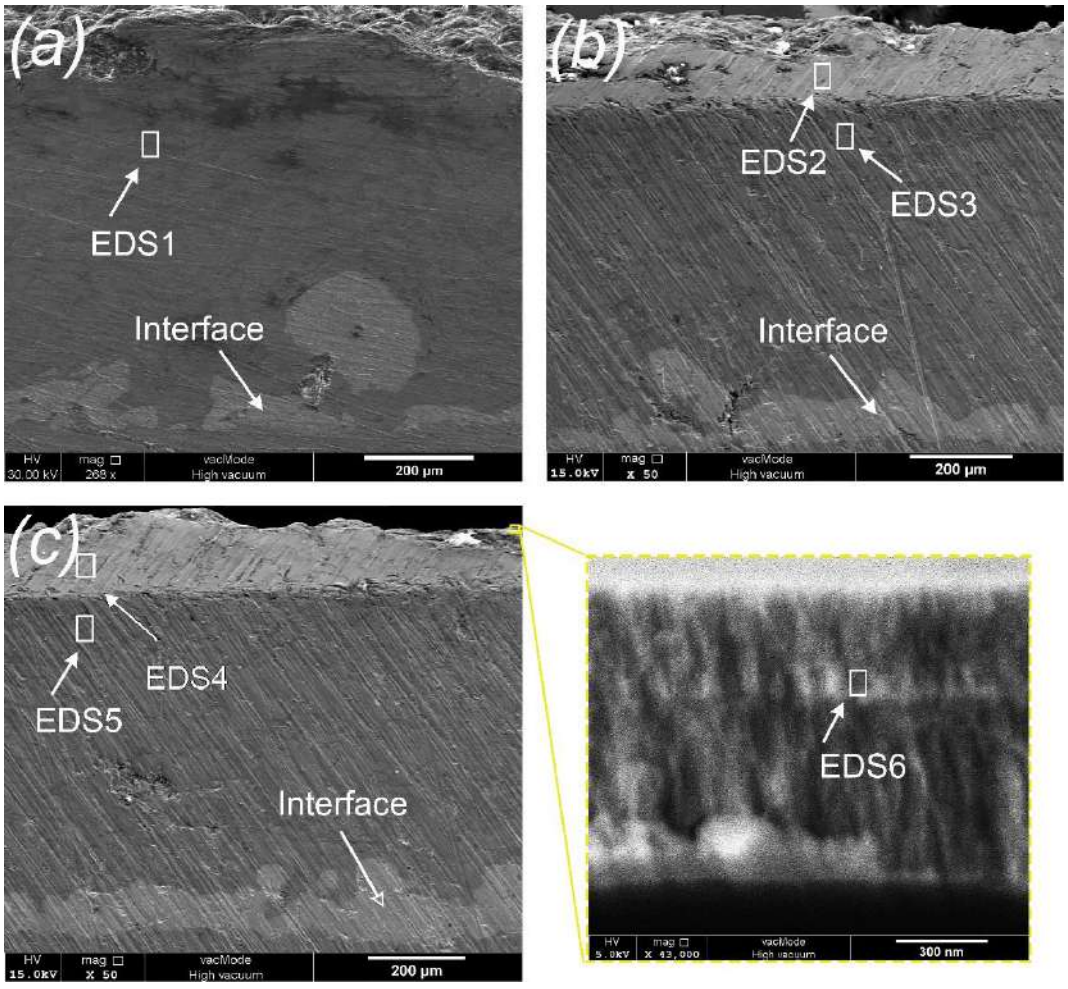


Figure 6.2 Cross-section images of: (a) SSC, (b) PIII/SSC and (c) W-Ti-N/PIII/SSC multilayer coatings

Figure 6.3 shows the EDS analysis results at the different zones indicated in **Figure 6.2**. For the W-Ti-N/PIII/SSC multilayer, low nitrogen composition was detected either in the W-Ti-N thin film, the nitrided layer or the SSC coating, this is probably due to the nitrogen diffusion in the coating interface direction along the interstitial sites [6.3].

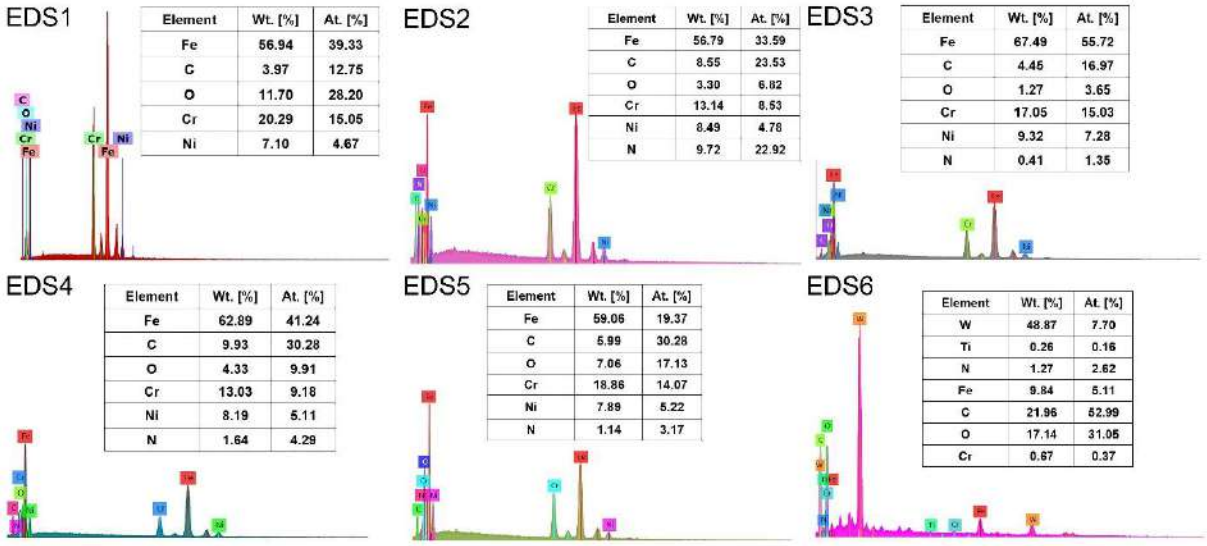


Figure 6.3 EDS analysis results at the different zones

Figure 6.4 shows the SEM surface morphologies for: (a) SSC, (b) PIII/SSC and (c) W-Ti-N/PIII/SSC multilayer coatings.

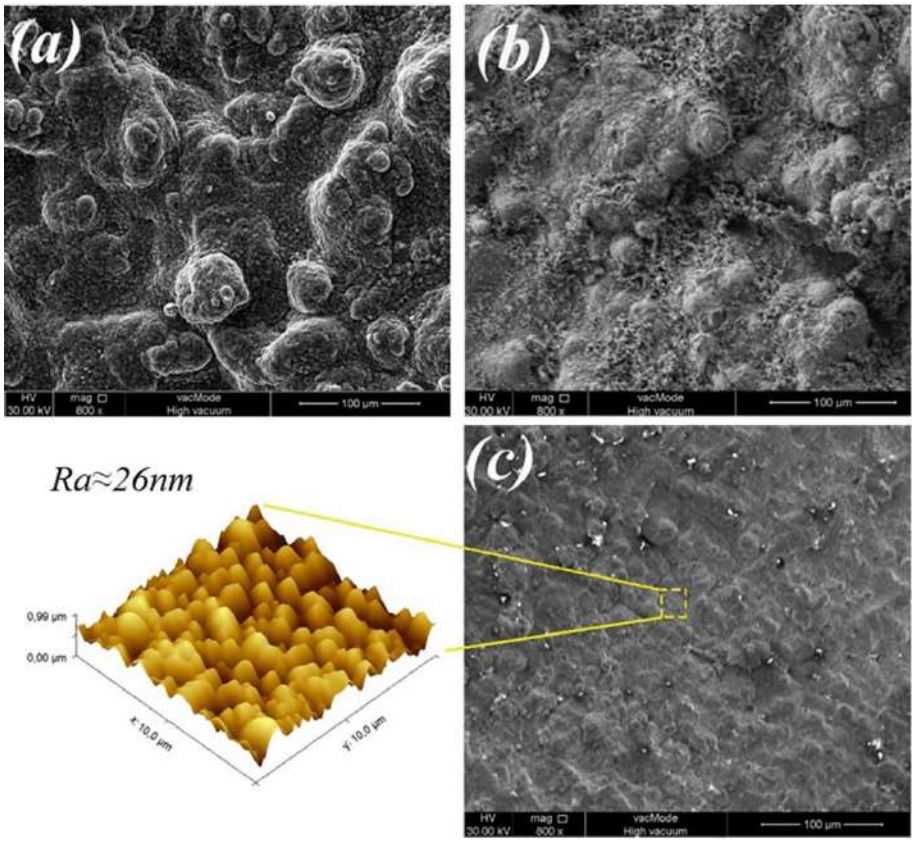


Figure 6.4 SEM top view images for: (a) SSC, (b) PIII/SSC and (c) W-Ti-N/PIII/SSC

The roughness is reduced after nitriding from: Ra≈ 43 nm for the non nitrided multilayer coating into Ra≈ 33 nm for the nitrided one and Ra≈ 26 nm for the W-Ti-N thin film on the nitrided multilayer. This reduction is related to the Ar^+ ion bombardment application before nitriding and the deposition of the thin film as explained in chapter 5 [6.4]. The roughness of the W-Ti-N surface is relatively high in comparison to the other thin films and that is related to the roughness of the SSC multilayer since thin films duplicate the morphology of the substrates [6.5].

6.3. Mechanical characterization

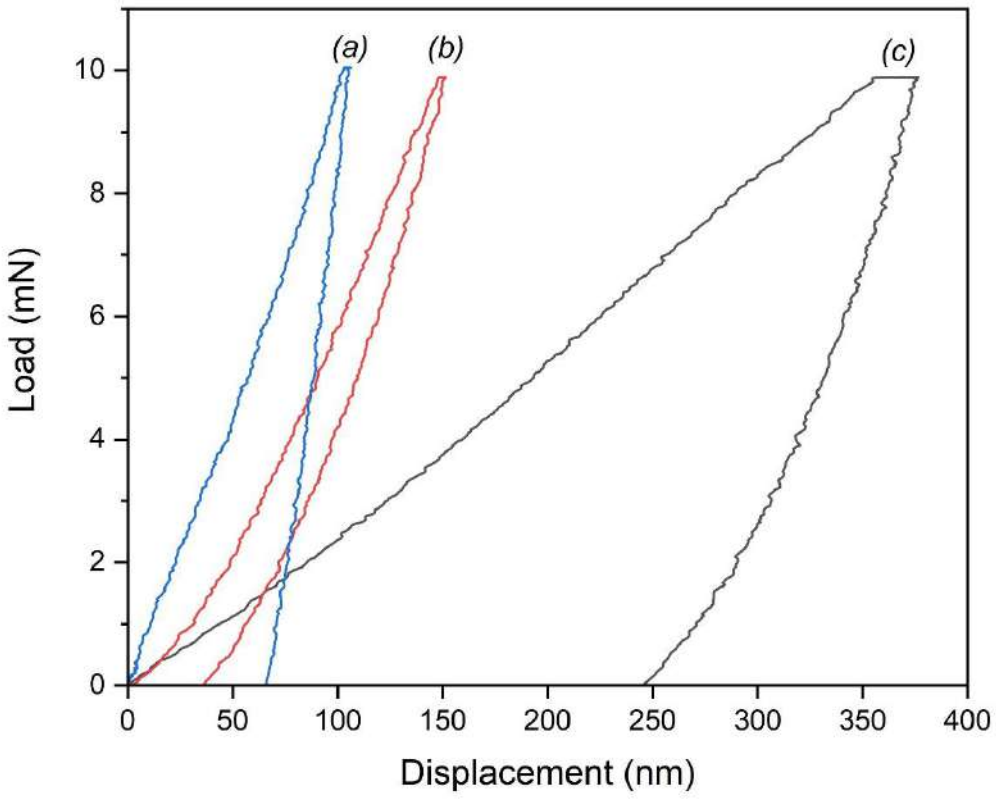


Figure 6.5 Typical nanoindentation curves for: (a) W-Ti-N/PIII/SSC, (b) PIII/SSC and (c) SSC multilayer coatings

Figure 6.5 shows the typical nanoindentation load-displacement curves for: (a) W-Ti-N/PIII/SSC, (b) PIII/SSC and (c) SSC multilayer coatings. From that figure, it can be seen that the indentation depth obtained for W-Ti-N/PIII/SSC is 105 nm, which is a sign of a higher hardness due to the fact that the hardness is function of the penetration depth [6.6]. The penetration depth of PIII/SSC is 151 nm, which is higher than that of SSC with 375 nm.

From **Figure 6.5**, the calculated values of the elastic recovery are 76% for PIII/SSC, 36.3% for W-Ti-N/PIII/SSC and 34.3% for SSC.

The nanoindentation results are listed in **Table 6.1**. SSC presents a hardness of 11.7 GPa.

Multilayers	**H (GPa)**	**E (GPa)**	**H^3/E^2 (GPa)**
SSC	11.7±0.7	182.6±2.8	0.05
PIII/SSC	16.4±3.2	130.6±1.2	0.26
W-Ti-N/PIII/SSC	22.3±3.1	219.8±7.9	0.23

Table 6.1 Nanoindentation test results for: SSC, PIII/SSC and W-Ti-N/PIII/SSC

After nitriding, the hardness increases into 16.4 GPa. After W-Ti-N thin film deposition, the hardness increases to 22.3 GPa. In comparison to the previous hardness results obtained with the same deposition conditions of W-Ti-N monolayer (7.1 GPa) or W-Ti-N/Al-Si multilayer (17.2 GPa) [6.7], the present hardness is the highest among them and that is related to existence of the nitrogen layer between the W-Ti-N thin film and the SSC multilayer coating. In the beginning of the deposition, Ti atoms and due to their high reactivity with N atoms form TiN compounds that grows at the W grains boundaries and act as nucleation sites. The TiN compounds amounts surrounding the W grains increase when increasing the N concentrations either during the W-Ti-N deposition or after N atoms diffusion from the

nitrided layer. At higher concentrations, W grains will be sized by the TiN compounds and a film with low density will be obtained and thereby, higher hardness will be obtained following the Hall-Petch relationship [6.8]. The mismatch of the thermal expansion coefficient between the W-Ti-N thin film, the nitrided layer, the SSC and the carbon steel substrate that induce the formation of thermal stresses during the cooling stage of the duplex treated multilayer has also a key contribution on the increased hardness.

Obtaining the preferred orientation (111) that can be considered as the most densely packed plane [6.9] can improve also the hardness of the W-Ti-N film. Furthermore, the hardness behaviour of W-Ti-N/PIII/SSC has in comparison with PIII/SSC and SSC multilayers is attributed to the surface morphology (roughness and grain size) of W-Ti-N thin film [6.4].

The resistance to plastic deformation H^3/E^2 values confirm the elastic recovery values above, where H^3/E^2 decrease as the elastic recovery increase. The plastic deformation values of PIII/SSC and W-Ti-N/PIII/SSC multilayers are respectively 0.26 and 0.23 which is about 5 times higher than that of SSC multilayer with 0.05, suggesting interesting wear resistances [6.10].

6.4. Tribological characterization

Figure 6.6 presents the friction curve of (a) SSC, (b) PIII/SSC and (c) W-Ti-N/PIII/SSC multilayer coatings. W-Ti-N thin film on the nitrided SSC friction curve has a steady variation between μ=0.129 and μ=0.148 due to the high hardness of W-Ti-N thin film [6.7].

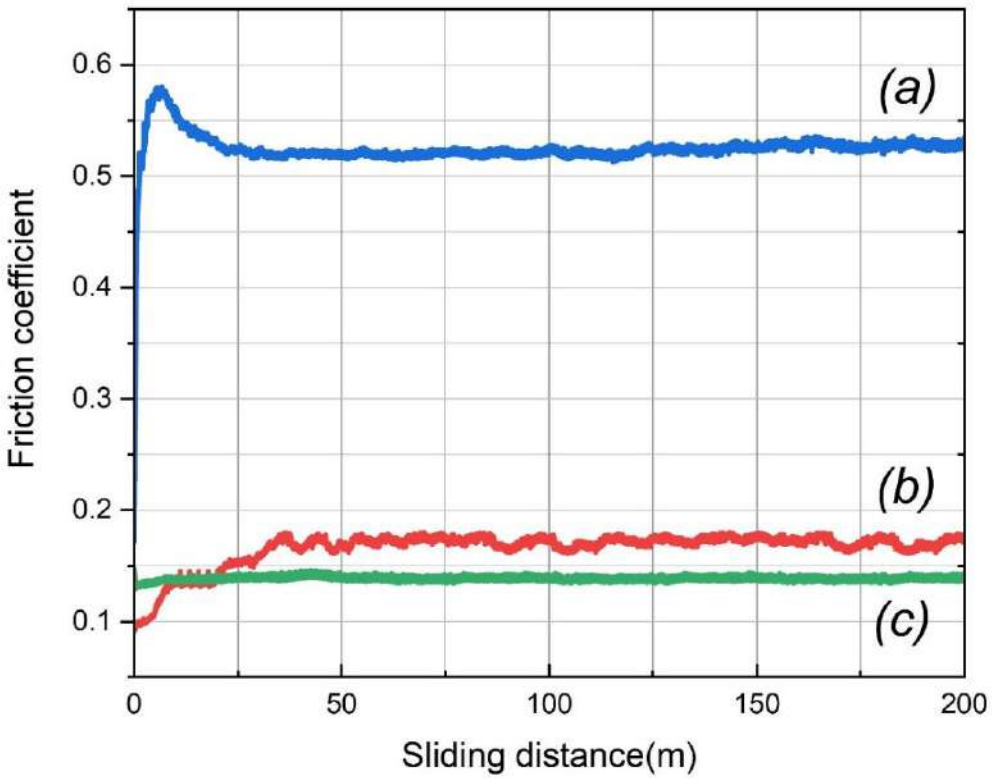


Figure 6.6 friction coefficient variations as function of the sliding distance for: (a) SSC, (b) PIII/SSC, (c) W-Ti-N/PIII/SSC multilayer coatings

Table 6.2 shows the tribological test results of all the coatings. W-Ti-N/PIII/SSC multilayer has a low COF of: μ=0.14. PIII/SSC has also a low COF of: μ=0.16. Whilst SSC has a COF of μ=0.52. W-Ti-N/PIII/SSC multilayer has also a very low wear rate of $k=7.55\cdot10^{-8}$ $mm^3/N\cdot m$ which is lower by three times of magnitude than that of SSC. PIII/SSC present also a low wear rate of $k=2.97\cdot10^{-7}$ $mm^3/N\cdot m$. The obtained wear rate of W-Ti-N/PIII/SSC multilayer is the lowest value measured for W-Ti-N thin films, lower than that reported by Silva et al. [6.11] with a wear rate in the order of 10^{-6}-10^{-5} $mm^3/N\cdot m$ and lower than that measured by Chemaa et al. [6.7] with wear rate in the order of $k=2.4$-$2.7\cdot10^{-3}$ $mm^3/N\cdot m$ with the same deposition conditions.

Coatings	**SSC**	**PIII/SSC**	**W-Ti-N/PIII/SSC**
COF	0.52	0.16	0.14
Wear rate ($mm^3/N \cdot m$)	$7.07 \cdot 10^{-5}$	$2.97 \cdot 10^{-7}$	$7.55 \cdot 10^{-8}$

Table 6.2 Tribological test results

Figure 6.7 shows 3D images of the wear tracks profiles. SSC has a deep wear track of D_P=12.0 µm, while those of PIII/SSC and W-Ti-N/PIII/SSC are respectively D_P=0.46 µm and D_P=0.27 µm, the wear track depth of the W-Ti-N thin film is shallower than the film thickness, not penetrating down to the nitrided stainless steel multilayer. Wear track width measurements reveal that SSC has also a wide wear track of w=0.33 mm. W-Ti-N/PIII/SSC has very narrow wear track of w=0.05 mm, whereas PIII/SSC has a wear width of: w= 0.15 mm.

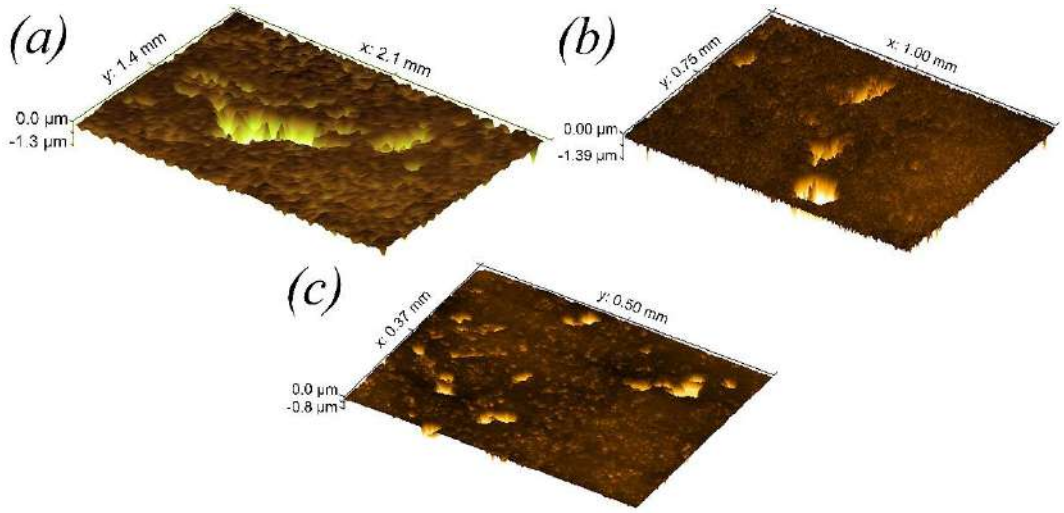


Figure 6.7 AFM 3D images of wear tracks profiles for: (a) SSC, (b) PIII/SSC and (c) W-Ti-N/PIII/SSC multilayer coatings

Figure 6.8 shows the wear tracks observed by SEM and the EDS punctual analysis for: (a) SSC, (b) PIII/SSC and (c) W-Ti-N/PIII/SSC.

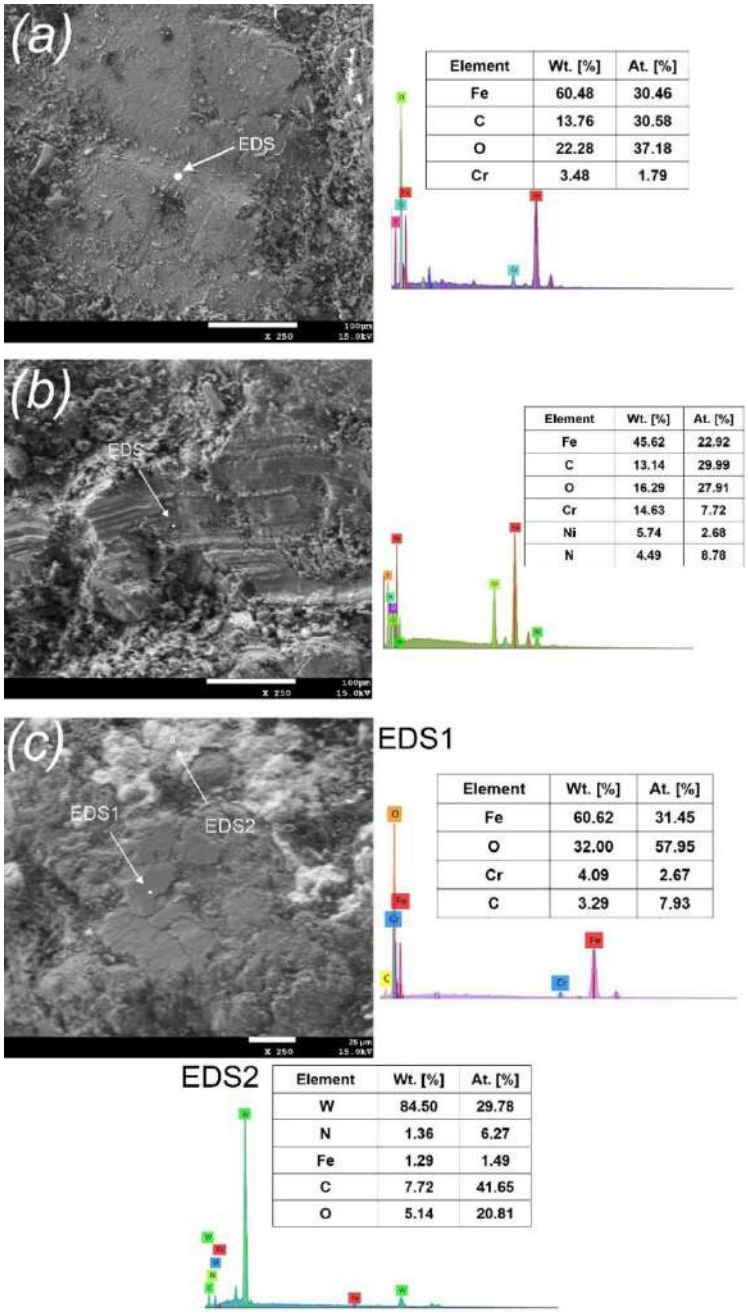


Figure 6.8 SEM wear tracks and EDS punctual analysis of the worn surfaces of: (a) SSC, (b) PIII/SSC and (c) W-Ti-N/PIII/SSC multilayer coatings

The wear track profile of W-Ti-N/PIII/SSC shows positive parts indicating the adhesive wear mechanism. Punctual EDS analysis inside and outside the positive parts (EDS1 and EDS2

respectively) reveals that the positive part has a high composition of Cr, while there is no W, Ti or N contents, suggesting that the adhered parts come from the counterpart ball which justifies the adhesive wear. That wear mechanism is originated from the existence of high amount of W in the film that has the highest compatibility to form adhesive combination with Cr according to Robinowicz compatibility table [6.12] shown in **Figure 6.9**.

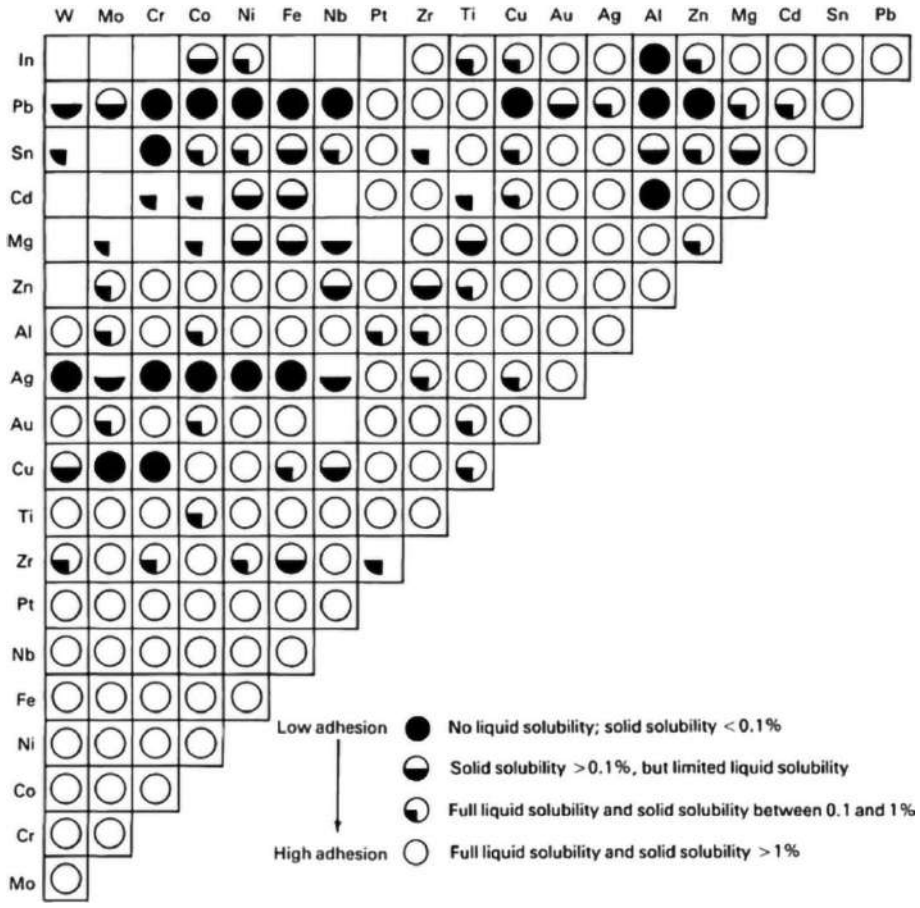


Figure 6.9 Rabinowicz Compatibility table [6.12]

6.5. Conclusions

The present chapter deal with W-Ti-N thin film that was applied on the nitrided SSC optimized before in order to give enhanced tribological properties to its surface. A duplex treated multilayer coating formed from W-Ti-N/PIII/SSC was obtained. Each layer was obtained through a different deposition method. The microstructure characterization showed that the film had two crystallographic orientations of W_2N and TiN: the (220) and the preferential orientation (111). The surface topography exhibited that the surface roughness and density is low. Mechanical characterization showed that the hardness of the film is up to 22.3 GPa that is harder than the other films deposited before with the same deposition conditions. Tribological characterization showed that a low COF of μ=0.14 was obtained and the lowest wear rate for W-Ti-N thin film was obtained also of $k=7.55\cdot10^{-8}$ $mm^3/N\cdot m$.

References

[6.1] D. Braga, J.P. Dias, and A. Cavaleiro, Duplex treatment: W-Ti-N sputtered coatings on pre-nitrided low and high alloy steels, *Surf. Coat. Technol.*, 2006, **200**, p 4861-4869.

[6.2] J.A. Thornton, High rate thick film growth, *Annual Rev. Mater. Sci.*, 1977, **7**, p 239-260.

[6.3] J. Lutz, J.W. Gerlach and S. Mändl, PIII nitriding of fcc-alloys containing Ni and Cr, *physica status solidi*, 2008, **205**, p 980-984.

[6.4] J.C. Caicedo, L. Yate, and J. Montes, Improving the physicochemical surface properties on AISI D3 steel coated with Ti-W-N, *Surf. Coat. Technol.*, 2011, **205**, p 2947-2953.

[6.5] S. Zhou, W. Liu, H. Liu, and C. Cai, Structural and electrical properties of Ti-W-N thin films deposited by reactive RF sputtering, *Physics Procedia*, 2011, **18**, p 66-72.

[6.6] T.D. Atmani, M. Gaceb, H. Aknouche, C. Nouveau, and M.S. Bouamrene, Parametric study of the mechanical properties of nanocrystalline TiN/CrN multilayer coatings with a special focus on the effect of coating thickness and substrate roughness, *Surf. Interfaces*, 2021, **23**, 101001.

[6.7] K. Chemaa, Y. Chabani, M. Gaceb and S. Hassani, "Study of tribological properties of titanium-based thin films applied to the rubbing parts of internal combustion engines piston", Master degree Thesis, M'hamed Bougara University Boumerdes, 2017.

[6.8] J.R. Weertman, Hall-Petch strengthening in nanocrystalline metals, Mater. Sci. Eng. A, 1993, **166**, p 161-167.

[6.9] R. Jalali, M. Parhizkar, H. Bidadi, H. Naghshara, and M.J. Eshraghi, Characterization of nano-crystalline Ti-W-N thin films for diffusion barrier application: a structural, microstructural, morphological and mechanical study, *Appl. Physics A*, 2018, **124**, p 1-11.

[6.10] S. Hassani, M. Bielawski, W. Beres, L. Martinu, M. Balazinski, and J.E. Klemberg-Sapiehaa, Predictive tools for the design of erosion resistant coatings. *Surf. Coat. Technol.*, 2008, **203**, p 204-210.

[6.11] P.N. Silva, J.P. Dias, and A. Cavaleiro, Performance of W-Ti-(N) coated pins in lubricated pin-on-disk tests, *Surf. Coat. Technol.*, 2008, **202**, p 2338-2343.

[6.12] T.W. Scharf, and S.V. Prasad, Solid lubricants: a review, *J. Mater. Sci.*, 2013, **48**, p 511-531.

General conclusions

Our study aims to give solution for sever and well known issues in the oil and gas transportation industry which are the surface failures of the valves in one side and their manufacturing costs in the other. This technico-economical dilemma can have many solutions through the different fields and sciences existing. We, as tribologists and material scientists we gave our solution from our vision side, which is replacing in the first step the valves materials from massive stainless steels into carbon steels that are coated by stainless steel coatings using TWAS thermal spraying process with better surface properties (hardness, friction, wear and corrosion) and so with lower cost. The second step, tend to introduce a duplex thin films on the optimized stainless steel coating combine a nitrided layer by PIII technique with a W-Ti-N thin film by PVD magnetron sputtering technique.

In the first step, the optimized stainless steel coating was made by four layers and annealed at 800°C in vacuum conditions, the obtained hardness was 74.6% higher than that of the massive stainless steel, COF is 7.1% lower than that of the massive stainless steel, the wear rate was two orders of magnitude lower than that of the massive stainless steel and the most interesting result was the corrosion rate that was higher than that of the massive stainless steel by one order of magnitude.

Because COF was improved with only small amount, the second step concentrates more in the tribological properties. After nitriding the optimized stainless steel coating using PIII process, the hardness increased by 40.2%, COF was 69.2% lower and the wear rate was two orders of

magnitude lower. After the deposition of W-Ti-N thin film, the hardness increased by 90.6%, COF was 73.0% lower and the wear rate was three orders of magnitude lower.

With a view to improve this work, we suggest the following points to be applied next:

- Manufacturing a prototype of different types of valves from carbon steel body with the optimized stainless steel coating to apply the results from the first step of this work.
- Developing a PIII nitriding system that can be used to nitride massive mechanical pieces and prototypes.
- Developing PVD systems (sputtering or/and vacuum evaporation) that can be used to deposit thin films on massive mechanical pieces and prototypes.
- Apply the obtained coating/multilayer on other mechanical pieces subjected to friction and wear as the general thesis title mention.